UNIVERSITY OF SOUTHAMPTON

In-duct measurement techniques for the characterisation of broadband aeroengine noise

by

Christopher R. Lowis

A thesis submitted in partial fulfillment for the
degree of Doctor of Philosophy

in the
Faculty of Engineering, Science and Mathematics
Institute of Sound and Vibration Research

December 2007

UNIVERSITY OF SOUTHAMPTON

ABSTRACT

FACULTY OF ENGINEERING, SCIENCE AND MATHEMATICS
INSTITUTE OF SOUND AND VIBRATION RESEARCH

Doctor of Philosophy

by Christopher R. Lowis

The focus of this thesis is the measurement of broadband fan noise, which due to reductions in tonal and jet noise, is now the dominant source at approach, and a major contributor at takeoff. This thesis proposes three new in-duct measurement techniques for the characterisation and measurement of broadband fan noise. A complete characterisation of broadband noise involves determining the sources of sound, their location, and the sound field they generate.

The first new in-duct measurement technique uses *inverse methods* to determine the noise source strengths on a ducted fan. The novel aspect of this technique is that it allows source strengths to be determined both in the rotating (or rotor-bound) reference frame and stationary (stator-bound) reference frame.

The second technique is the development of an in-duct, rotating focus beamformer that allows beamforming in both rotating and stationary reference frames using an in-duct microphone array. The ability of the beamformer to determine the strengths of the rotor-based and stator-based sources is demonstrated using numerical simulations, with particular emphasis on the determination of the relative contributions of the rotor and the stator to overall broadband noise.

The third measurement technique is designed to allow radiated directivity patterns to be predicted from in-duct measurements. This technique allows the prediction of radiated directivity from hollow no-flow ducts, fan inlets and annular exhaust ducts from in-duct measurements. The technique is also validated using experimental data acquired from a no-flow duct rig.

Finally, an *in-situ* phase calibration method for in-duct axial arrays is proposed. This technique allows the rapid calibration of microphone arrays used in the three measurement techniques presented in the thesis. The technique is validated using experimental data.

Contents

Nomenclature

α Angle of alignment of a dipole source to the duct axis, page 13

$\bar{\square}$ Denotes Prandtl-Glauert transformed coordinates, page 64

β Doppler factor $\sqrt{(1-M^2)}$, page 64

$|b(\phi,\omega)|^2$ In-duct axial beamformer response, page 63

$\Delta\mathbf{y}_{\frac{1}{2}}$ Beamformer mainlobe width. Also in the three coordinates $\Delta z_{\frac{1}{2}}$,$\Delta r_{\frac{1}{2}}$,$\Delta\theta_{\frac{1}{2}}$, page 44

$\square^{+}$ Pseudo-inverse operator, page 17

$\square^{H}$ Hermitian transpose operator, page 17

δ Dirac delta function, page 26

Δr_s Radial separation distance between sources, page 29

$\Delta\theta_s$ Azimuthal source separation angle, page 23

Δz Axial separation distance between microphones in the in-duct array, page 40

δz Separation distance between source and first microphone ring, page 29

σ_{mn} Mode Eigenvalue for a hard-walled duct, page 13

γ_{mn} Mode wave number, page 13

$|H(\phi,\omega)|^2$ In-duct to far-field transfer function, page 63

i Imaginary number $\sqrt{-1}$, page 13

$\kappa(\square)$ Condition number of a matrix $\square$, page 22

κ_{mn} Mode wave number, page 13

λ Acoustic wavelength, page 28

$\tilde{\mathbf{y}} = (r_s, \tilde{\theta}_s, z_s)$ Source position evaluated in the rotating reference frame, page 14

$\mathbf{e}$ Vector of errors, page 17

$\mathbf{f}$ Vector of source strengths, page 16

$\mathbf{G}$ Matrix of Green's functions, page 16

$\mathbf{p}$ Vector of measured pressures, page 16

$\mathbf{w}$ Beamformer weighting vector, page 36

$\mathbf{x} = r, \theta, x$ Cylindrical coordinate system, page 12

$\mathbf{y} = r_s, \theta_s, z_s$ Location of source in cylindrical coordinate system, page 12

Λ_{mn}^2 Mode normalisation constant, page 13

Ω Rotational frequency of source, page 12

$|p_f(\phi, \omega)|^2$ Far-field directivity, page 63

ϕ Far-field polar directivity angle, page 64

ϕ_b Beamsteer angle for the axial beamformer, page 67

$\bar{\phi}_{mn}$ Mode ray angle of the $(m,n)^{\text{th}}$ mode, page 64

Ψ_{mn} Normalised mode shape function of the $(m,n)^{\text{th}}$ mode, page 64

ψ_{mn} Mode shape function, page 13

$\mathbf{S}_{p_\Omega p_\Omega}$ Cross-spectral matrix of modified pressure measurements p_Ω, page 37

$\text{AG}(\phi)$ Beamformer array gain, page 74

$\tilde{\mathbf{y}}_b$ Beamformer focus point in rotating reference frame, page 36

$\tilde{S}$ Blade surface in rotating reference frame, page 14

ϖ The sound power carried by a single mode above cut-off, page 67

$|p_w(\phi_{mn}, \omega)|^2$ Square pressure at the duct wall due to the $(m,n)^{\text{th}}$ mode, page 66

$\mathcal{S}$ Duct cross-sectional area πa^2, page 73

a Radius of duct, page 13

A_{mn} Mode amplitude of the $(m,n)^{\text{th}}$ mode, page 64

B Number of fan blades, page 24

c Speed of sound, page 12

$E\{\square\}$ Expectation operator, page 15

G Green's function, page 13

Acknowledgements

I am indebted to my supervisor Dr. Phil Joseph for his support. As he often reminds students "A Ph.D is a journey"; it's been a pleasure to have his good natured companionship and technical expertise on mine. I am also thankful for the involvement of my advisory panel members Prof. Philip Nelson, Dr. Alan McAlpine and in particular Dr. Keith Holland, who's input and advice at all stages of my studies have been of tremendous help. The final version of the thesis was also improved immensely thanks to the advice and comments of Dr. Pieter Sijtsma, who served as my external examiner.

The ISVR has been an inspiring place to complete my doctorate, thanks in no small part to my many friends and colleagues here. In particular Mrs. Susan Brindle for her tireless secretarial support, Prof. Jeremy Astley, Dr. Rod Self, and all of my friends from "the house" past and present who made the day-to-day experience constantly enjoyable. A special thank you is reserved for my former friends and colleagues at DLR Berlin, in particular Dr. Lars Enghardt, for providing me with a firm foundation on which to begin my Ph.D.

My parents have been a constant source of love, support and encouragement for which I am ever grateful. I also offer my love and thanks to Steve for his brotherly friendship, and to Minori, for everything.

Finally, I thank Rolls-Royce Plc and EPSRC for their financial support.

If your mind is truly, profoundly stuck, then you may be much better off than when it was loaded full of ideas. **Robert M. Pirsig**, *Zen and the Art of Motorcycle Maintenance.*

Chapter 1

Introduction

1.1 Introduction

Aeroengine noise-engineers need innovative measurement techniques to help them quantify, and ultimately reduce, the noise of their engines. Commercial pressures, driven by increasingly stringent government and community noise standards, require manufacturers to produce ever quieter engines.

The noise produced by an aircraft is the sum of a number of individual noise sources, such as the fan, the jet and turbulence-noise generated by the airframe, among others. Before the advent of high bypass ratio engines, jet noise, which scales at a high power of jet velocity, was far and away the most dominant noise source, and for many years all efforts were focused on reducing it. Today the situation is less clear. All noise sources are now of comparable importance, and to reduce noise further we must give equal attention to each of them. We require measurement techniques to quantify the contribution to the overall noise from each of the individual sources.

1.1.1 Thesis Overview

The focus of this thesis is the measurement of broadband fan noise, which due to reductions in tonal and jet noise, is now the dominant source at approach, and a major contributor at takeoff [1]. This thesis proposes three new in-duct measurement techniques for the characterisation and measurement of broadband fan noise. A complete characterisation of broadband noise involves determining the sources of sound, their location, and the sound field they generate.

This chapter presents a survey of the literature and shows that there are comparatively few measurement techniques available for the location and quantification of broadband noise sources on a rotating fan. In chapter 2 a new in-duct measurement technique is

proposed. This technique uses *inverse methods* to determine the noise source strengths on a ducted fan. The novel aspect of this work is that it allows source strengths to be determined both in the rotating (or rotor-bound) reference frame and stationary (stator-bound) reference frame.

In chapter 3 the principles developed in chapter 2 are used to allow beamforming in both rotating and stationary reference frames using an in-duct microphone array. The ability of the beamformer to determine the strengths of the rotor-based and stator-based sources is demonstrated using numerical simulations, with particular emphasis on the determination of the relative contributions of the rotor and the stator to overall broadband noise.

Chapter 4 presents a third measurement technique. During fan-rig experiments it is often impractical to measure radiated noise directly. The proposed technique uses an in-duct axial array of microphones to predict the radiated directivity pattern. The theory developed in chapter 4 allows the prediction of radiated directivity from hollow no-flow ducts, fan inlets and annular exhaust ducts from in-duct measurements. In chapter 5 this technique is validated using experimental data acquired from a no-flow duct rig.

All three of the proposed techniques require well-calibrated microphone arrays. In chapter 6 an *in-situ* phase calibration technique is proposed. This technique allows the rapid calibration on an in-duct axial microphone array. The calibration technique is validated using the experimental data acquired in chapter 5. The final chapter of this thesis summarises and gives some suggestions for further work.

1.2 Literature Review

1.2.1 The case for measurement techniques

The ultimate goal for aeroengine manufacturers is to pass the ICAO (International Civil Aviation Organisation) noise certification [2]. This test awards an aircraft a "chapter rating" (after the chapter of the report in which the requirements for the standard are contained) based on a standardised measure of its noise at take off, landing and flyover. Based on the outcome of this test the operations of an aircraft may be restricted, for example, to day time flights only at particular airports. Tandon [3] gives a recent summary of the ICAO certification and local certifications in use at individual airports. Since the certification itself is an experimental technique the most reliable estimate of how well a new engine will perform is achieved by duplicating the certification procedure as closely as possible.

The ICAO standardised test does not, however, reveal anything about the individual sources that contribute to the total noise. Measurement techniques are required to

provide a direct means of examining how noise is generated. This is especially important for broadband noise which is generated by small scale turbulence structures interacting with high-speed rotating machinery components. Measurement techniques provide a means to understand how broadband fan noise is generated, and how best to minimise it.

1.2.2 Measurement techniques for the characterisation of aeroengine noise

In order to completely characterise broadband aeroengine noise we must know the following,

- The location and strengths of the acoustic sources on the fan and stator generated by the flow of air over the vanes and blades, and the interaction of turbulence with solid, rotating blades.
- The sound field in the inlet or bypass duct. The in-duct sound field is typically described either in terms of a summation of modal components, or alternatively for broadband sound as a summation of "rays" with varying ray angles. Knowledge of the in-duct sound field allows predictions of the effect on the noise of acoustic lining or varying duct geometry.
- The radiated directivity from the engine. Predictions of the contribution of broadband engine noise to the overall noise "footprint" of the aircraft depends on the directivity of the radiated noise, that is the noise level in the far-field as a function of frequency and angle from the duct-axis. The directivity will be affected by the geometry of the duct exit, and by the mounting of the engine on the aircraft.

The following sections present some of the experimental techniques that have been developed to allow the characterisation of aeroengine noise.

Phased array flyover tests

The objective of aeroengine manufacturers, at least as far as noise is concerned, is to develop engines that are quiet enough to obtain ICAO noise certification at the lowest "chapter" possible. Since the total noise is dependent on the mounting of an engine on an aircraft, the most obvious measurement technique is the *flyover* measurement. In this technique an aircraft is flown over a number of microphones in various flight patterns, and measurements of the noise are made. These measurements may be a simple reproduction of the ICAO testing technique, or may use phased array beamforming techniques to locate and quantify the engine noise, and other noise sources.

Beamforming is achieved using a large array of microphones underneath the flight path of the aircraft. The signals from each microphone are delayed in time and summed such that the noise originating from a particular point sums coherently, and noise from other points sums incoherently, and is suppressed. This is known as a delay-and-sum beamformer. As the aircraft flies overhead, the time delays are modified to track the motion of the aircraft.

The first such example of the potential of the delay-and-sum beamforming technique was presented by Howell *et al.* [4], who used an array of 16 microphones to locate and quantify the engine sources on a Boeing 757 as it flew overhead. The sophistication and complexity of flyover beamforming measurements continues to increase. Recent examples include large-scale measurement campaigns in the USA and Europe presented for example by Brusniak *et al.* [5] and Guérin and Michel [6], where arrays containing hundreds of microphones are used. Figure 1.1 is an example of the source-strength maps obtainable from these kind of flyover measurements.

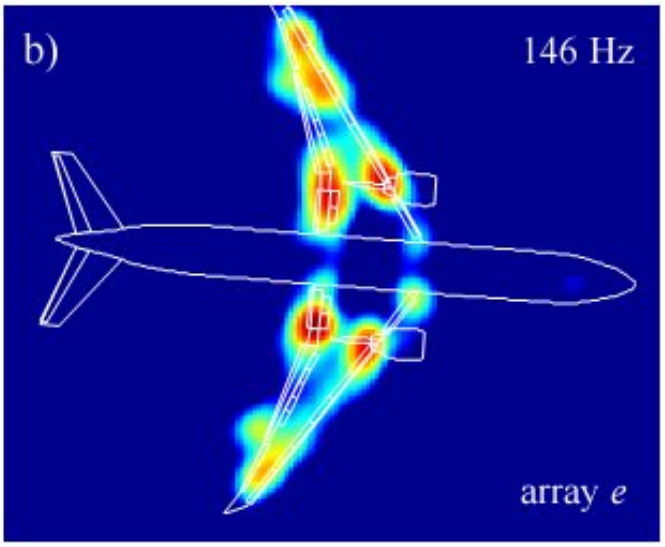

FIGURE 1.1: A sample beamformer output contour obtained by Brusniak *et al.* [5] from flyover measurements of the Quiet Technology Demonstrator 2 (QTD2) aircraft. The array used had a diameter of 76 m and contained 250 microphones. Post-processing of the data using time-domain beamforming reveals the location of sources on the aircraft. [Reproduced from Brusniak *et al.* [5] with permission]

The disadvantages of the flyover measurement technique are the costs and complexity involved, and also the difficulty in interpreting results when factors such as atmospheric propagation are taken into account. As a method to characterise aeroengine noise, flyover measurements are only able to give an indication of the relative level of the engine compared to, for example, airframe noise at different points along the flight path. No knowledge of the in-duct sound field, the noise sources inside the engine, or accurate measurement of the directivity is gained.

Static engine tests

Static engine tests are also employed to measure the noise of the engine in isolation. These tests involve the use of a single engine, usually in an outdoor test facility. Far-field directivity can be accurately measured using an array of microphones, and the

measurement of overall noise levels is the subject of a *Society of Automotive Engineers* standard [7]. Extrapolation of these measurements to equivalent in-flight noise levels has been the focus of further research [8, 9, 10, 11]. Measurement techniques have also been developed to locate and quantify the contributing engine noise sources. Examples of this include polar correlation [12, 13, 14], beamforming [15, 16] and near-field inversion methods [17, 18, 19, 20].

In-duct measurement techniques

Flyover and static-engine tests are costly, and since the engines used are difficult to modify, these tests do not readily allow the investigation of new noise control methods. For this reason, model-scale tests are often performed as they provide realistic aerodynamic conditions while at the same time being easy to modify and instrument with sensors. A disadvantage of model-scale tests is that direct measurement of radiated noise is often impractical. Model-scale tests are often carried out indoors, where either anechoic facilities do not exist for the measurement of radiated noise, or measurement is impossible due to mechanical constraints (venting of gasses for example). Because of this, acoustic measurements are often restricted to locations *within* the bypass duct or inlet duct. A recent example of a model-scale engine rig is the AneCom facility in Germany, in which Rolls-Royce have a stake. At this facility only far-field directivity in the forward arc is directly measureable.

In-duct measurement techniques can be used to locate and quantify individual noise sources in the model-scale engine, and to measure the in-duct sound field. Comparatively few such measurement techniques exist, and this thesis proposes three new techniques. The following is a survey of the existing literature.

The most comprehensive experimental investigation of broadband noise undertaken to date was performed by Ganz *et al.* at NASA, using the Boeing 18-inch fan rig [21]. This test was unique in that it used a modular fan design whereby the stators could be removed and the casing boundary layer sucked away. By measuring the broadband noise with and without stators and boundary layer present, they were able to estimate the individual contribution to the overall noise from sources within the engine. Figure 1.2 is a result from their report showing the breakdown of inlet-radiated broadband fan noise at 70% fan speed. It shows that the strength of the rotor sources, stator sources and the contribution from the rotor interacting with the boundary layer are comparable to within 5dB. Therefore, a measurement technique that could determine their individual contributions *in-situ*, such as that proposed in chapter 3 would be useful.

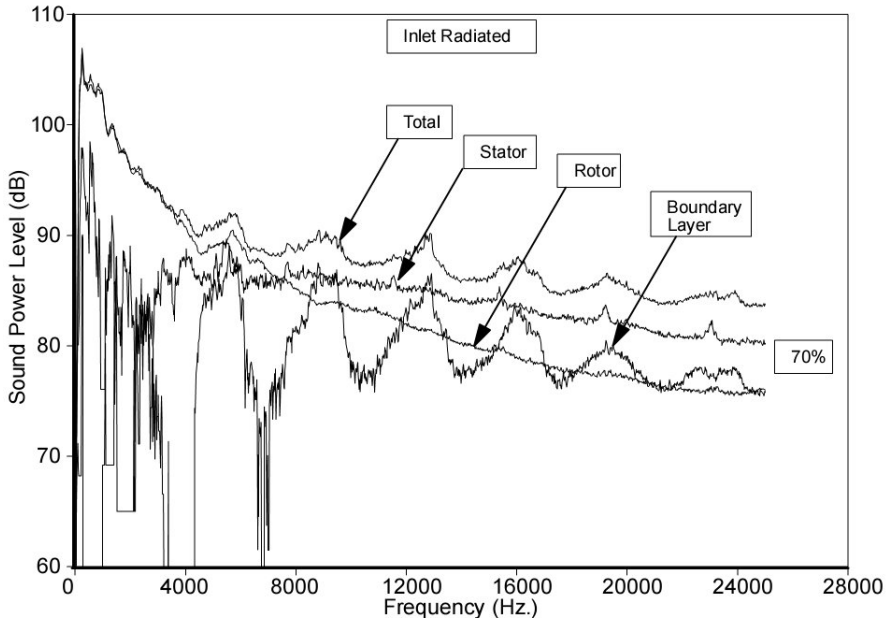

FIGURE 1.2: Inlet-radiated broadband fan noise at spectra at 70% fan speed. By physically removing components of the engine Ganz and co-authors [21] broke down the total noise into its stator, rotor and boundary-layer components. [Reproduced from Ganz *et al.* [21] with permission]

Modal analysis

The sound field propagating within a duct can be expressed as the sum of "modes". Each mode is a eigensolution of the wave equation which satisfies the boundary conditions. In-duct modal analysis is a measurement technique to deduce the amplitude of each modal component from measurements of pressure made inside the duct and represents a complete characterisation of the ducted sound field.

In the context of aeroengine noise, the first experimental attempt to decompose all propagating modes in an axial-flow fan rig was presented by Bolleter and Crocker [22]. Their technique used two microphones, one acting as a phase reference, while the other was moved to various positions in the duct. By forming a cross-spectral matrix between all the measurement positions, and formulating a model of the sound field due to incident and reflected modes, modal amplitudes up to a frequency of $ka \approx 15$ were determined. To validate the technique the dominant modes measured were compared with those predicted by Tyler and Sofrin [23] and were found to be in agreement. Modal analysis of aeroengine tonal noise has since become a well established and often-used technique.

Modal analysis of broadband noise, however, is a comparatively less well developed technique. Broadband noise generated by the fan causes all propagating modes to carry energy. As the number of modes increases, more microphones are required to accurately decompose the sound field. This involves either using an array with a large number of fixed microphones, as employed by Ganz [21] for example, or by using a smaller number

of microphones that can rotate around the duct axis. To use a rotating microphone array, a known phase reference, such as that provided by a single stationary microphone is required. Enghardt *et al.* [24, 25] have recently proposed techniques to allow the decomposition of broadband sound fields with up to 150 propagating modes. The determination of sound-power from the summation of the power in each individual mode is shown to agree well with the existing ISO standardised in-duct sound-power measurement technique [26].

Far-field directivity can be estimated using a complete modal decomposition, providing an accurate prediction of how each mode propagates to the far-field can be made. The measurement time and complexity required to do this is considerable, and has motivated the development of the technique in chapter 4. Note also that whilst modal analysis techniques offer a complete description of the sound field in a duct they provide no insight into the sources of broadband noise.

In-duct inversion techniques

Inversion techniques are a class of methods that allow source strength localisation and quantification. The source of sound is modelled as a number of simple point sources whose strength can be deduced from measurements of acoustic pressure by inverting a transfer matrix of source-receiver Green's functions. Inversion techniques have been used in free-field applications [27, 28, 29] where the radiation paths can be modelled by simple analytical Green's functions.

The first attempt to apply inversion techniques to stationary sources in a duct was proposed by Kim and Nelson [30]. An analytic hard-walled, finite length, no-flow duct Green's function was used to determine the source strength and location of a single stationary loudspeaker in a duct of 0.315 m radius with one open, and one anechoically terminated end. The radial and axial locations of the source was assumed to be known, and the technique was used to determine the azimuthal position, and the strength of the source. At a normalised frequency of $ka = 1.57$ the azimuthal location of the source could be determined to within 30° and its strength to within 3dB when acoustic pressure measurements were made 0.05 m (approx 0.04λ) from the source plane. Using numerical simulations Kim and Nelson showed that to achieve higher spatial resolution, measurements have to be made in the near field of the sources. This finding is consistent with the requirements of acoustic near field holography [31].

Kim and Nelson used a Green's function obtained from a numerical model, however Holland [32] has shown that, in a reverberant environment, measured Green's functions can also be used in inversion techniques. This suggests that the application of inversion techniques to ducted sources is not limited by the requirement for an accurate theoretical

model of the sound propagation, provided a source-receiver Green's function can be measured.

The technique proposed by Kim and Nelson is restricted to stationary sources. It cannot be applied in aeroengine problems for the determination of sources on the rotating fan blades. Chapter 2 (also Lowis and Joseph [33]) addresses this problem by introducing a Green's function which is valid for rotating sources. Another limitation of inversion techniques is that problems quickly become ill-conditioned when the number of sources to be deduced increases (at higher frequencies, or with more blades for example). Beamformer techniques address this limitation by focusing a phased array over a region measuring the apparent source strength distribution.

In-duct beamforming techniques

In addition to the flyover source location problem mentioned above, beamformer techniques are now routinely used to locate aeroacoustic sources on stationary objects, for example on an airfoil slat in a wind-tunnel [34], the distributed sources contributing to trailing edge noise [35] and during scale aircraft model wind tunnel tests [36]. Dougherty [37] presents a comprehensive review of recent advances in aeroacoustic beamforming theory. Although these techniques are frequently used, little work has been done on the application of beamforming for the location and quantification of rotating sources within a duct.

The development of a beamformer to identify free-field sources in the rotating reference frame was first undertaken by Sijtsma *et al.* [38, 39], in order to locate sources on open rotors in wind-tunnels, and on wind-turbines. Their work, based in the time-domain, introduced a transfer function that relates the source strength in the rotating reference frame to a stationary microphone position. Recent work by Sijtsma [40] and the present author (chapter 3 and [41]) has extended this technique to the quantification of ducted sources. The advantages and disadvantages of the technique proposed by Sijtsma and the one in this thesis are discussed in section 3.3.

1.3 Conclusions

This survey of the literature has indicated that to date there are no satisfactory experimental techniques which allow the rotor and stator based broadband sources to be individually differentiated. A lack of techniques that allow far-field directivity to be estimated from in-duct measurements has also been identified. In conclusion,

- Measurement techniques are an important tool for the aeroengine manufacturer. Full-scale aircraft and static engine tests are accurate, but expensive ways of assessing the noise generated by new engines. Rig tests have many advantages, but require in-duct measurement techniques.

- In-duct measurement techniques have been developed for the characterisation of aeroengine noise. Research has concentrated on the measurement of tonal noise due to rotor-stator interaction. Comparatively little work has been undertaken on source location in the rotating reference frame, and on the measurement of broadband noise.

- This thesis presents an inversion technique and a beamformer technique to locate and quantify rotating, and stationary, broadband sources using in-duct microphone arrays.

- This thesis also presents a technique to estimate far-field broadband directivity patterns using an in-duct microphone array. This technique is particularly useful in rig tests where direct measurement of radiated noise is impossible.

Chapter 2

Determining the strength of rotating ducted sources by inverse methods

2.1 Introduction

This chapter describes an experimental method for determining the broadband acoustic source strength distribution over the surface of a ducted rotor using pressure measurements made at the duct wall.

This chapter extends an inversion technique proposed by Kim and Nelson [30] for determining the strength of stationary, ducted sources to the inversion of *rotating*, *broadband*, aerodynamic sources on a ducted rotor. The equivalent uncorrelated sources in this case are shown to be separated by a correlation length that will be shown to be typically an order of a magnitude smaller than an acoustic wavelength. The resolution of sources at this separation distance necessitates the use of pressure measurements made in the near field of the rotor. The novel aspect of this measurement procedure is that it provides a means to remove the effect of source rotation and hence allows the inversion of ducted broadband sources in the rotating reference frame.

2.2 Theory

2.2.1 Sound field due to a rotating dipole source distribution in an infinite duct with flow

Consider an infinite hard-walled cylindrical duct containing a uniform axial mean flow as shown in figure 2.1. The convected wave equation is

$$\left(\frac{1}{c^2}\frac{D^2}{Dt^2} - \nabla^2\right) p = 0 \tag{2.1}$$

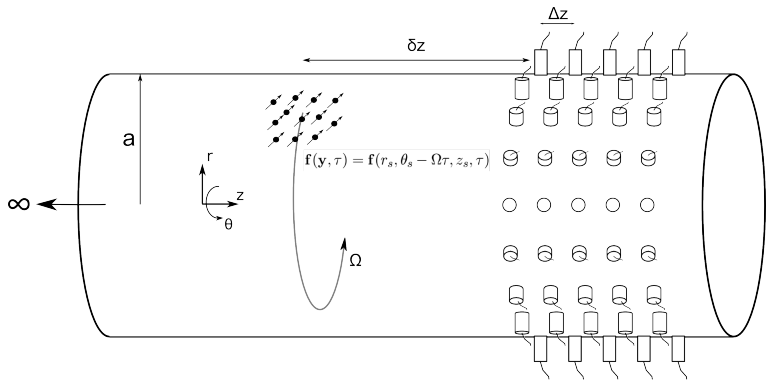

FIGURE 2.1: A dipole source distribution rotating at angular speed Ω radiates sound in an infinite hard-walled cylindrical duct with superimposed mean flow.

where $D/Dt = \partial/\partial t + cM(\partial/\partial z)$ is the convected derivative operator associated with a mean flow velocity of cM in the axial direction, and c is the speed of sound in a uniform medium.

The broadband acoustic source strength distribution due to a rotating fan blade is represented by acoustic dipole sources distributed over the blade surfaces with specified spatial and frequency correlation characteristics. The sources, with dipole moment distribution specified by $\mathbf{f}(\mathbf{y},\tau) = \mathbf{f}(r_s, \theta_s - \Omega\tau, z_s, \tau)$, are assumed to rotate around the duct axis in the θ-direction at an angular frequency Ω.

In the absence of stator vanes, the dominant broadband noise sources are situated on the rotor, and arise due to the interaction of the turbulent boundary produced on the surface of the rotor blades with the fan blade trailing edges.

Putting $\mathbf{f}(\mathbf{y},\tau) = f(\mathbf{y},\tau)\hat{\mathbf{n}}(\mathbf{y})$, where $\hat{\mathbf{n}}(\mathbf{y})$ is the unit vector normal to the blade surface, S, the time-varying pressure at any receiver point $\mathbf{x} = (r,\theta,z)$ within the duct can be calculated from the Green's function solution to the wave equation (2.1),

$$p(\mathbf{x},t) = \int_{-\infty}^{+\infty} \int_S f(\mathbf{y},\tau)\hat{\mathbf{n}}(\mathbf{y}) \cdot \nabla G(\mathbf{x},t|\mathbf{y},\tau) dS(\mathbf{y}) d\tau \tag{2.2}$$

where $f(\mathbf{y},\tau)$ is the magnitude of the dipole source strength distribution over the surface of the rotor blades. Note that source position is a function of emission time τ, $\mathbf{y} = \mathbf{y}(\tau)$.

The Green's function solution for an infinite, hard-walled cylindrical duct containing an axial uniform mean flow with Mach number M may be expressed as a superposition of an infinite number of modes given by, amongst others, Goldstein [48],

$$G(\mathbf{x},t|\mathbf{y},\tau) = \frac{\mathrm{i}}{4\pi} \sum_{m=-\infty}^{\infty} \sum_{n=0}^{\infty} \frac{\psi_{mn}(r)\psi^*_{mn}(r_s)e^{\mathrm{i}m(\theta-\theta_s)}}{\Lambda^2_{mn}} \int_{-\infty}^{\infty} \frac{e^{\mathrm{i}\omega(t-\tau)}e^{-\mathrm{i}\gamma^{\pm}_{mn}(z-z_s)}}{\kappa_{mn}(\omega)} d\omega \tag{2.3}$$

where ψ_{mn} denotes the radial mode shape function of the $(m,n)^{th}$ mode, which in a hollow duct of radius a has the form,

$$\psi_{mn}(r) = J_m(\sigma_{mn}\frac{r}{a}) \tag{2.4}$$

where J_m is the first-order Bessel function of order m. In a hard-walled cylindrical duct, σ_{mn} is the n^{th} stationary point of the Bessel function of order m. The term Λ_{mn}^2 is a normalisation constant (see appendix A).

Substituting the Green's function of equation (2.3) into the convective wave equation leads to the following expressions for the mode wavenumbers [49],

$$\gamma_{mn}^{\pm} = \frac{-Mk \mp \kappa_{mn}}{1-M^2}, \quad \kappa_{mn} = \sqrt{k^2 - (1-M^2)(\frac{\sigma_{mn}}{a})^2} \tag{2.5}$$

Modes can propagate unattenuated when κ_{mn} is real. From equation (2.5) this leads to an expression for the cut-on frequency associated with each mode. In normalised duct-frequency units, it is given by

$$(ka)_{mn} = \sigma_{mn}\sqrt{1-M^2} \tag{2.6}$$

At a frequency below the cut-on frequency the modes decay exponentially along the duct.

A dipole source aligned at an angle α relative to the duct axis has components of $\hat{\mathbf{n}}$ given by

$$\hat{\mathbf{n}} = [\hat{r}, \hat{\theta}, \hat{z}] = [0, \sin\alpha, \cos\alpha] \tag{2.7}$$

where in general $\alpha = \alpha(\mathbf{y})$. The ∇ operator in cylindrical coordinates is given by

$$\nabla G = \hat{r}_s\frac{\partial G}{\partial r_s} + \frac{\hat{\theta}}{r_s}\frac{\partial G}{\partial \theta_s} + \hat{\mathbf{z}}\frac{\partial G}{\partial z_s} \tag{2.8}$$

Substituting equation (2.3) into equation (2.8) gives the non-zero components of ∇G as

$$\frac{\hat{\theta}}{r_s}\frac{\partial G}{\partial \theta_s} = \frac{\mathrm{i}\hat{\theta}}{4\pi}\sum_{m=-\infty}^{\infty}\frac{-\mathrm{i}m}{r_s}\sum_{n=0}^{\infty}\frac{\psi_{mn}(r)\psi_{mn}^*(r_s)e^{\mathrm{i}m(\theta-\theta_s)}}{\Lambda_{mn}^2}\int_{-\infty}^{\infty}\frac{e^{\mathrm{i}\omega(t-\tau)}e^{-\mathrm{i}\gamma_{mn}^{\pm}(z-z_s)}}{\kappa_{mn}(\omega)}d\omega \tag{2.9}$$

$$\hat{\mathbf{z}}\frac{\partial G}{\partial z_s} = \frac{\mathrm{i}\hat{\mathbf{z}}}{4\pi}\sum_{m=-\infty}^{\infty}\sum_{n=0}^{\infty}\mathrm{i}\gamma_{mn}^{\pm}\frac{\psi_{mn}(r)\psi_{mn}^*(r_s)e^{\mathrm{i}m(\theta-\theta_s)}}{\Lambda_{mn}^2}\int_{-\infty}^{\infty}\frac{e^{\mathrm{i}\omega(t-\tau)}e^{-\mathrm{i}\gamma_{mn}^{\pm}(z-z_s)}}{\kappa_{mn}(\omega)}d\omega \tag{2.10}$$

Substituting equations (2.9) and (2.10) into equation (2.2) gives

$$p(\mathbf{x},t) = \frac{1}{2\pi}\int_{-\infty}^{\infty}\int_{S} f(\mathbf{y},\tau)\sum_{m=-\infty}^{\infty}\int_{-\infty}^{\infty} g_m(\mathbf{y},z,r,\omega)e^{\mathrm{i}m\theta}e^{\mathrm{i}\omega(t-\tau)}d\omega dS(\mathbf{y})d\tau \qquad (2.11)$$

where for conciseness a transfer impedance, g_m, has been defined which relates the pressure due to a spinning mode of order m at a frequency ω, located at $\mathbf{x} = (r, \theta = 0°, z)$, due to a point dipole source of unit source strength located at $\mathbf{y}$. It is obtained by comparing equation (2.11) with the result of substituting equations (2.9) and (2.10) into equation (2.2),

$$g_m(\mathbf{y},z,r,\omega) = \frac{1}{2}\sum_{n=0}^{\infty}\Big[-\gamma_{mn}^{\pm}\cos\alpha + \frac{m}{r_s}\sin\alpha\Big]\frac{\psi_{mn}(r)\psi_{mn}^{*}(r_s)e^{-\mathrm{i}m\theta_s}}{\Lambda_{mn}^{2}}\frac{e^{-\mathrm{i}\gamma_{mn}^{\pm}(z-z_s)}}{\kappa_{mn}(\omega)} \qquad (2.12)$$

2.2.2 Sound field produced by a broadband rotating dipole source distribution

For rotating sources the circumferential source position $\theta_s(\tau)$ in the stationary reference frame (relative to the duct) may be related to the angle $\tilde{\theta}_s$ in a rotating reference frame spinning with the rotor at an angular frequency Ω by $\theta_s = \tilde{\theta}_s - \Omega\tau$; where Ω is the shaft rotation frequency. Substituting for θ_s in equation (2.11), the expression for p becomes

$$p(\mathbf{x},t) = \frac{1}{2\pi}\int_{-T}^{T}\int_{\tilde{S}} f(\tilde{\mathbf{y}},\tau)\sum_{m=-\infty}^{\infty}\int_{-\infty}^{\infty} g_m(\tilde{\mathbf{y}},z,r,\omega)e^{\mathrm{i}m\theta}e^{\mathrm{i}\omega t-\mathrm{i}(\omega-m\Omega)\tau}d\omega d\tilde{S}(\tilde{\mathbf{y}})d\tau \qquad (2.13)$$

where $\tilde{\mathbf{y}}$ is the time-independent source position evaluated in the rotating reference frame, $\tilde{\mathbf{y}} = (r_s, \tilde{\theta}_s, z_s)$ and $\tilde{S} = \tilde{S}(\tilde{\mathbf{y}})$.

The integral over τ in equation (2.13) is of the form,

$$\int_{-\infty}^{\infty} f(\tilde{\mathbf{y}},\tau)e^{-\mathrm{i}(\omega-m\Omega)\tau}d\tau = f(\tilde{\mathbf{y}},\omega-m\Omega) \qquad (2.14)$$

and equation (2.13) can therefore be written as

$$p(\mathbf{x},t) = \frac{1}{2\pi}\int_{\tilde{S}}\sum_{m=-\infty}^{\infty} f(\tilde{\mathbf{y}},\omega-m\Omega)\int_{-\infty}^{\infty} g_m(\tilde{\mathbf{y}},z,r,\omega)e^{\mathrm{i}m\theta}e^{\mathrm{i}\omega t}d\omega d\tilde{S}(\tilde{\mathbf{y}}) \qquad (2.15)$$

Comparison of equation (2.15) with the definition of the Fourier transform,

$$p(\mathbf{x},t) = \frac{1}{2\pi}\lim_{T\to\infty}\int_{-T}^{T} p(\mathbf{x},\omega)e^{\mathrm{i}\omega t}d\omega \qquad (2.16)$$

allows equation (2.15) to be written in the frequency domain as

$$p(\mathbf{x},\omega) = \int_{\tilde{S}} \sum_{m=-m_0}^{m_0} f(\tilde{\mathbf{y}},\omega - m\Omega) g_m(\tilde{\mathbf{y}},z,r,\omega) e^{\mathrm{i}m\theta} d\tilde{S}(\tilde{\mathbf{y}}) \tag{2.17}$$

where in equation (2.17), for receivers located several wavelengths from the sources, cutoff modes can be neglected and the modal summation is confined to the propagating modes, such that m_0 is the highest propagating azimuthal mode order, and n_0 the highest propagating radial mode order.

Note that the effect of transforming the source integral to the rotating reference frame has been to shift the source frequency ω by $-m\Omega$. This finding will form the basis of the inversion procedure presented in section 2.3.

Broadband sound fields are most suitably expressed in terms of the cross-spectrum between two points $\mathbf{x}$ and $\mathbf{x}'$ in the duct, defined by

$$S_{pp}(\mathbf{x},\mathbf{x}',\omega) = \lim_{T\to\infty} \frac{\pi}{T} E\{p(\mathbf{x},\omega) p^*(\mathbf{x}',\omega)\} \tag{2.18}$$

where E denotes the expectation value.

Substituting equation (2.17) into equation (2.18) gives the following expression for S_{pp}

$$\begin{aligned} S_{pp}(\mathbf{x},\mathbf{x}',\omega) = \int_{\tilde{S}} \int_{\tilde{S}'} \sum_{m=-m_0}^{m_0} \sum_{m'=-m_0}^{m_0} & S_{ff}(\tilde{\mathbf{y}},\tilde{\mathbf{y}}',\omega - m\Omega, \omega - m'\Omega) \times \\ & \times g_m(\tilde{\mathbf{y}},z,r,\omega) g^*_{m'}(\tilde{\mathbf{y}}',z,r',\omega) e^{\mathrm{i}m\theta - \mathrm{i}m'\theta'} d\tilde{S}(\tilde{\mathbf{y}}) d\tilde{S}(\tilde{\mathbf{y}}') \end{aligned} \tag{2.19}$$

where

$$S_{ff}(\tilde{\mathbf{y}},\tilde{\mathbf{y}}',\omega,\omega') = \frac{\pi}{T} E\{f(\tilde{\mathbf{y}},\omega) f^*(\tilde{\mathbf{y}}',\omega')\} \tag{2.20}$$

Equation (2.19) is an expression for the pressure cross-spectrum between any two points in the duct due to a rotating dipole source distribution with spatial and frequency cross-spectrum S_{ff} (in the rotating reference frame). Note that for rotating sources, $\Omega \neq 0$, the source strength and its propagation become coupled through the spinning mode index m. This is the reason why conventional inversion procedures, valid for stationary sources, for example as described by Kim and Nelson [30], cannot be applied to rotating sources. An alternative procedure is proposed in section 2.3.

2.3 Inversion technique for ducted rotating sources

This section is concerned with an inversion technique to determine the broadband strengths of rotating broadband sources in a duct from a number of measurements of acoustic pressure made at the duct wall. We show below that their determination by existing inverse

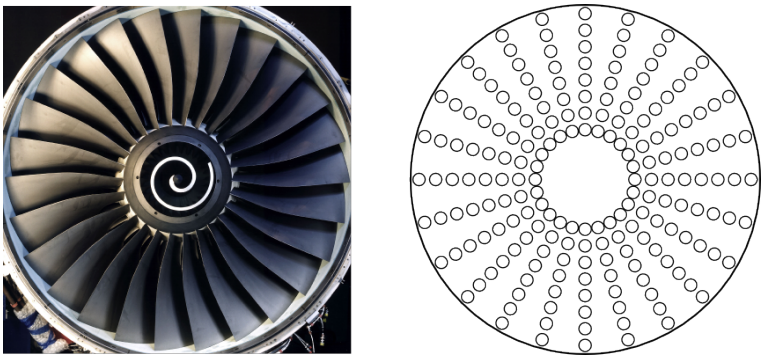

FIGURE 2.2: An acoustic inversion problem is formulated by replacing the real acoustic source (left) with an equivalent distribution of discrete model sources (right)

methods cannot be performed. A new technique for the inversion of rotating broadband sources is therefore proposed. Simulation results are presented to illustrate the various properties of the new inversion technique. Before presentation of the technique for inverting rotating sources, we first review the theory for the inversion of stationary source strengths. We will show subsequently that by appropriately processing the measured pressure signals, and by the introduction of a modified Green's function, the theory for the inversion of rotating sources may be written in an identical form to that for stationary sources.

2.3.1 Inversion techniques for stationary sources

Inverse techniques require the approximation of a continuous source region by a finite number of discrete sources (figure 2.2). The objective of the inversion procedure is to deduce the vector of optimal discretized source strengths, $\hat{\mathbf{f}}$, which in a model of the radiated sound field, $\mathbf{p} = \mathbf{G}\mathbf{f}$, matches, in a least squares sense, the pressure $\hat{\mathbf{p}}$ measured at an array of microphones, where $\mathbf{G}$ is a matrix of transfer impedances, which may be measured or predicted.

At a single frequency the vector of pressures $\mathbf{p}$ due to a discretized *stationary* source distribution $\mathbf{f}$ can be written in the form,

$$\mathbf{p} = \mathbf{G}\mathbf{f} \tag{2.21}$$

where $\mathbf{G}$ is a matrix of transfer impedances that relates the assumed source distribution $\mathbf{f}$ to the vector of predicted pressures at the sensors. The $(i,j)^{th}$ element of $\mathbf{G}$ specifies the transfer impedance between the i^{th} source and the pressure at the j^{th} sensor. Note that, as indicated in equation (2.15), when there is relative motion between the source and receiver, the source and receiver frequencies are no longer identical.

In practice, the measured pressure signals are contaminated by "noise". Noise could be introduced by errors in the measurements and also by inaccuracies in the model of $\mathbf{G}$.

We therefore write the vector of measured pressures $\hat{\mathbf{p}}$ as the sum of the "noise-free" perfectly predicted measurements and an error term, $\mathbf{e}$,

$$\hat{\mathbf{p}} = \mathbf{G}\mathbf{f} + \mathbf{e} \tag{2.22}$$

The optimal source strength vector $\mathbf{f}$ that minimises the sum of squared errors $\mathbf{e}^H\mathbf{e}$, for the case where there are equal numbers of sources and sensors, is given by

$$\mathbf{f} = \mathbf{G}^{-1}\hat{\mathbf{p}} \tag{2.23}$$

where H denotes the Hermitian transpose operator.

More generally, if there are more sensors than sources then the system of equations in (2.23) is over-determined. In this case $\mathbf{G}$ is non-square and the optimum solution is given by

$$\mathbf{f} = \mathbf{G}^{+}\hat{\mathbf{p}} \tag{2.24}$$

where $\mathbf{G}^{+} = [\mathbf{G}^H\mathbf{G}]^{-1}\mathbf{G}^H$ is the pseudo-inverse of $\mathbf{G}$.

2.3.2 Application of the inversion technique to stationary broadband sources

Consider the cross-spectral matrix of measured pressures $\mathbf{S}_{\hat{\mathbf{p}}\hat{\mathbf{p}}}(\omega)$, defined by

$$\mathbf{S}_{\hat{\mathbf{p}}\hat{\mathbf{p}}} = \frac{\pi}{T}E\{\hat{\mathbf{p}}\hat{\mathbf{p}}^H\} \tag{2.25}$$

Substituting equation (2.21) into (2.25) gives

$$\mathbf{S}_{\hat{\mathbf{p}}\hat{\mathbf{p}}} = \mathbf{G}\mathbf{S}_{\mathbf{ff}}\mathbf{G}^H \tag{2.26}$$

where

$$\mathbf{S}_{\mathbf{ff}} = \frac{\pi}{T}E\{\mathbf{f}\mathbf{f}^H\} \tag{2.27}$$

Similarly, to determine $\mathbf{S}_{\mathbf{ff}}$ from $\mathbf{S}_{\hat{\mathbf{p}}\hat{\mathbf{p}}}$, equation (2.24) is substituted into equation (2.27) to give

$$\mathbf{S}_{\mathbf{ff}} = \mathbf{G}^{+}\mathbf{S}_{\hat{\mathbf{p}}\hat{\mathbf{p}}}(\mathbf{G}^{+})^H \tag{2.28}$$

Note that the general expression for the pressure cross-spectrum given by (2.19) for rotating sources *cannot* be formulated in the form of equation (2.26) for stationary sources. The inversion procedure of equation (2.28) therefore does not apply to rotating sources. The essential difficulty, as made explicit by equation (2.19), is that the receiver and source frequencies are no longer the same. A procedure for determining the source strength in

the rotating reference frame must therefore remove the effects of source rotation. Such a procedure is proposed below.

2.3.3 Inversion of rotating broadband sources

We begin with equation (2.17) for the pressure produced by a rotating single-frequency source distribution. Owing to the periodicity of the sound field in the θ direction, the pressure at the duct wall ($r = a$) at axial position z, sensed by N microphones at positions θ_i, can be written as a discrete Fourier series expansion with the coefficients

$$p_m(z,a,\omega) = \frac{1}{N}\sum_{i=1}^{N} p(a,\theta_i,z,\omega)e^{-\mathrm{i}m\theta_i} \qquad (\frac{-|1-N|}{2} \leq m \leq \frac{N}{2}) \tag{2.29}$$

this spinning mode decomposition gives the pressure amplitude, p_m, of the m^{th} mode at the duct wall, and satisfies the Shannon sampling rate. Substituting equation (2.17) into equation (2.29) gives

$$p_m(z,a,\omega) = \int_{\tilde{S}} f(\tilde{\mathbf{y}},\omega - m\Omega)g_m(\tilde{\mathbf{y}},z,a,\omega)d\tilde{S}(\tilde{\mathbf{y}}) \tag{2.30}$$

from which we may write,

$$p_m(z,a,\omega + m\Omega) = \int_{\tilde{S}} f(\tilde{\mathbf{y}},\omega)g_m(\tilde{\mathbf{y}},z,a,\omega + m\Omega)d\tilde{S}(\tilde{\mathbf{y}}) \tag{2.31}$$

Equation (2.31) suggests that the source spectrum at the unshifted frequency $f(\tilde{\mathbf{y}},\omega)$ (i.e. observed in the rotating reference frame), can be deduced from measurements of the spinning mode amplitude $p_m(\mathbf{x},\omega + m\Omega)$ and measurements (or predictions) of $g_m(\tilde{\mathbf{y}},z,a,\omega + m\Omega)$ at a shifted frequency of $\omega + m\Omega$. The frequency shift is introduced to remove the effects of source rotation.

This frequency-shifted mode amplitude measurement p_m is now used to define a pressure spectrum $p_\Omega(\mathbf{x},\omega)$, given by

$$p_\Omega(\mathbf{x},\omega) = \sum_{m=-m^-}^{m^+} p_m(z,a,\omega + m\Omega)e^{\mathrm{i}m\theta} \tag{2.32}$$

where the subscript Ω on p is used to distinguish this pressure from the directly measurable pressure defined in equation (2.17). In appendix C we show that the pressure p_Ω defined by equation (2.32) is precisely the same as that measured by a microphone rotating around the duct axis at the same angular speed as the rotor.

Note that the upper and lower limits of m in equation (2.32), $m^\pm$, specifying the range of propagating modes, differ from those in equation (2.17), $\pm m_0$ which contribute to the

pressure measured by a stationary microphone in the duct. In equation (2.32), as m increases, so the frequency, $\omega + m\Omega$, at which the modal components p_m are evaluated also increases. Hence the summation over propagating modes has to be made over the new range of spinning mode orders, $-m^- \leq m \leq m^+$. The variation of m^+ and m^- with ka and Ω is examined in section 2.3.4.

Substituting equation (2.31) into (2.32) leads to a relationship between the pressure p_Ω and the source strength $f(\tilde{\mathbf{y}})$, as observed in the rotating reference frame, $\tilde{\mathbf{y}}$,

$$p_\Omega(\mathbf{x},\omega) = \int_{\tilde{S}} f(\tilde{\mathbf{y}},\omega) \sum_{m=-m^-}^{m^+} g_m(\tilde{\mathbf{y}},z,r,\omega+m\Omega)e^{\mathrm{i}m\theta} d\tilde{S}(\tilde{\mathbf{y}}) \tag{2.33}$$

By exact analogy with the expression for stationary source distributions, equation (2.33) for rotating sources can be formulated more generally as

$$p_\Omega(\mathbf{x},\omega) = \int_{\tilde{S}} f(\tilde{\mathbf{y}},\omega)\hat{\mathbf{n}}(\tilde{\mathbf{y}}) \cdot \nabla G_\Omega(\tilde{\mathbf{y}},\mathbf{x},\omega) d\tilde{S}(\tilde{\mathbf{y}}) \tag{2.34}$$

where G_Ω is a hard-walled duct Green's function, which has been modified to incorporate the effects of source rotation, given by

$$G_\Omega(\tilde{\mathbf{y}},\mathbf{x},\omega) = \frac{\mathrm{i}}{4\pi} \sum_{m=-m^-}^{m^+} \sum_{n=0}^{n_0} \frac{\psi_{mn}(r)\psi^*_{mn}(r_s)e^{\mathrm{i}m(\theta-\tilde{\theta}_s)}}{\Lambda^2_{mn}} \frac{e^{-\mathrm{i}\gamma^\pm_{mn}(z-z_s)}}{\kappa_{mn}(\omega+m\Omega)} \tag{2.35}$$

and $\gamma^\pm_{mn}$ is evaluated at the shifted frequency $\omega + m\Omega$. Note that putting $\Omega = 0$ in equations (2.34) and (2.35) recovers equation (2.2) (expressed in the frequency domain) for the pressure due to stationary sources.

Equations (2.34) and (2.35) are therefore a generalised formulation of equation (2.2) for the acoustic pressure at a single frequency, which allows for the effects of source rotation. It is identical in form to that for stationary sources, and is suitable for inversion using existing techniques.

The analogous expression to equation (2.28) for the cross-spectrum of discretized rotating sources in the rotating reference frame in terms of the modified Green's function, $\mathbf{G}_\Omega$, is given by

$$\mathbf{S_{ff}} = \mathbf{G}^+_\Omega \mathbf{S}_{p_\Omega p_\Omega} (\mathbf{G}^+_\Omega)^H \tag{2.36}$$

Equation (2.36) suggests that by use of this modified Green function, G_Ω, the inversion procedure required to recover the source cross spectrum $\mathbf{S}_{ff}(\tilde{\mathbf{y}},\tilde{\mathbf{y}}',\omega)$ in the rotating reference frame from measurements of the pressure cross spectrum $\mathbf{S}_{p_\Omega p_\Omega}(\mathbf{x},\mathbf{x}',\omega)$ can be carried out in precisely the same way as for stationary broadband sources (section 2.3.2). The important difference is that now the pressure cross spectrum is computed

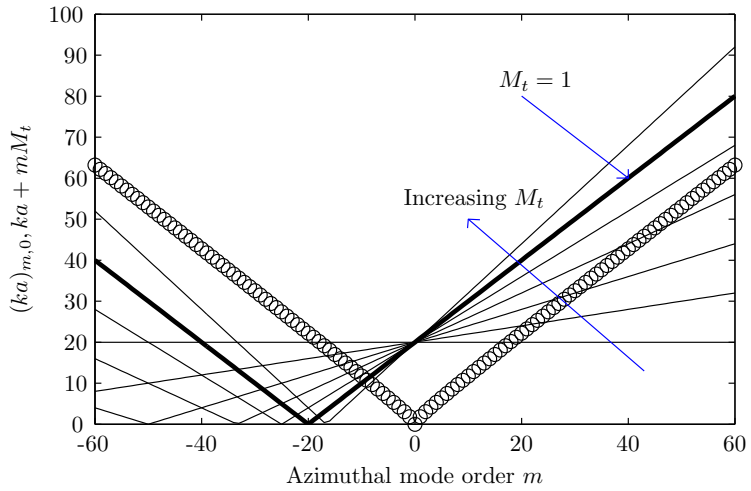

FIGURE 2.3: A plot of azimuthal mode cut-on frequencies $(ka)_{m,0}$ (line with circles) and the left hand side of the cut-on condition $ka + mM_t$ (solid line) (equation 2.37) versus mode order m. The solid lines are M_t values of 0 (horizontal) to 1.2 in $0.2M_t$ increments at normalised frequency $ka = 20$. Points of intersection define $m^{\pm}$.

from p_Ω, which first requires a spinning mode decomposition of the sound field to be performed.

Equations (2.35) and (2.36) form the main results of this chapter. Their effectiveness for deducing the source strength of rotating source distributions is explored in section 2.3.5. We first consider the determination of m^+ and m^-, corresponding to the range of propagating spinning modes contributing to p_Ω and $\mathbf{G}_\Omega$.

2.3.4 Determination of m^+ and m^-

The upper and lower modal orders m^+ and m^- appearing in equation (2.35) specify the range of propagating spinning modes that have to be included in the calculation of p_Ω and $\mathbf{G}_\Omega$ for sensors outside the near field of the rotor. With reference to equation (2.31), at least one radial mode of order m can propagate at a frequency $\omega + m\Omega$ providing $|\omega + m\Omega| > \omega_{m,0}$, where $\omega_{m,0}$ is the cutoff frequency of the lowest order radial mode $n = 0$. This cut-off condition may be written in non-dimensional form as

$$|ka \pm mM_t| \geq (ka)_{m,0} \tag{2.37}$$

where $(ka)_{m,0} = \sigma_{m,0}\sqrt{1 - M^2}$ from equation (2.6), $M_t = \Omega a/c$ is the blade tip Mach number and ka is the non-dimensional observer frequency. Figure 2.3 is a plot of the left hand side of equation (2.37) (solid line) at $ka = 20$ for a range of blade tip Mach numbers between 0 and 1.2. Also shown, indicated by circles, is the cut-on frequency $(ka)_{m,0}$, corresponding to the right hand side of equation (2.37). As indicated in equation (2.37) the mode m contains at least one propagating radial mode and must be included in the modal summation for m-values when when the solid line is above the circles.

Figure 2.3 shows that for supersonic tip speeds, $M_t > 1$, the cut-off condition of equation (2.37) is satisfied for all m-values, $m > 0$, since the two curves diverge for positive m. This suggests that all co-rotating spinning ($m > 0$) modes to infinity must be included in the modal summation of p_Ω and G_Ω in equation (2.35). However only a finite number of counter-rotating modes ($m < 0$) must be included. At the sonic blade tip speed $M_t = 1$, the cut-on frequency and "excitation frequency", $ka + mM_t$, increase with m at exactly the same rate and the curves run exactly parallel. Again all co-rotating mode orders to infinity must be included in p_Ω and G_Ω. For subsonic tip speeds, $M_t < 1$, the two lines intersect indicating that there is always a finite range of co- and counter-rotating propagating mode orders that have to be included in the modal summation. Note that for $m < 0$, irrespective of M_t, the two curves always intersect, suggesting that there is always a finite range of counter-rotating modes to be included in p_Ω and G_Ω.

A good estimate for $m^\pm$ is obtained by noting that for suitably high m-values, in the absence of axial flow, the angular phase velocity c_p of the mode m at the duct wall is given by $c_p = a\omega/m$, which must exceed the speed of sound c_0 in order to propagate. Recall that p_Ω is identical to the pressure measured by a microphone rotating around the duct wall at the shaft rotational frequency Ω. In this rotating reference frame, the cut-off condition becomes $c_p - a\Omega > c_0$. Substituting the approximation to c_p given above, this condition may be written as [1].

$$\frac{ka}{m} - M_t \geq 1 \tag{2.38}$$

Solving for $m = m^\pm$ in equation (2.37) gives

$$m^\pm = \frac{ka}{1 \mp M_t} \tag{2.39}$$

Equation (2.39) confirms that $m^+ \to \infty$ as $M_t \to 1$, as predicted by figure 2.3.

2.3.5 Source resolution limits of the inversion technique for sensor arrays outside the near field of the rotor

We now quantify the resolution limits of the inversion technique, i.e how closely two sources may be discriminated. We assume that the microphone arrays used are positioned at a distance far enough away from the source plane that the effect of evanescent modes on the measured pressure is negligible. The application of the inversion technique for rotating sources, given by equation (2.36), relies on being able to accurately invert the matrix $\mathbf{G}_\Omega$. Error bounds on the source strength deduced from the inversion in the presence of measurement error, modelling error and other sources of noise, can be estimated from the *condition number* of $\mathbf{G}_\Omega$.

[1] Note that this cutoff condition can also be derived from equation (2.37) by noting that for large m-values, $(ka)_{m,0} \approx m$.

Consider the error $\delta\mathbf{f}$ in $\mathbf{f}$ due to errors (noise) $\delta\mathbf{p}_\Omega$ in the measured pressure $\mathbf{p}_\Omega$ under the transformation of equation (2.23),

$$\mathbf{f} + \delta\mathbf{f} = \mathbf{G}_\Omega^+(\mathbf{p}_\Omega + \delta\mathbf{p}_\Omega) \tag{2.40}$$

It can be shown [50] that the ratio of the norms of the perturbed quantities satisfies the inequality,

$$\frac{\|\delta\mathbf{f}\|}{\|\mathbf{f}\|} \leq \kappa(\mathbf{G}_\Omega)\frac{\|\delta\mathbf{p}_\Omega\|}{\|\mathbf{p}_\Omega\|} \tag{2.41}$$

where $\|\cdot\|$ denotes the matrix 2-norm and the condition number of $\mathbf{G}_\Omega$ can be calculated from

$$\kappa(\mathbf{G}_\Omega) = \|\mathbf{G}_\Omega\|\|\mathbf{G}_\Omega^+\| \tag{2.42}$$

Equation (2.41) states that the error in the reconstructed source strength vector $\mathbf{f}$ is bounded by $\kappa(\mathbf{G})$ times the relative error in the measured pressures $\mathbf{p}_\Omega$. A similar analysis shows that the error in $\mathbf{f}$ due to modelling error in the transfer matrix $\mathbf{G}_\Omega$ is bounded by

$$\frac{\|\delta\mathbf{f}\|}{\|\mathbf{f}\|} \leq \kappa(\mathbf{G}_\Omega)\frac{\|\delta\mathbf{G}_\Omega\|}{\|\mathbf{G}_\Omega\|} \tag{2.43}$$

In the following sections we investigate the effect on the conditioning of the matrix $\mathbf{G}_\Omega$ due to various assumed source distributions. These will be used to establish fundamental limits for how closely together the discrete rotating sources can be resolved. All the simulations will be performed without the addition of noise, $\delta\mathbf{p}_\Omega = 0$. Very large condition numbers ($\kappa(\mathbf{G}_\Omega) > 10^6$) will indicate that the results obtained by the inversion are likely to be very inaccurate when deduced from pressure measurements contaminated by small levels of noise.

The matrix $\mathbf{G}_\Omega$ relates the pressure $\mathbf{p}_\Omega$ measured at an array of microphones to the discretized source distribution $\mathbf{f}$. The choice of microphone positions will therefore affect the conditioning of $\mathbf{G}_\Omega$. Previous work by Kim and Nelson [30] has investigated the effect of microphone array geometry on $\kappa(\mathbf{G})$ for the case of stationary sources. Since the technique presented in this chapter allows rotating sources to be inverted in precisely the same way as for stationary sources, these findings are also relevant to this work.

Kim and Nelson have examined the effect on $\kappa(\mathbf{G})$ of various wall-mounted microphone array configurations. They showed that there must be more microphones than sources in order for the transfer matrix to be well conditioned. It was found that the arrangement of the sensors into single, or multiple, axially separated rings did not have a significant influence on the condition number. Recall that, in the present technique, the measurement of p_Ω requires a modal decomposition to be preformed. In the following simulations, therefore, the microphone array consists of a single ring of N sensors sufficient in number to

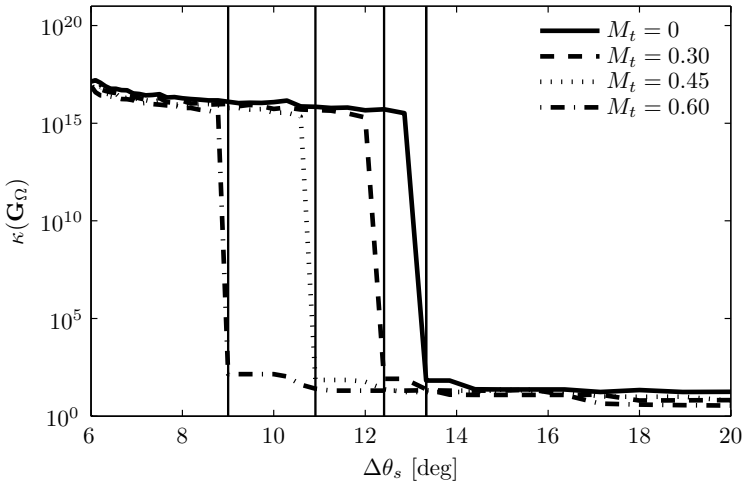

FIGURE 2.4: Conditioning of the transfer matrix $\mathbf{G}_\Omega$ at $ka = 15$, as a function of azimuthal source separation for varying rotational speeds. The vertical lines indicate the value $\frac{2\pi}{m_T}$ calculated for each rotational speed.

perform a modal decomposition at the highest frequency of interest, $N = 2m^+ + 1$, where m^+ is the highest "spatial frequency" of interest when cutoff modes can be neglected.

2.3.5.1 Angular resolution limits

We first examine, by means of a numerical simulation, the variation of $\kappa(\mathbf{G}_\Omega)$ as a function of the angular source separation angle $\Delta\theta_s$. In practical terms, this is a measure of the ability of the inversion technique to resolve sources on adjacent blades. In this simulation, N_s sources located at $r_s = 0.8a$ are arranged with an angular separation of $\Delta\theta_s = \frac{2\pi}{N_s}$. The duct contains an axial mean flow of $M = 0.2$. The simulation is performed at a frequency of $ka = 15$ for various M_t-values. Neglecting the effect of the low axial Mach number for simplicity, equation (2.39) suggests that $m^+ = \frac{15}{1-0.6} \approx 40$ at the highest M_t value under consideration here, $M_t = 0.6$, which therefore requires 80 sensors in a single ring to perform its modal decomposition. A single ring of 80 microphones is positioned 2.4λ (1 metre) downstream of the sources. At this measurement location and frequency, cutoff modes can be neglected.

The results of this simulation of $\kappa(\mathbf{G}_\Omega)$ versus $\Delta\theta_s$ as figure 2.4 (obtained by varying N_s) at different rotational speeds, M_t. As the number of sources N_s increases, an angular separation is reached where the condition number of $\mathbf{G}_\Omega$ suddenly becomes very large ($\kappa(\mathbf{G}_\Omega) > 10^{15}$) and therefore the sources can no longer be resolved.

By inspection, it is found that the angular resolution limit, $\Delta\theta_s$, below which the inversion is impractical due to poor conditioning of the transfer matrix, is given by

$$\Delta\theta_s \leq \frac{2\pi}{m_T} \tag{2.44}$$

where $m_T = m^+ + m^- + 1$ is the total number of propagating azimuthal modes included in the calculation of $\mathbf{G}_\Omega$ for a given ka and rotational frequency Ω. This limit, $2\pi/m_T$, is indicated by the vertical dotted lines in figure 2.4. For $\mathbf{G}_\Omega$ to be well-conditioned there must be more azimuthal modes included in its calculation than there are sources. As shown in figure 2.3, and quantified by equation (2.39), m^+ increases with M_t and hence the angular resolution limit of the inversion technique improves as the tip speed Mach number increases.

2.3.5.2 Frequency limits for resolving sources on B blades

The angular resolution limits presented in the previous section have practical implications for the inversion of blade-based sources in aeroengines. If a blade can be represented by dipole source distribution along the trailing edge, (or leading edge in the case of rotor/stator interaction noise where $\Omega = 0$) then in order to invert for the sources on B blades, an angular resolution of $2\pi/B$ must be possible. Putting $\Delta\theta_s = 2\pi/B$ and $m_T = m^+ + m^- + 1$ in equation (2.44), and noting equation (2.39) for m^+ and m^-, gives the following necessary, but not sufficient condition, for accurate inversion

$$\frac{ka}{1 - M_t} + \frac{ka}{1 + M_t} + 1 \gtrapprox B \tag{2.45}$$

Equation (2.45) establishes a lower frequency limit below which the sources on B blades cannot be resolved. Solving for this frequency and normalising by the Blade Passing Frequency, $(ka)_{BPF} = M_t B$, gives

$$\frac{\omega}{\omega_{BPF}} = \frac{ka}{(ka)_{BPF}} \gtrapprox \frac{(B-1)(1-M_t^2)}{2M_t B} \tag{2.46}$$

For large values of B typical of turbofan engines, equation (2.46) simplifies further to

$$\frac{\omega}{\omega_{BPF}} \gtrapprox \frac{1 - M_t^2}{2M_t} \tag{2.47}$$

Equation (2.47) predicts that in order to resolve sources above a frequency $\alpha \cdot \omega_{BPF}$ the blade tip Mach number must exceed $M_t = \sqrt{\alpha^2 + 1} - \alpha$. Source resolution above $\frac{1}{2}BPF$ and $1BPF$ for example, is only possible at rotational speeds above $M_t = \sqrt{5/4} - 1/2 \approx 0.62$ and $\sqrt{2} - 1 \approx 0.41$ respectively. This lower limit falls rapidly as M_t is increased. To demonstrate this, ω/ω_{BPF} in equation (2.47) is plotted versus M_t in figure 2.5.

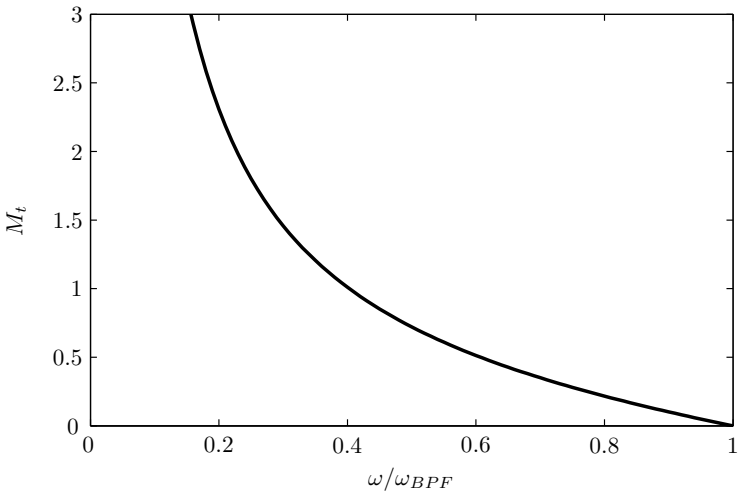

FIGURE 2.5: The lower frequency limit, ω/ω_{BPF} for resolving sources azimuthally as a function of tip speed Mach number.

2.3.5.3 Radial resolution limits

Kim and Nelson [29] have shown that a half-wavelength resolution limits exists for inversion techniques when measurements are made in the far-field of the source. Assuming that the same resolution limit can also be applied to sources in a duct resolution limit for resolving sources radially in a duct can be shown to be,

$$\frac{n_0}{N_s} > 1 \tag{2.48}$$

since n_0 may be interpreted, approximately, as the number of turning points of the mode shape function of the axi-symmetric mode $m = 0$. Correspondingly, it specifies, approximately, the number of half-wavelengths across the duct radius.

The dependence of resolution limits due to source rotation can be summarised by considering the "mode triangle", plotted in figure 2.6 for $M_t = 0$ and $M_t = 0.5$ at $ka = 50$. in which the number of radial modes is plotted against each spinning mode order included in the calculation of $\mathbf{G}_\Omega$. The result for the stationary source case, $M_t = 0$, is a symmetrical triangle. For $M_t = 0.5$, the triangle is skewed towards the co-rotating modes ($m^+ > m^-$ as explained in section 2.3.4). As predicted by equation (2.44) azimuthal resolution therefore improves as source rotational speed increases. Note that in figure 2.6 the highest radial order mode n_0 in both the stationary and rotating source cases is associated with the $m = 0$ azimuthal mode, irrespective of Ω. The maximum radial order therefore does not increase with increasing source rotation frequency. The inequality in equation (2.48) is therefore valid for all rotational speeds, and the radial resolution limit is only weakly dependent on Ω.

Section 2.3.5.2 has shown that attempting to invert for sources on different blades leads to a lower frequency limit below which the inversion cannot be performed. We now propose

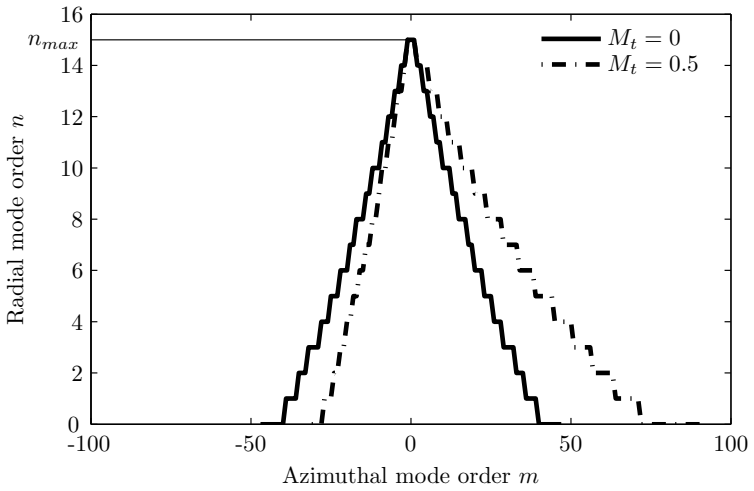

FIGURE 2.6: The mode triangle at $ka = 50$ for stationary (solid line, $M_t = 0$) and rotating (dash-dot line, $M_t = 0.5$) sources. The x-axis denotes the propagating azimuthal mode order m, the y-axis the highest order propagating radial mode associated with each of the azimuthal modes.

a simplifying assumption that not only substantially reduces the number of sources to be inverted but also circumvents the resolution problem identified in section 2.3.5.2.

2.4 Simplifying assumption for the blade surface pressure cross-spectrum

A general expression for the sound field produced by rotating sources in a duct has been derived in equation (2.19). For the case of an aeroengine fan some further simplifying assumptions can be made in order to reduce considerably the number of sources to be inverted.

We first assume that the acoustic sources are concentrated along the trailing edge of each individual rotor blade and that the sources on different blades are uncorrelated. The source spatial cross spectrum of equation (2.20) may therefore be written as

$$S_{ff}(\tilde{\mathbf{y}}, \tilde{\mathbf{y}}', \omega) = S_{ff}(r_s, r'_s, \tilde{\theta}_{s_0}, \omega)\delta(\theta_{s_j} - \theta'_{s_j})\delta(\theta_{s_j} - 2\pi j/B) \qquad (z_s = z'_s) \qquad (2.49)$$

where δ is the Dirac delta function, B is the number of blades and $\theta_{s_j} = 2\pi j/B$ specifies the angular position of the j^{th} trailing edge (where $j = 0, \cdots, B-1$).

Noting that $d\tilde{S}(\tilde{\mathbf{y}}) = r_s dr_s d\tilde{\theta}$, and assuming that the pressure measurements are made at the duct wall $r = a$, equation (2.33), for $S_{p_\Omega p_\Omega}$ for B *identical*, uncorrelated blades

reduces to,

$$S_{p\Omega p\Omega}(\mathbf{x},\mathbf{x}',\omega) = B\int_{r_s}\int_{r'_s}\sum_{m=-m_0}^{m_0}\sum_{m'=-m_0}^{m_0} S_{ff}(r_s,r'_s,\tilde{\theta}_{s_0},\omega)\times$$
$$\times\, g_m(r_s,\tilde{\theta}_{s_0},z,a,\omega+m\Omega)g^*_m(r'_s,\tilde{\theta}_{s_0},z',a,\omega+m'\Omega)e^{\mathrm{i}m\theta-\mathrm{i}m'\theta'}r_s r'_s dr_s dr'_s \quad (2.50)$$

where $\tilde{\theta}_{s_0}$ is the circumferential position of the zeroth blade, $j=0$ (chosen arbitrarily).

We now investigate the accuracy of the inversion procedure by applying it to "measurements" of $\mathbf{S}_{p\Omega p\Omega}$ predicted using a model for S_{ff} in equation (2.50). The rotor blade is modelled as a smooth, flat plate with zero pressure gradient. For simplicity scattering of the hydrodynamic pressure field by the trailing edge is ignored in the model for S_{ff} and the surface pressure fluctuations are assumed to be concentrated at the blade trailing edge. We use the simple model given by Blake [51] to represent the spatial correlation function, S_{ff}, of the pressure fluctuations beneath a turbulent boundary layer on a flat plate, which has the form

$$S_{ff}(r_s,r'_s,\omega) = \Phi_{ff}(r_s,\omega)e^{-\gamma\frac{\omega\Delta r_s}{U_c}} \quad (2.51)$$

where Φ_{ff} is the frequency pressure spectrum of the turbulence boundary layer, and γ is an empirical constant determined from experiment. Further details of the model are given in appendix B. Equation (2.51) may be used to define the boundary layer correlation length, L_c, as the span-wise separation distance $\Delta r_s = |r_s - r_{s'}|$ at which S_{ff} attains half its maximum value,

$$L_c = \frac{ln(0.5)U_c}{-\gamma\omega} \quad (2.52)$$

For practical purposes, the source model of equation (2.51) must be discretized for numerical evaluation of equation (2.50). The number of sources, and hence their separation distance along the blade span, required in the calculation of S_{ff} from equation (2.51) is determined by examining the convergence of $S_{p\Omega p\Omega}$ predicted as a function of the number of uncorrelated sources.

Figure 2.7 is a plot of the magnitude and phase of the cross-spectrum $S_{p\Omega p\Omega}$ as a function of source separation distance for various rotational speeds M_t. The "measured" pressure cross-spectrum is observed to converge as the source separation distance tends to a turbulence correlation length L_c. In order to obtain a converged model for S_{ff} in equation (2.50) therefore, discrete sources used to model the boundary layer pressure distribution of equation (2.51), must be separated by at least one correlation length at the frequency of interest.

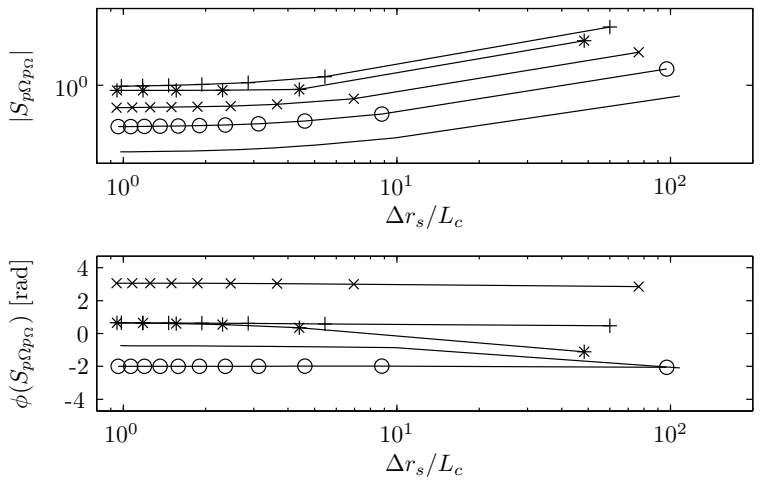

FIGURE 2.7: Convergence of the magnitude (top) and phase (bottom) of $S_{p_\Omega p_\Omega}$ as a function of source separation distance as measured by a pair of microphones situated at the duct wall with an angular separation of 10°. Convergence at varying source rotational speeds is plotted ($M_t = 0$ (solid line), $M_t = 0.2$ (line with circles), $M_t = 0.4$ (line with crosses), $M_t = 0.6$ (line with pluses), $M_t = 0.8$ (line with stars))

Recall from section 2.3.5.3 that for measurements made outside the near field of the rotor, sources can only be resolved with a separation distance greater than approximately $\lambda/2$, where $\lambda = 2\pi c/\omega$ is the acoustic wavelength. The correlation length, L_c, may be compared with this resolution limit by noting that $U_c \approx 0.7\sqrt{(\Omega r)^2 + (Mc)^2}$ and $\gamma = 0.7$ in equation (2.52) to give,

$$\frac{L_c}{\frac{1}{2}\lambda} \approx \frac{M_t}{10} \tag{2.53}$$

The source separation distance required to give a converged value of S_{ff} is therefore significantly less, by an order of magnitude, than the separation distance, $\lambda/2$, that can be resolved using measurements made outside of the near field of the rotor. Equation (2.53) implies that for these measurements the inversion must assume fewer sources, by at least a factor of ten, than the effective number of uncorrelated sources present on the rotor blades. The performance of the inversion technique for this situation will now be investigated.

2.4.1 Application of the inverse technique to the "single-blade" model

Equation (2.50) gives the pressure cross spectra at a particular microphone position due to a fan with B identical blades. The discretized version of this equation, following the procedure presented in section 2.3.1, is

$$\mathbf{S}_{p_\Omega p_\Omega} = B\, \mathbf{G}_\Omega\, \mathbf{S_{ff}}\, \mathbf{G}_\Omega^H \tag{2.54}$$

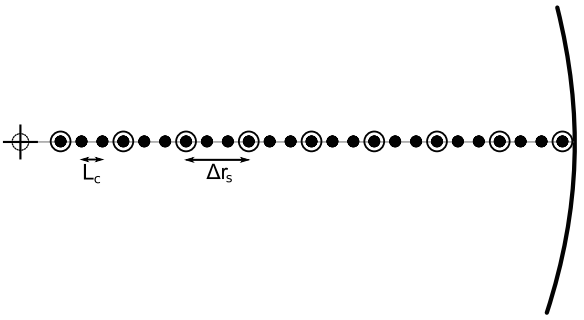

FIGURE 2.8: A schematic of the geometry of the inversion technique for aerodynamic sources. The uncorrelated sources, representing the aerodynamic trailing edge noise in the forward problem, are shown as small circles separated by a turbulence correlation length L_c. The assumed sources, used in the inverse problem, with a separation distance Δr_s are denoted by larger circles.

The determination of $\mathbf{S}_{\hat{f}\hat{f}}$ from measurements of $\mathbf{S}_{p_\Omega p_\Omega}$ follows from equation (2.54) as

$$\mathbf{S}_{\hat{f}\hat{f}} = \frac{1}{B}\mathbf{G}_\Omega^+ \mathbf{S}_{p_\Omega p_\Omega} \mathbf{G}_\Omega^{+H} \tag{2.55}$$

A schematic diagram of the source geometry used in this simulation is shown in figure 2.8. The uncorrelated sources, representing the aerodynamic trailing edge noise in the forward problem, are shown as small circles separated by a turbulence correlation length L_c. The assumed sources, used in the inverse problem, with a separation distance Δr_s, are denoted by the larger circles.

The accuracy of the inversion is computed from the normalised error function defined by

$$J_{ff} = \frac{\|\mathbf{S}_{ff} - \mathbf{S}_{\hat{f}\hat{f}}\|}{\|\mathbf{S}_{ff}\|} \tag{2.56}$$

where $\mathbf{S}_{ff}$ is the source strength cross-spectrum of the exact aerodynamic sources at the location of the assumed sources.

In order to improve upon the resolution limits identified in section 2.3.5 obtained for measurements made away from the rotor near field requires measurements to be made in the acoustic near field. For this region the sound field comprises high wavenumber components. This necessitates the inclusion of cutoff modes in the calculation of $\mathbf{G}_\Omega$ and in the measurement of p_Ω.

The inversion is performed at $ka = 15$ and $M_t = 0.5$ for various axial measurement positions between $\delta z = |z - z_s| = 0.05\lambda$ and $\delta z = 10\lambda$. The turbulence correlation length of the aeroacoustic sources, from equation (2.52) is $0.0148m$. For a duct with a 1 metre radius, therefore, $a/L_c \approx 68$ sources are used in the forward problem to calculate the cross-spectra $S_{p_\Omega p_\Omega}$ at the measurement positions. Note that the number of cutoff modes included in the calculation is chosen to give a converged solution of p_Ω and $\mathbf{G}_\Omega$.

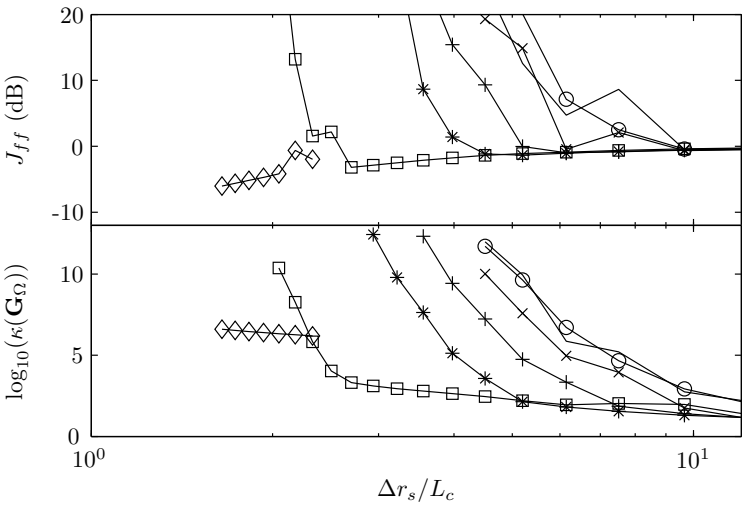

FIGURE 2.9: A plot of the inversion accuracy J_{ff} and the conditioning of the transfer matrix $\kappa(\mathbf{G}_\Omega)$ as a function of the distance between assumed sources ($\Delta r_s/L_c$). The simulation is carried out for various source-microphone separation distances $\delta z/\lambda = 10$ (solid line), $\delta z/\lambda = 1$ (with circles), $\delta z/\lambda = 0.5$ (with crosses), $\delta z/\lambda = 0.3$ (with pluses), $\delta z/\lambda = 0.2$ (with stars), $\delta z/\lambda = 0.1$ (with squares), $\delta z/\lambda = 0.05$ (with diamonds). Measurement in the near-field allows more sources to be assumed, and therefore improves the reconstruction accuracy, at the expense of conditioning.

The pressure measurements used in this inversion could be obtained in practice by a radial "rake" with the same number of sensors as assumed sources, equally spaced along a single radius from the centre of the duct to the duct wall. The pressure cross spectrum $\mathbf{S}_{p_\Omega p_\Omega}$ is calculated at the microphone positions using equation (2.54). The inversion is performed using equation (2.55) with varying numbers of assumed sources equally spaced along a radius (as illustrated in figure 2.8). Figure 2.9 is a plot of the inversion accuracy J_{ff} (equation (2.56)) and the conditioning of the transfer matrix $\kappa(\mathbf{G}_\Omega)$, as a function of the separation distance, Δr_s, between assumed sources for varying source-microphone axial separation distances, δz.

Figure 2.9 indicates that good inversion accuracy and acceptable conditioning values are only possible simultaneously for microphones positioned closer than approximately $\lambda/3$ from the source plane. Figure 2.10 shows some illustrative results for the inverted source strength magnitudes along the blade trailing edge (crosses, the diagonal elements of the $\mathbf{S}_{\hat{f}\hat{f}}$ matrix). Also shown are the exact source strengths used in the converged model for $\mathbf{S}_{ff}$ (circles).

Figure 2.10 shows that, with approximately one assumed source per two correlation lengths (figure 2.10(a)), with microphones positioned 0.05λ from the source plane, it is possible to achieve a reconstruction of the source strength distribution that agrees well with the exact source strength distribution. However, $\kappa(\mathbf{G}_\Omega)$ is very high ($> 10^6$) in this example. Errors in the reconstructed source strengths are most apparent at the tip of the blade, $r_s = a$. Figures 2.10(b) and 2.10(d) suggest that moving the microphone array further from the rotor requires fewer sources to be assumed in order to ensure good

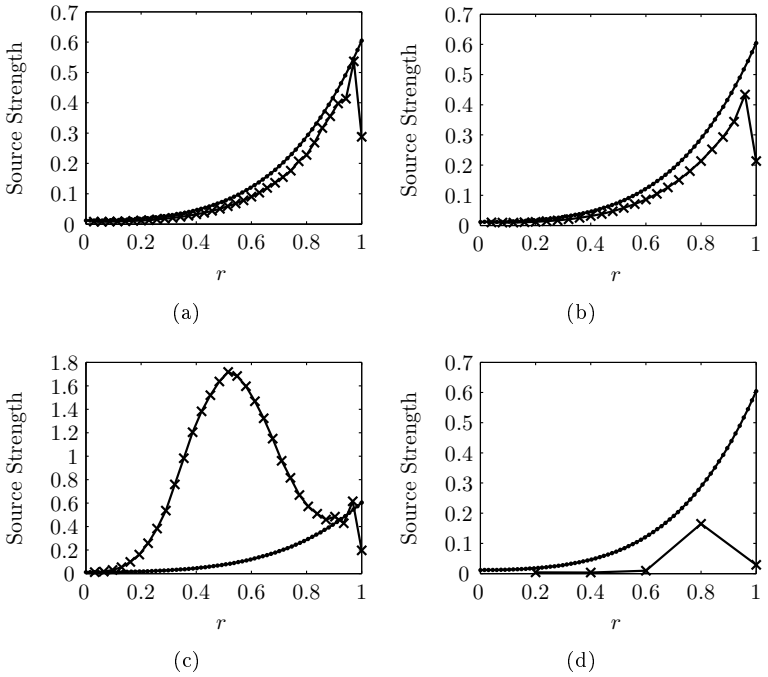

FIGURE 2.10: Reconstruction of radial source strengths at $ka = 15$ with near-field effects. Plotted are the true source strengths (line with circles) and the reconstructed source strengths (line with crosses) as a function of radial distance. The source-receiver separation distance, conditioning of the transfer matrix and radial spacing between assumed sources in each case are as follows (a) $\delta z = 0.05\lambda$, $\kappa(\mathbf{G}_\Omega) = 2.48 \times 10^6$, $\Delta r_s/L_c = 1.93$. (b) $\delta z = 0.1\lambda$, $\kappa(\mathbf{G}_\Omega) = 2068$, $\Delta r_s/L_c = 2.70$. (c) $\delta z = 0.1\lambda$, $\kappa(\mathbf{G}_\Omega) = 1.85 \times 10^8$, $\Delta r_s/L_c = 2.18$. (d) $\delta z = 0.1\lambda$, $\kappa(\mathbf{G}_\Omega) = 12.8$, $\Delta r_s/L_c = 13.5$.

conditioning. However, the reconstruction accuracy deteriorates as a result. Assuming the same number of sources at $\delta z = 0.1\lambda$ as at $\delta z = 0.05\lambda$ (figure 2.10(c)) results in poor conditioning, and hence poor agreement, between reconstructed and exact source strengths.

In order to improve the reconstruction accuracy further, it would be necessary to move the microphones even closer to the source plane. This might be difficult to achieve in practice, and would require an even greater number of sensors to perform the modal decomposition for the determination of p_Ω. Steps would also have to be taken to minimise contamination of the measurements by flow noise. At $ka = 15$ and $\delta z = 0.1\lambda$, the maximum azimuthal mode order, m^+, included in the calculation of $\mathbf{G}_\Omega$ is 100. Practical application of the inversion technique at this frequency would therefore require the determination of the amplitudes of all modes up to this order.

Positioning the microphones close to the rotor would in practice increase the significance of cascade effects (multiple reflections of the sound radiated from the trailing-edges between adjacent blades). In principle, these effects could be taken into account in the formulation of the measured or predicted Green's functions. An indication of the significance of cascade effects on trailing edge noise is provided by the work of Glegg [52] who has shown that, to a good approximation, radiation from the cascade is related to

that from an isolated airfoil by a simple frequency dependent multiplicative factor, that varies between 0 and 2.

The results in this chapter suggest that there is a balance to be struck between the reconstruction accuracy, J_{ff}, and the conditioning $\kappa(\mathbf{G}_\Omega)$. Based on the data presented in this chapter, a suitable compromise is to make measurements 0.1λ from the source plane, assuming approximately one source for every 3 turbulence correlation lengths. This allows source strengths to be estimated to around $1dB$ accuracy. The condition number of approximately $\kappa(\mathbf{G}_\Omega) \approx 2000$ has been shown [30] to be low enough to allow inversion to be performed in realistic experimental conditions, especially if the conditioning is improved further by the application of matrix regularisation techniques. It should be noted, however that the improvement of conditioning be regularisation is usually at the expense of reduced inversion accuracy.

2.5 Conclusion

An inversion technique suitable for the determination of rotating, broadband sources in a duct has been presented. This work is an extension of the work of Kim and Nelson [30] for the inversion of stationary ducted monopoles.

The principle findings presented in this chapter may be summarised as follows:

- The rotation of sources in a duct causes a coupling between source and propagation terms. Existing inversion techniques therefore cannot be used for the determination of aerodynamic sources on rotor blades.

- A measurement technique has been developed to deduce the pressure spectrum that is precisely equal to that measured by microphones rotating around the duct axis at the same rotational speed as the fan.

- Based on this new measurement technique, and the introduction of a modified Green's function, which includes the effects of source rotation, a new inversion technique has been devised that allows the determination of the strength of rotating, broadband sources in their rotating reference frame.

- The resolution limits of the new inversion technique, for measurements made outside the near field of the rotor, have been shown to be significantly larger than the effective separation distance of uncorrelated sources located on the fan blade trailing edge. To improve upon the resolution limits therefore, measurements must

be made in the near field of the rotor, requiring the use of a much larger number of sensors to decompose the azimuthal modes.

- Simulations have demonstrated that for a 26-bladed fan, rotating at $M_t = 0.5$, the aerodynamic source strengths can be estimated with acceptable robustness and approximately 1dB accuracy, when measurements are made 0.1 acoustic wavelengths from the rotor.

Chapter 3

A Rotating Beamformer Technique for Locating and Quantifying Aeroengine Noise Sources

3.1 Introduction

The previous chapter presented an inversion technique for determining the strength of acoustic sources in the rotating reference frame. The principal disadvantage of the technique was the ill-conditioning of the matrix to be inverted when a large number of sources were assumed to be present. In this chapter we discuss a method, based on a focused beamformer technique, to overcome these limitations. The principle application of the in-duct beamformer presented in this chapter is to quantify how much of the radiated broadband noise from the fan can be attributed to the rotor alone and how much is due to the stator.

The basis of the technique is a conventional beamformer whose point of focus rotates around the duct axis at the shaft rotational frequency. The rotating beamformer has the desirable property that noise due to stationary sources is partially rejected, since their contribution to the beamformer becomes "smeared". This property is exploited to quantify the relative contributions of the rotor-based and stator-based broadband sources.

The development of a beamformer to identify free-field sources in the rotating reference frame was first undertaken by Sijtsma *et al.* [38, 39], in order to locate sources on open rotors in wind-tunnels, and on wind-turbines. Their work, based in the time-domain, introduced time-dependent delays between the individual microphones to allow the beamformer beam to rotate at the same rotational speed as the rotor. Recent work by Sijtsma [40] and the present author [41] has extended this technique to the quantification

of ducted sources. The advantages and disadvantages of the technique proposed by Sijtsma and the one in this thesis are discussed in section 3.3.

The proposed technique relies on the estimation or prediction of an in-duct frequency-domain Green's function between a stationary receiver point and a rotating point dipole source, as outlined in chapter 2. While this would no doubt be technically challenging in practice, recent work on this subject provides some encouragement that this is achievable. Holland [32] has demonstrated that beamforming can be performed to locate sources using measured Green's functions in a reverberant environment. For in-duct applications the work of Kim and Nelson [30] demonstrated the feasibility of using modelled Green functions to experimentally determine the location of simple sources by inverse methods.

3.2 Theory

The development of a rotating-focus beamformer begins with measurement of the acoustic pressure, p_Ω, deduced from acoustic pressure measurements made at the wall of a circular duct as described in chapter 2. It was shown to be identical to that measured by microphones rotating around the duct axis with angular speed Ω. This modified pressure is now used as the input to a conventional frequency-domain focused beamformer formulation [53] of the form

$$b(\tilde{\mathbf{y}}_b, \Omega, \omega) = \mathbf{w}^H(\tilde{\mathbf{y}}_b, \mathbf{x}, \Omega, \omega)\mathbf{p}_\Omega(\mathbf{x}, \omega) \tag{3.1}$$

where $\mathbf{p}_\Omega$ is a vector of modified pressures measured at the microphone locations $\mathbf{x} = [\mathbf{x}_1, \mathbf{x}_2, \ldots, \mathbf{x}_N]^T$, $\tilde{\mathbf{y}}_b$ denotes the focus point of the beamformer in the rotating reference frame and $\mathbf{w}$ is a vector of complex weighting coefficients. The fundamental assumption made here is that since $\mathbf{p}_\Omega$ is the pressure measured by a microphone rotating around the duct axis, the array beam pattern defined from equation (3.1) also rotates about the axis and is therefore stationary in the rotating reference frame.

To obtain an expression for $\mathbf{w}$, we first assume that by focusing the beam at a single point the noise from other points can be ignored. The vector of measured pressures in the rotating reference frame, $\mathbf{p}_\Omega$, due to a single rotating point force of magnitude $f(\tilde{\mathbf{y}}, \omega)$ at location $\tilde{\mathbf{y}}$ can be written as

$$\mathbf{p}_\Omega(\mathbf{x}, \omega) = f(\tilde{\mathbf{y}}, \omega)\mathbf{g}_\Omega(\tilde{\mathbf{y}}, \mathbf{x}, \Omega, \omega) \tag{3.2}$$

where $\mathbf{g}_\Omega(\tilde{\mathbf{y}}, \mathbf{x}, \Omega)$ is a vector of transfer impedances,

$$\mathbf{g}_\Omega^T(\tilde{\mathbf{y}}, \mathbf{x}, \Omega) = [G_\Omega(\tilde{\mathbf{y}}, \mathbf{x}_1), G_\Omega(\tilde{\mathbf{y}}, \mathbf{x}_2), \ldots, G_\Omega(\tilde{\mathbf{y}}, \mathbf{x}_N)] \tag{3.3}$$

where $\mathbf{x}_i$ is the location of the i^{th} microphone, and G_Ω is the rotating-source Green's function defined in equation (2.35). The ω-dependence has been dropped for brevity.

The complex weighting coefficients $\mathbf{w}$ are chosen such that the beamformer output is as close as possible to the true source strength when $\tilde{\mathbf{y}} = \tilde{\mathbf{y}}_b$. Thus, we require $\mathbf{w}$ that minimises the cost function

$$J = \frac{\pi}{T} E\{|b(\tilde{\mathbf{y}}, \Omega) - f(\tilde{\mathbf{y}})|^2\} \tag{3.4}$$

Substitution of equation (3.2) into equation (3.4) gives

$$J = \frac{\pi}{T} E\{(\mathbf{w}^H \mathbf{p}_\Omega(\mathbf{x}) - f(\tilde{\mathbf{y}}))(\mathbf{w}^H \mathbf{p}_\Omega(\mathbf{x}) - f(\tilde{\mathbf{y}}))^*\} \tag{3.5}$$

Equation (3.5) can be written in the quadratic form

$$J = \mathbf{w}^H \mathbf{S}_{p_\Omega p_\Omega} \mathbf{w} - \mathbf{w}^H \mathbf{s}_{p_\Omega f} - \mathbf{s}_{p_\Omega f}^H \mathbf{w} + S_{ff} \tag{3.6}$$

where $\mathbf{S}_{p_\Omega p_\Omega}$ is a matrix formed from the cross-spectra of every microphone with every other microphone, $\mathbf{s}_{p_\Omega f}$ is the vector of cross spectra between source and sensors, and S_{ff} is the power spectrum of the source defined respectively as

$$\mathbf{S}_{p_\Omega p_\Omega} = \frac{\pi}{T} E\{\mathbf{p}_\Omega(\mathbf{x}) \mathbf{p}_\Omega^H(\mathbf{x})\}, \quad \mathbf{s}_{p_\Omega f} = \frac{\pi}{T} E\{\mathbf{p}_\Omega(\mathbf{x}) f^*(\tilde{\mathbf{y}})\}, \quad S_{ff} = \frac{\pi}{T} E\{|f(\tilde{\mathbf{y}})|^2\} \tag{3.7}$$

Given that $\mathbf{p}_\Omega(\mathbf{x}) = f(\tilde{\mathbf{y}}) \mathbf{g}_\Omega(\tilde{\mathbf{y}}, \mathbf{x}, \Omega)$ from equation (3.2), the optimum weighting vector that minimises equation (3.6) under the assumption that no additional noise is present at the sensors is given ([53]) by,

$$\mathbf{w}(\tilde{\mathbf{y}}, \mathbf{x}, \Omega) = (\mathbf{g}_\Omega^H(\tilde{\mathbf{y}}, \mathbf{x}, \Omega) \mathbf{g}_\Omega(\tilde{\mathbf{y}}, \mathbf{x}, \Omega))^{-1} \mathbf{g}_\Omega(\tilde{\mathbf{y}}, \mathbf{x}, \Omega) \tag{3.8}$$

Note that the determination of source strength using the focused beamforming method does not rely on the inversion of a matrix as in the inversion method of chapter 2. Beamforming avoids the issues associated with the conditioning of the inverse problem at the expense of uncertainty in determining source location and strength, as will be demonstrated later in this chapter.

The beamformer output spectral density, $S_{bb}(\tilde{\mathbf{y}}, \Omega)$, is given

$$S_{bb}(\tilde{\mathbf{y}}, \Omega) = E[\frac{\pi}{T} |b(\tilde{\mathbf{y}}, \Omega)|^2] = \mathbf{w}^H(\tilde{\mathbf{y}}, \mathbf{x}, \Omega) \mathbf{S}_{p_\Omega p_\Omega} \mathbf{w}(\tilde{\mathbf{y}}, \mathbf{x}, \Omega) \tag{3.9}$$

In an engine duct in which fan broadband noise sources are predominantly situated either on the rotor and stator, $\mathbf{S}_{p_\Omega p_\Omega}$ can be written as

$$\mathbf{S}_{p_\Omega p_\Omega} = \mathbf{S}_{p_\Omega p_\Omega}^{\mathrm{R}} + \mathbf{S}_{p_\Omega p_\Omega}^{\mathrm{S}} \tag{3.10}$$

where $\mathbf{S}^{\mathrm{R}}_{p\Omega p\Omega}$ and $\mathbf{S}^{\mathrm{S}}_{p\Omega p\Omega}$ are the contributions to the pressure cross-spectral matrix from the rotor and stator sources respectively, and are assumed to be mutually incoherent. Substitution of equation (3.10) in equation (3.9) gives

$$S_{bb}(\tilde{\mathbf{y}},\Omega) = S^{\mathrm{R}}_{bb}(\tilde{\mathbf{y}},\Omega) + S^{\mathrm{S}}_{bb}(\tilde{\mathbf{y}},\Omega) \tag{3.11}$$

thus, the contributions to the mean-square beamformer output from the rotor and stator are additive.

3.3 Review of the Rotating Beamformer due to Sijtsma

To the author's knowledge the only other study on the use of phased array beamforming techniques to locate rotating ducted broadband sources was recently presented by Sijtsma [40]. This section presents a comparison of the technique proposed in this thesis and that proposed by Sijtsma. The derivation presented here follows an earlier paper by Sijtsma et al. [38].

The starting pointing of the rotating beamformer algorithm proposed by Sijtmsa et al. is equation (3.12), which expresses the time-dependent acoustic pressure at the i^{th} microphone $p_i(t)$ in terms of the time-dependent monopole source strength, $\sigma(\tau)$ whose position varies with time varies according to $\mathbf{y}(\tau)$ and a time-dependent "transfer function" $T(\mathbf{x}_i,\mathbf{y}(\tau),t,\tau)$,

$$p_i(t) = T(\mathbf{x}_i,\mathbf{y}(\tau),t,\tau)\sigma(\tau) + n(t) \tag{3.12}$$

where $n(t)$ is the pressure contribution due to noise and from the other sources. An important aspect of equation (3.12) is that the source strength is expressed in terms of emision time τ, which has the advantage that equation (3.12) is separable such that the source term $\sigma(\tau)$ and the propagation term T are decoupled. This procedure is exactly analogous to that undertaken in the frequency domain in section 2.2 (*cf* equation (2.17)) in which appropriate frequency shifts were introduced into the source term to allow the source term to be decoupled from the propagation term. Following the analysis due to, for example, Dowling and Ffowcs Williams [54] of the sound due to sources in motion, T is of the form

$$T(\mathbf{x}_i,\mathbf{y}(\tau),t,\tau) = \frac{1}{4\pi\{t-\tau+Q(\mathbf{x}_i,\mathbf{y}(\tau),t,\tau)\}} \tag{3.13}$$

where

$$Q(\mathbf{x}_i,\mathbf{y}(\tau),t,\tau) = \left[-\mathbf{y}'(\tau)+M\mathbf{n}_z\right]\cdot\left[\mathbf{x}_i-\mathbf{y}(\tau)-M(t-\tau)\mathbf{n}_z\right] \tag{3.14}$$

and $\mathbf{n}_z$ is the unit vector in the flow direction and the prime denotes differentiation with respect to the argument. Observer time t and emission time τ are related by

$$t_i = \tau - \frac{M\left(\mathbf{x}_i-\mathbf{y}(\tau)\right)\cdot\mathbf{n}_z}{1-M^2} + \frac{\sqrt{M^2\{(\mathbf{x}_i-\mathbf{y}(\tau))\cdot\mathbf{n}_z\}^2+(1-M^2)|\mathbf{x}_i-\mathbf{y}(\tau)|^2}}{1-M^2} \tag{3.15}$$

The estimate for source strength $\hat{\sigma}(\tau)$ at a particular "look" direction $\mathbf{y}$ is obtained directly from equation (3.12) by correcting the measured pressure signal at each microphone for its propagation between source and receiver postion (that is, by dividing by T) and summing the result

$$\hat{\sigma}(\tau) = \frac{1}{N} \sum_{i=1}^{N} \frac{p_i(t_i)}{T(\mathbf{x}_i, \mathbf{y}(\tau), t_i, \tau)} \tag{3.16}$$

Thus since equation (3.16) corrects for both amplitude and phase it permits focussing in range as well as angle.

The implementation by Sijtsma of the technique decribed in [40] for the determination of source strengths in a duct uses a free-field transfer function. This assumption is justified by the use of acoustic lining which minimises the reflections from the duct wall. Due to the non-axisymmetric duct geometry Sijtsma also suggests the use of an analytical duct-mode based Green's function for the beamformer, in order to incorporate the effects of the duct on the sound field. In this chapter we investigate the use of such an analytical Green's function. Also the use of the modified pressure formulation in chapter 2 allows all processing to take place in the frequency domain.

In summary therefore, the key differences between the technique proposed in this chapter, and that used by Sijtsma are,

- Our formulation of a measured pressure in the rotating reference frame allows both stationary and rotating focus to be achieved in the frequency domain. This makes the modelling of the Green's function more practical
- Our formulation permits the effect of the duct to be taken into account; this means that acoustic lining of the duct is not necessary.

3.4 Use of the rotating-focus beamformer to separate rotating and stationary sources

The principle application of the in-duct beamformer presented in this chapter is to resolve the broadband noise sources into their rotor and stator based components. For locating sources on the stator, a stationary beam, achieved by setting $\Omega = 0$ in equation (3.9), is used. For locating sources on the rotor, a rotating beam, rotating at the same speed as the rotor, is focused on the rotating sources. The ability of the rotating-focus beamformer to discriminate rotor sources and stator sources is now investigated from the results of computer simulations.

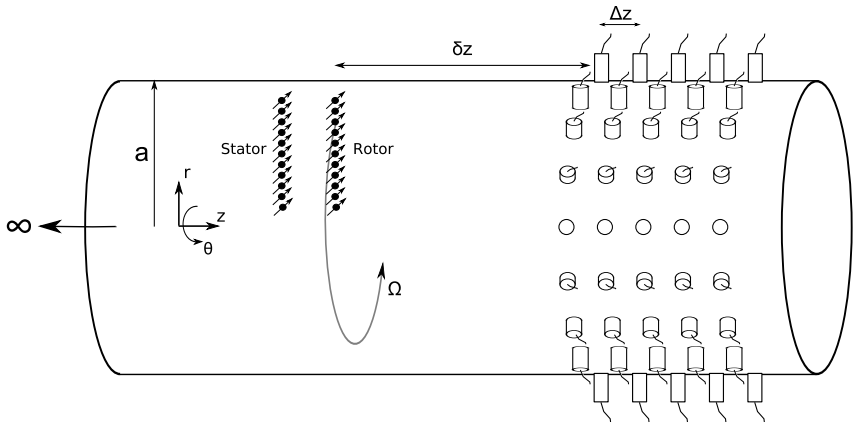

FIGURE 3.1: A line of dipole sources rotating at angular speed Ω represent the rotor. The stator is modelled by a stationary line of dipole sources. The sources are located at $\mathbf{y}_s$. The sound field is detected by an array of microphones located at $\mathbf{x}$, with the first ring δz from the stator. The array consists of N_z rings, and has a total length L_z. The rotating-focus beamformer beam is steered to focus at locations $\mathbf{y}$.

In the following simulations, for simplicity, the rotor and stator are each represented by a single radial line of discrete dipole sources (figure 3.1), separated by L_c, the turbulence correlation length given by equation (2.52), such that the sources can be considered uncorrelated. For simplicity, the source strength distribution along the blade span is assumed to follow a simple power law, $f(r_s) \propto r_s^n$ where $n = 0$. Higher powers were also investigated but had little effect on the results. The rotor sources are located at $z = 0$, and the stator sources at $z = -2\lambda$. The rotor sources rotate around the duct axis at $M_t = 0.5$.

The microphone array consists of 3 rings of 50 microphones, with adjacent rings separated axially by $\Delta z = \lambda/2$ with the first ring located at $\delta z = 10\lambda$ from the rotor plane. A uniform flow of $M = 0.2$ is assumed in the simulation. Source near field effects are modelled by including evanescent modes with amplitudes of up to 30dB lower than the maximum propagating mode amplitude at the location of the first microphone ring. Note that blockage of sound due to the transmission through the rotor and stator is not included in the simulation.

We first investigate the variation of beamformer output as the point of focus of the beam is made to vary axially along the duct using first a stationary beam, and then a rotating beam. Figure 3.2a is a plot of the beamformer output as the axial focus point varies from -4λ to 2λ, with the azimuthal and radial positions of the focus point held constant at 0° and $0.8a$ respectively.

The beamformer output is calculated for the three cases: i) rotor sources present only, ii) stator sources present only and iii) with both rotor and stator sources present simultaneously. Note that the beamformer output with both rotor and stator sources present is the sum of the beamformer outputs of the rotor and stator alone cases (from equation

(3.11)). The results of the simulation repeated with a beam rotating at the same angular speed as the rotor, $M_t = 0.5$ is shown in figure 3.2b.

With a stationary beam, figure 3.2a, the combined beamformer output (solid black line) has a maximum output at the location of the stator sources, $z = -2\lambda$. Examining the contribution to the beamformer output from the stator and rotor sources alone we see that the stator sources (dotted line) are the major contributor. The rotor sources (dashed line), located at $z = 0\lambda$ do not contribute significantly to the combined beamformer output. Their individual contribution is approximately 15dB lower than the stator sources at $z = -2\lambda$, and 7dB at $z = 0\lambda$.

Figure 3.2b shows the same three predictions obtained from the rotating beam. Here the opposite behaviour to figure 3.2a is observed. The maximum beamformer output is now observed at the location of the rotating sources, $z = 0\lambda$ and is therefore dominated by the contribution due to the rotating sources. Stationary sources are therefore suppressed by the rotating beam and rotating sources are suppressed by the stationary beamformer.

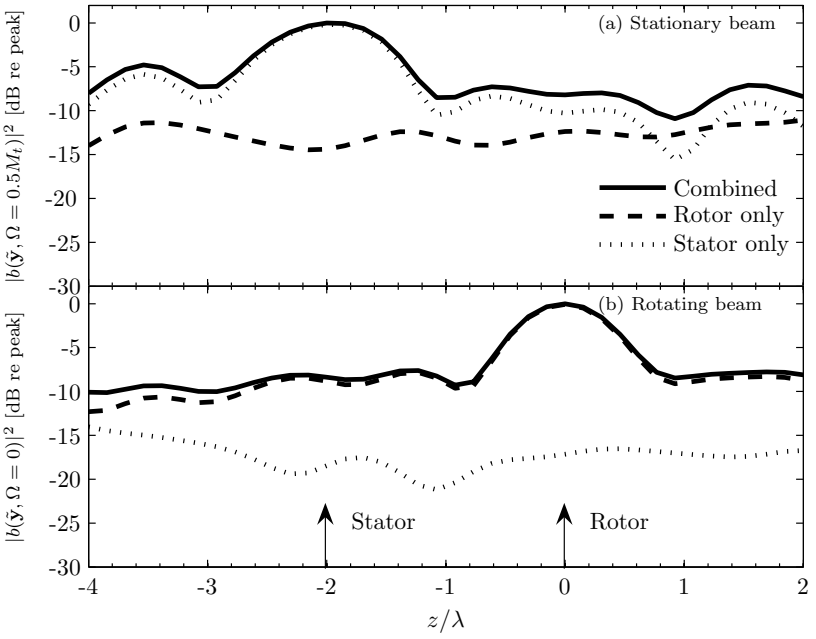

FIGURE 3.2: Beamformer output as a function of axial steering location z using a stationary (a) and a rotating (b) beam. The solid curve is the beamformer output, the dashed curve shows the contribution to the beamformer output from the rotor sources alone, the dotted line from the stator sources alone. Arrows indicate the location of the rotor and stator.

Figure 3.3(a) is a colour-map of the beamformer output for the simulation in figure 3.2 with the focus now steered over the z-r plane corresponding to $-4 \leq z/\lambda \leq 2$, $0 \leq r/a \leq 1$ at $\theta = 0°$. The colour scale is normalised to the peak output. Figure 3.3(b) shows the prediction for a rotating beam. The stator sources are visible when a stationary beam is used, and suppressed in favour of the rotating sources when a rotating beam is used.

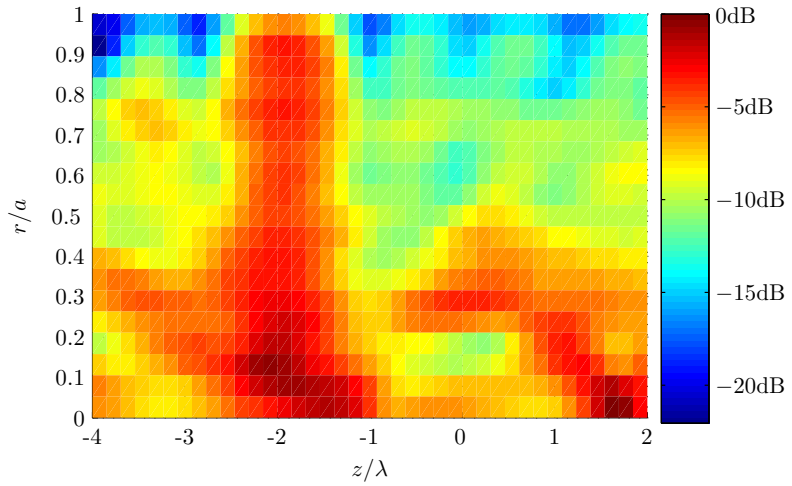

(a)Stationary beam ($M_t = 0$)

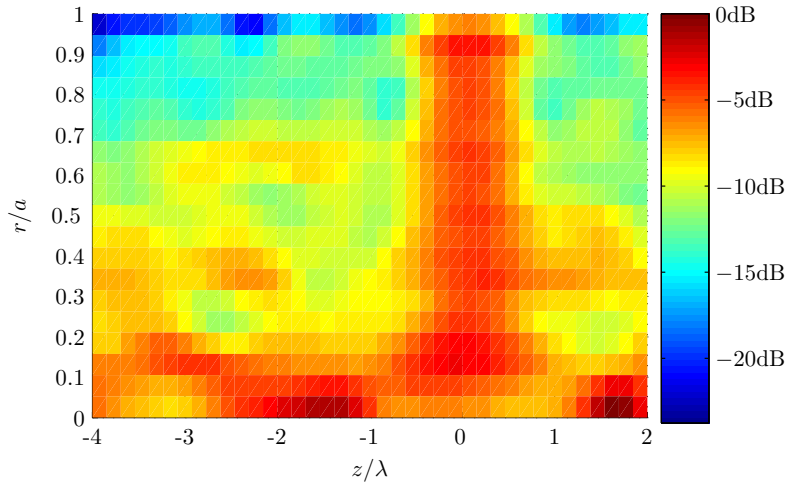

(b)Rotating beam ($M_t = 0.5$)

FIGURE 3.3: Beamformer output as the beamformer focus is moved in the z-r plane for a stationary beam (top) and a beam rotating at the same rate as the rotor (bottom).

In figures 3.2 and 3.3 the location of maximum beamformer output corresponding to the source location is not a sharp peak but is instead distributed over a finite region. This region may be interpreted as the main lobe of the region. The width of the beamformer lobe, taken at the 3dB-down point is approximately 1λ. The width of the mainlobe is a measure of the *beamformer resolution* and depends on a number of factors presented later in the chapter. A beamformer with a large mainlobe has poor resolution and is unable to distinguish sources that are too close together. We will now investigate what happens when the rotor and stator sources are moved close together such that the beamformer main-lobes overlap, and cannot be separated using a conventional stationary beamformer.

Figure 3.4, shows a repeat of the calculation in figure 3.2 but with the rotor and stator sources separated by 0.5λ, i.e. less than the beamwidth. Figure 3.4a is a plot of the stationary beamformer output as a function of axial scanning position with a stationary beam. In this plot the rotor sources are also assumed to be stationary.

In figure 3.4a, the solid line is the beamformer output with the stationary beamformer. Due to the overlap of the main-lobes of the individual beamformer outputs, the two sources are indistinguishable, as is the case with a standard beamformer.

Figure 3.4b is a plot of the beamformer output as a function of axial steering position with the rotor sources rotating at $M_t = 0.5$. The dashed curve is the beamformer output with a rotating beam, the dotted curve with a stationary beam. The rotor sources are clearly distinguishable from the stationary sources when detected with a rotating beam.

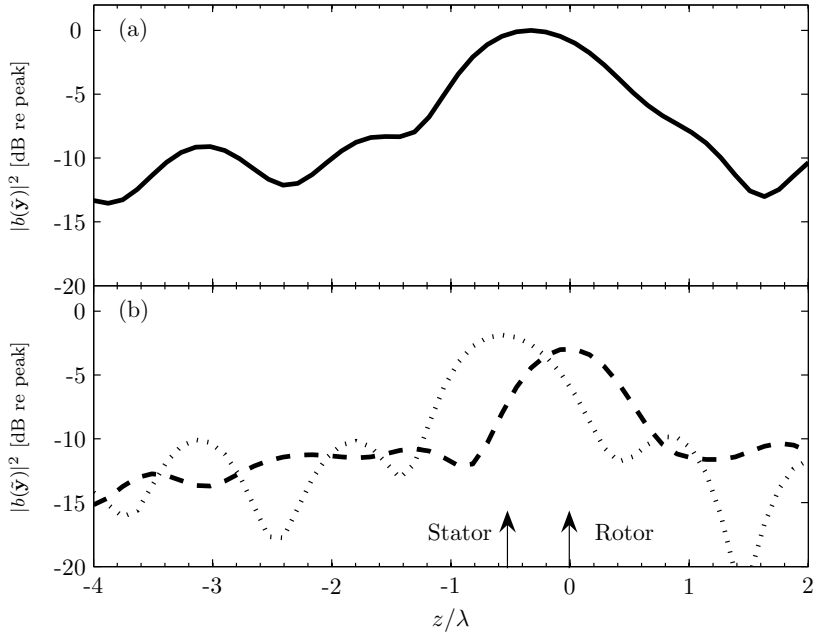

FIGURE 3.4: Beamformer output in the axial direction at $r = 0.8a$. Rotor and stator sources are separated by $\lambda/2$. In (a) the rotor and stator sources are both stationary. In (b) the rotor sources are rotating at $M_t = 0.5$ and the stator sources are stationary. The dotted line is the beamformer output with a stationary beam, the dashed line is with a rotating beam.

In conclusion the rotating-focus beamformer is able to differentiate between rotor and stator based sources by virtue of two properties:

1. A finite mainlobe and sidelobe rejection common to all phased-array beamformers.
2. Additional suppression of stationary sources when detected by a rotating beam and vice-versa, due to the "smearing" effect.

3.4.1 Illustrative beamformer results for the separation of multiple rotor and stator based sources

In section 3.4 the rotor and stator sources were assumed to consist of a single line of point dipole sources. We now consider a larger number of line sources arranged to model multiple fan blades and stator vanes.

Figure 3.5 shows the beamformer output when the rotating beamformer is focused on a simulated fan consisting of 13 blades rotating at $M_t = 0.5$. A stator row consisting of 26 vanes is assumed to be present separated axially from the fan at varying axial distances. Due to the periodicity of the fan face, only an 80° segment of the duct is shown.The frequency is $ka = 20$, and the source separation distance on each blade or vane is $2L_c$, this corresponds to 20 sources per blade on the rotor, and 44 sources per vane on the stator. A larger source separation distance than in section 3.4 was chosen for computational reasons. The total strengths of the rotor and stator sources are equal. The sources on each blade and vane are distributed between $r_s = 0.4a$ and $r_s = a$. There are no sources at $r_s < 0.4a$ in order to simulate the presence of a rotor hub. The microphone array used has 5 rings with 50 microphones in each ring.

Figures 3.5a and 3.5b are the beamformer outputs of the rotating beam and the stationary beam respectively for a rotor-stator separation distance of 0.2λ. Figures 3.5c and 3.5d show the beamformer output for a separation distance of λ, and figures 3.5e and 3.5f for a distance of 5λ. At all separation distances the sources between different individual rotor blades and stator vanes are distinguishable. As the separation distance decreases to less than a beamwidth ($< \lambda$) the rotor and stator sources are still differentiated from one another, particularly close to the tip, however there is noticeably higher beamformer output between the individual rotor blades close to the centre of the duct where the sources are closeer together than the beamwidth. Sources on the same blade (or vane) cannot be resolved for the reasons discussed in section 3.5.

3.5 Beamformer resolution

Beamformer resolution is a measure of how closely the beamformer is able to distinguish sources that are close together. Aeroacoustic sources are considered to be separate if the distance between them is larger than a correlation-length - a distance related to the larger scale turbulent structures in the flow.

The output of a beamformer $b(\mathbf{y})$ typically consists of a mainlobe at the location of the source with a series of sidelobes on either side of the true source location. Two sources that lie inside the beamformer mainlobe will be indistinguishable. The width of the mainlobe therefore determines the beamformer resolution. An ideal beamformer would have zero beamwidth and infinite sidelobe rejection. It is known from array processing theory (summarised for example by Johnson and Dudgeon [45]) that for arrays of finite spatial extent the mainlobe will always have a finite width. This chapter uses the definition of beamwidth as the width of the mainlobe at one half of its peak value (known in the literature as the Full-Width Half-Maximum, or "3dB down") and denoted here by $\Delta\mathbf{y}_{\frac{1}{2}}$.

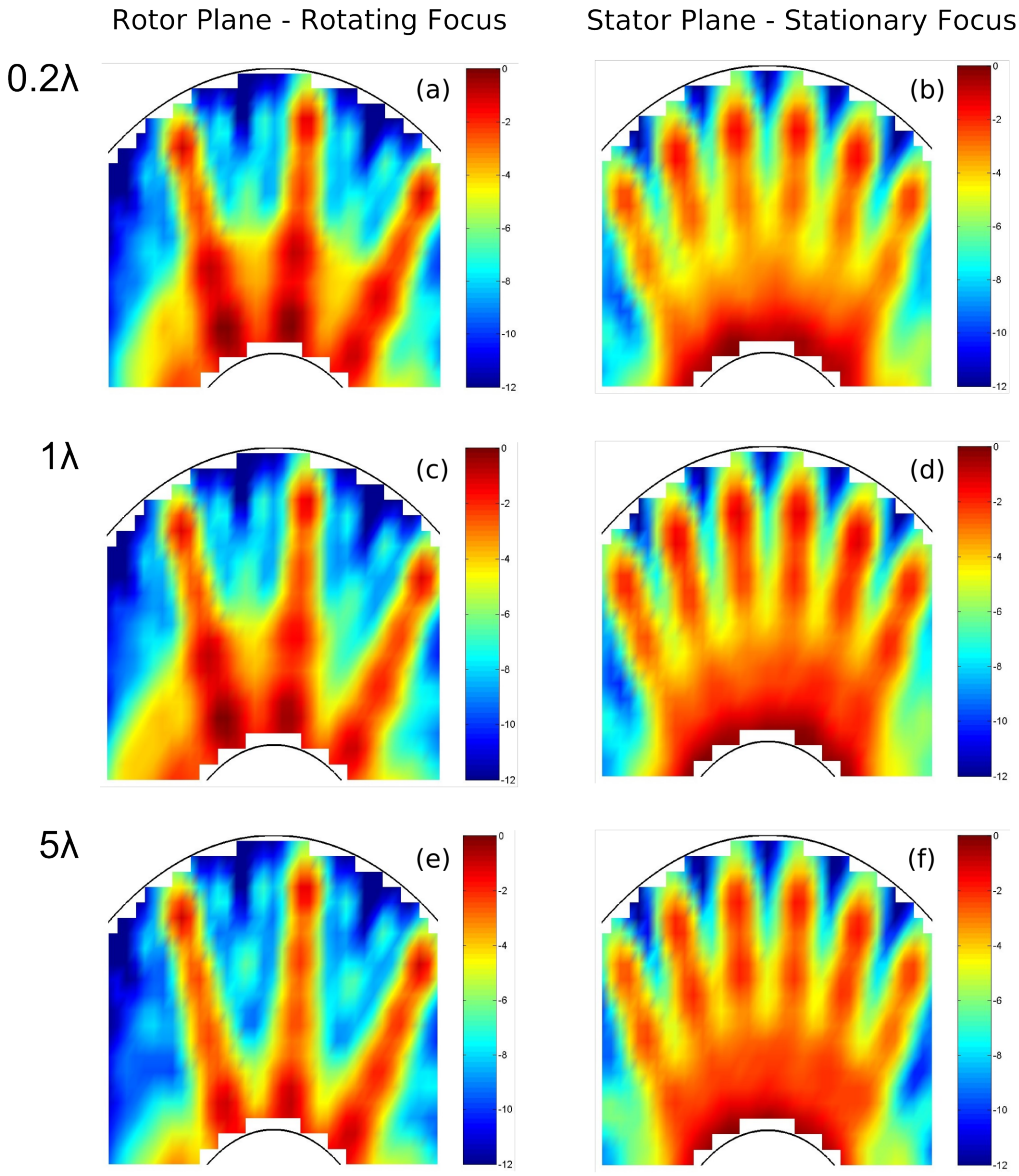

FIGURE 3.5: Identification of rotor and stator sources for a simulated turbofan engine with 13 rotor blades and 26 stator vanes. The frequency is $ka = 20$, and the rotor sources are rotating at $M_t = 0.5$. Figures (a) and (b) are the beamformer outputs in the rotor (rotating-beam) and stator (stationary-beam) planes respectively for a rotor-stator separation distance of 0.2λ, (c) and (d) for a distance of λ and (e) and (f) for 5λ.

In the previous section the rotating-focus beamformer was used to separate rotor and stator noise sources. This is achieved by virtue of two properties. Firstly the "smearing" of source strengths that occurs when a rotating source is detected by a stationary beamformer and vice-versa. Secondly when the sources are closer than a beamwidth, the degree of rejection possible between rotor and stator sources depends on the axial beamwidth.

As well as being able to resolve axially, radial resolution is important for the identification of sources along an individual rotor blade or stator vane. Azimuthal resolution is important for the quantification of sources on adjacent blades or vanes.

To provide an overview of the resolution of the rotating-focus beamformer, we first consider the beamformer output due to a single rotating source when focused over three dimensions. We then investigate the resolution in the three dimensions individually.

3.5.1 Three-dimensional point-spread functions

Figure 3.6 shows a number of contours of constant beamformer output in the rotating reference frame due to a single ducted, rotating axial-dipole source at $r_s = 0.8a$ rotating at an equivalent tip Mach number of $M_t = 0.5$. Such contours are known in the literature as *point-spread functions*. Here 4 contours are plotted in the three-dimensional scanning region corresponding to regions where the beamformer output is 0.1dB,1dB,3dB and 6dB below the peak amplitude. The 6dB contour (figure 3.6d) shows a beamformer output that appears to spiral down the duct. This is consistent with the interpretation of the in-duct sound field as a summation of spinning modes that consist of spiral regions of constant phase.

In figure 3.6, at lower contour levels the effect of beamwidth, and the presence of sidelobes in the beam-pattern become more important to the overall response. In the following sections we will examine the influence of the array geometry, scanning location and frequency on the beamwidth of the beamformer. Recall that the measurement of p_Ω used in the beamformer formulation relies on first performing a modal decomposition. A commonly used microphone arrangement for modal decomposition is an array of wall mounted microphones arranged in rings at multiple axial locations. It is necessary therefore to also use such an arrangement of microphones for the focused beamformer. Figure 3.1 illustrates the parameters that define the microphone array geometry. These are, the number of rings, N_z, the number of microphones in each ring, N_θ, the axial spacing between adjacent rings, Δz, and the distance, δ_z, between the rotor plane and the first ring of the microphone array. We begin by considering the beamwidth in the axial direction.

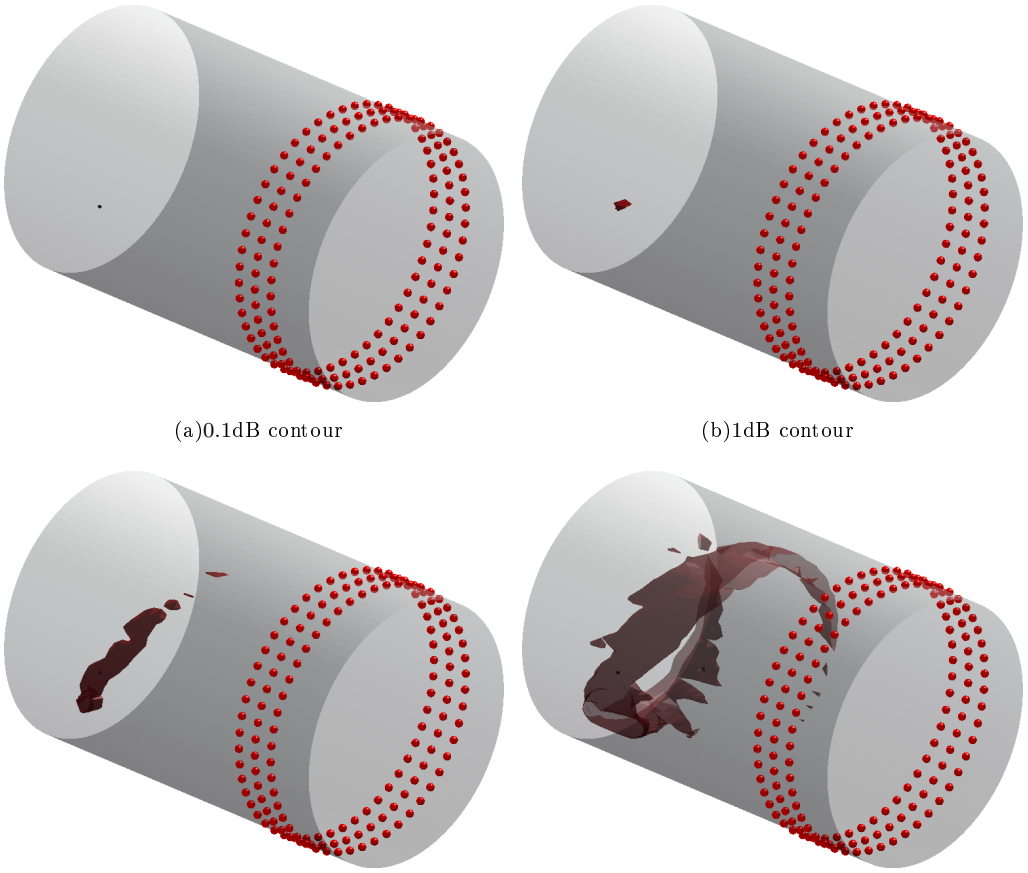

(a)0.1dB contour (b)1dB contour

(c)3dB contour (d)6dB contour

FIGURE 3.6: Point-spread functions at varying contour levels in the rotating reference frame for a single rotating source at $0.8r$ (shown as a small black dot).

3.5.2 Axial resolution

In this section we investigate the effect on axial beamwidth of changes in the array geometry. This has implications, as explained in section 3.4, on the degree of source discrimination possible when rotating and stationary sources are close together.

In the simulations that follow the beamwidth is calculated from the beamformer output due to a single rotating source positioned at $r_s = 0.8a, \theta_s = 0, z_s = 0$. The beam is steered along an axial line from $z = -5\lambda$ to $z = 5\lambda$, and the beamwidth of the mainlobe is measured. Other factors, including uniform flow and source near field effects are the same as the simulations in section 3.4.

The influence of array length, number of microphones per ring and distance between array and source are presented in the following three sections. In section 3.5.2.4 we consider the variation of beamwidth with frequency. Finally, in section 3.5.2.5 a simple analytical model is presented to help explain some of the findings.

3.5.2.1 Axial resolution as a function of N_θ

We first consider the effect on the axial beamwidth of varying the number of microphones in each ring. The axial beamwidth, $\Delta z_{\frac{1}{2}}$, is calculated at a frequency of $ka = 10$ for an array with 1,2 and 10 rings of microphones. Each ring contains N_θ microphones, where N_θ is varied from 1 to 60. The array length, $(N_z - 1)\Delta z$, is kept fixed at 1λ. A plot of the axial beamwidth as a function of N_θ/m_T is shown in figure 3.7, where m_T is the maximum azimuthal mode order present in the formulation of the modified pressure p_Ω,

$$m_T = \frac{ka}{1 - M_t} + \frac{ka}{1 + M_t} + 1 \tag{3.17}$$

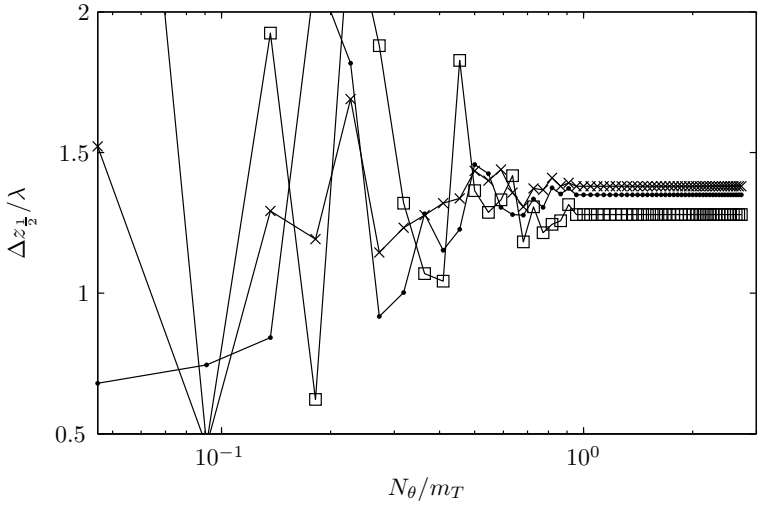

FIGURE 3.7: Axial beamwidth as a function of the number of microphones per ring for a one-ring (squares), two-ring (crosses) and ten-ring (dots) microphone array.

Notice that when $N_\theta > m_T$, the number of microphones per ring ceases to affect the beamwidth of the array. It is interesting to note that a finite axial beamwidth is achieved through the use of a single ring of sensors (squares), suggesting that axial focus is possible even with a single ring. For arrays where $N_\theta < m_T$, the beamwidth is highly dependent on both N_θ and array length. Arrays with more rings show smaller variations in beamwidth than those with fewer rings when N_θ is greater than approximately $0.5m_T$. This is due to the additional phase information available to the array when multiple rings are used. In general the axial beamwidth tends close to $\lambda(1+M) \approx 1.2\lambda$ for all arrays investigated.

3.5.2.2 Effect of array length on axial resolution

In this section we investigate the influence of microphone array length, L_z, on axial beamwidth. The frequency of calculation is $ka = 10$ and beamwidth is calculated for an array with between 2 and 10 rings of microphones with 25 microphones in each ring (such that $N_\theta/m_T = 1.14$). Figure 3.8 is a plot of the axial beamwidth, $\Delta z_{\frac{1}{2}}/\lambda$, as a function of microphone array length normalised on λ.

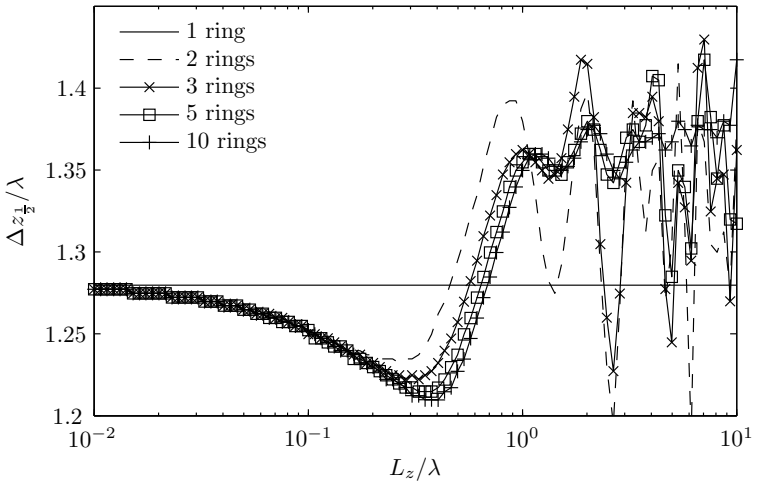

FIGURE 3.8: Axial beamwidth as a function of array length.

The variation of beamwidth with array length is observed to be small at approximately 0.2λ. For array lengths shorter than approximately 0.05λ, arrays with multiple rings have a beamwidth that tends to that of a single ring. Note that the beamwidth is minimum, and only weakly dependent on array length, for arrays with a total length of approximately 0.5λ. For arrays longer than a wavelength, the beamwidth approaches 1.35λ. Arrays with more rings, and lengths greater than 1λ, have a weaker dependence of beamwidth on array length.

3.5.2.3 Effect of array position on axial beamformer output

The final array geometry parameter to be investigated is the axial distance, δz, between the beamformer scanning plane and the first ring of the microphone array. Figure 3.9 is a plot of axial beamformer output $|b(z)|$, calculated for an array of length 1λ consisting of 5 rings of 25 microphones. The separation distance δz varies from 1λ to 200λ.

Figure 3.9 shows that $\Delta z_{\frac{1}{2}}$ is independent of the distance of the array from the source, and is in all cases approximately 1.2λ. A particularly interesting feature of figure 3.9 is that when the array overlaps the scanning region, as is the case when $\delta z = 1\lambda$ (the solid curve in figure 3.9), the beamformer output is very small in the region inside, and beyond, the array. This effect is explained in section 3.5.2.5.

3.5.2.4 Effect of frequency on axial resolution

This section examines the dependence of $\Delta z_{\frac{1}{2}}$ on the measurement frequency and the rotational frequency of the source. Figure 3.10 is a plot of the axial beamwidth as a function of frequency for the two different source rotational speeds of $M_t = 0$ and $M_t = 0.5$. The source is located at $r_s = 0.8a$. With the source stationary (figure

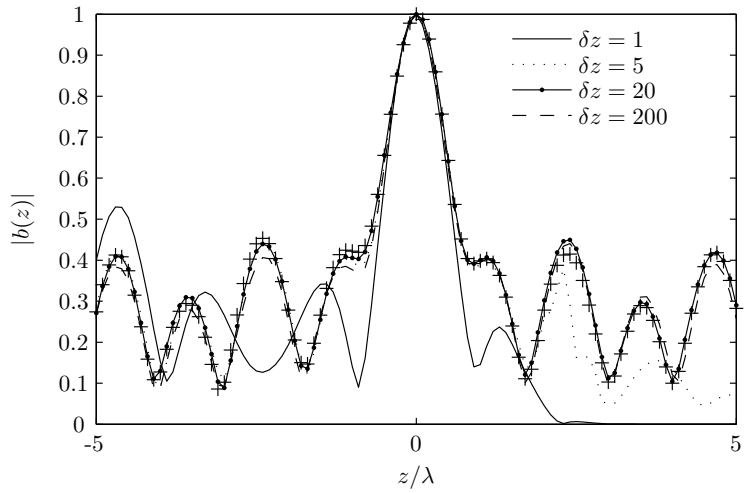

FIGURE 3.9: Axial beamformer output $|b(z)|$, calculated for an array of length 1λ consisting of 5 rings of 25 microphones as a function of axial scanning location. The separation distance, δz, between the first ring of the microphone array and the source varies from 1λ to 200λ. In each case, the array is located on the right hand side of the figure.

3.10(b)) the beamwidth tends to infinity at frequencies close to the cut-on frequencies of the $(m,n) = (m,0)$ modes (marked with circles in figure 3.10(a)). Furthermore, at the cut-on frequencies of the $(m,n) = (m,n>0)$ modes (marked with crosses in figure 3.10(b)) the axial beamwidth remains close to λ. For a rotating source ($M_t = 0.5$ in figure 3.10(b)) the peaks in the curve are shifted to $\omega + m\Omega$. Thus, no axial rejection of the sources is possible at these cut-on frequencies.

Figure 3.11 shows the results of a repeat calculation of figure 3.10 but with a source at $r_s = 0.4a$. The peaks in the axial beamwidth curve are now associated with the $(m,n) = (m,0)$ modes as well as some of the $(m,n) = (m,n>0)$ modes. With a rotating source (figure 3.11(b)), the peaks have also shifted in frequency by $\omega + m\Omega$.

The location and frequency shift of the peaks in the axial beamwidth can be explained by considering the behaviour of the Green's function used in the beamformer formulation of equation (3.8). The peaks in the beamwidth-ka curve coincide with the singularities in equation (2.35). The denominator in equation (2.35) includes the axial wavenumber component $\kappa_{mn} = \sqrt{k^2 - (1-M^2)(\sigma_{mn}/a)^2}$ which is zero at the modal cuton frequency. At a cuton frequency the acoustic pressure is dominated by a single near-cuton mode. The location of the source therefore cannot be determined based on the spatial information provided by a single mode, and hence the beamwidth becomes very large. The reason this phenomena only affects $(m,n) = (m,0)$ modes, for a source at $r_s = 0.8a$, will be explained below.

How strongly the acoustic pressure is dominated by a single mode near cuton depends on how well this mode is couple to the source. In figures 3.10 and 3.11 the frequencies at which peaks in the beamwidth-ka curve occur depends on the radial location of the

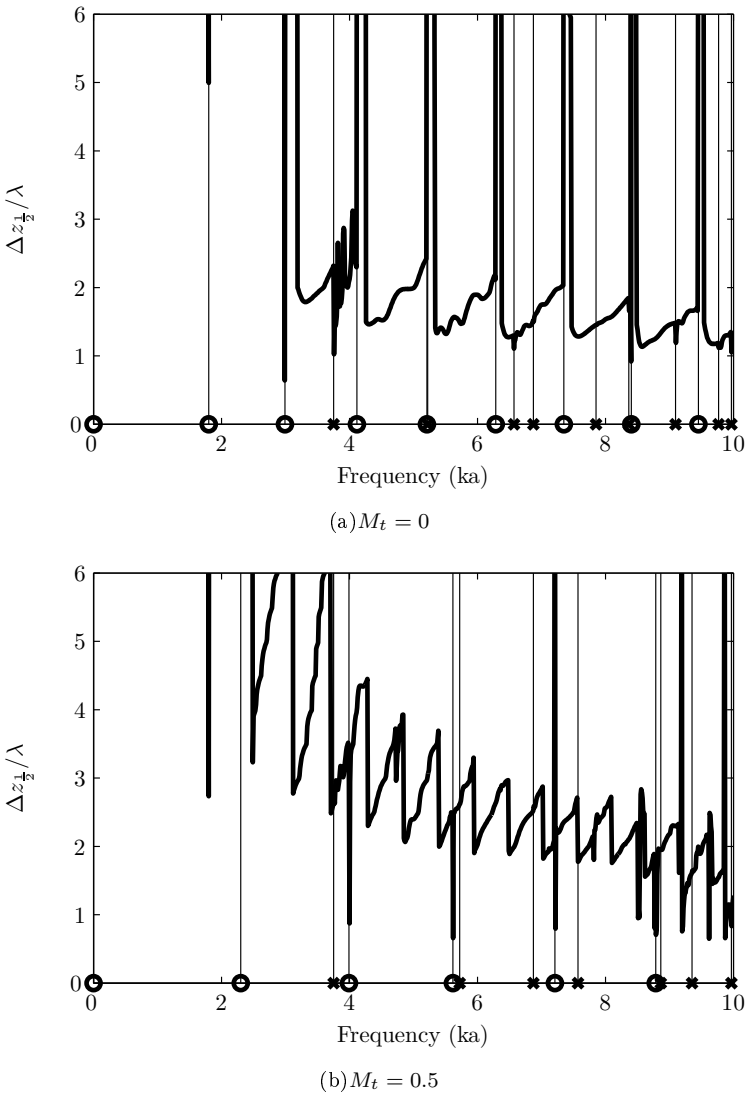

FIGURE 3.10: Axial beamwidth as a function of frequency at two different rotational speeds, $M_t = 0$ (a) and $M_t = 0.5$ (b). The source is located at $r_s = 0.8a$. Circles indicate the cut-on frequencies of the $(m, n) = (m, n = 0)$ modes; crosses indicate the cut-on frequencies of $(m, n) = (m, n > 0)$ modes.

source. Figure 3.12 is a plot of the mode shape functions versus radial location for a number of different modes. At a radial location $r = 0.8a$ the magnitude of the $(m, n) = (m, n > 0)$ mode shape functions are very small and therefore poorly coupled to a source at that radial location. Close to their cuton frequencies the denominator of equation (2.3) becomes very large, but this is counteracted by the behaviour of the numerator, which is proportional to the magnitude of the mode shape function and therefore becomes very small. Hence there are no peaks in the beamwidth-ka curve. At $r = 0.4a$ the magnitudes of some of the mode shape functions for $n > 0$ are comparable to those of the $n = 0$ modes. Sources at this radial position couple well with the $n > 0$ modes and hence result in a large beamwidth close to their cuton frequencies (figure 3.11).

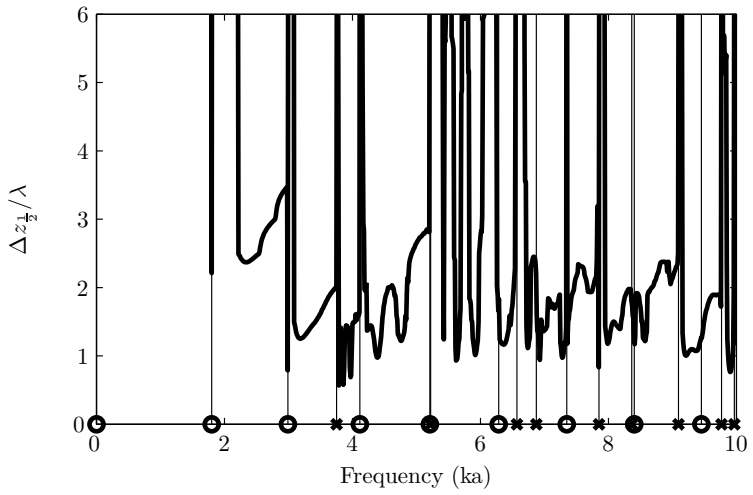

(a)$M_t = 0$

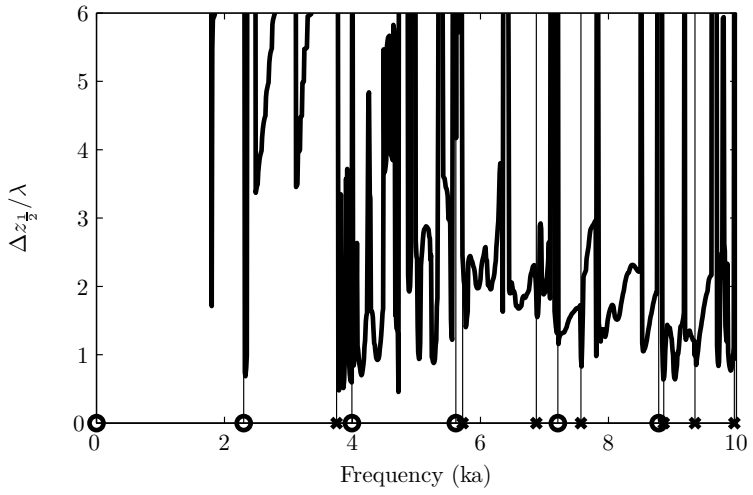

(b)$M_t = 0.5$

FIGURE 3.11: Axial beamwidth as a function of frequency at two different rotational speeds, $M_t = 0$ (a) and $M_t = 0.5$ (b). The source is located at $r_s = 0.4a$. Circles indicate the cut-on frequencies of the $(m, n) = (m, n = 0)$ modes; crosses indicate the cut-on frequencies of $(m, n) = (m, n > 0)$ modes.

3.5.2.5 High frequency analytical model of the axial beamformer

Many of the characteristics of the axial resolution of the beamformer can be explained by a simple one-dimensional model. The acoustic pressure in the duct due to a source at z_s is assumed to be sensed by an axial line of sensors. In the high frequency limit the pressure at the i^{th} sensor can be approximated by the sum of a continuous spectrum of axial wavenumber components. Ignoring the contribution to the measured pressure from variations of the path length difference in the r and θ directions we have,

$$p(z_i) = \int_{kM/(1-M^2)}^{k/(1-M)} p(k_z) e^{-\mathrm{i}k_z(z_i - z_s)} dk_z \tag{3.18}$$

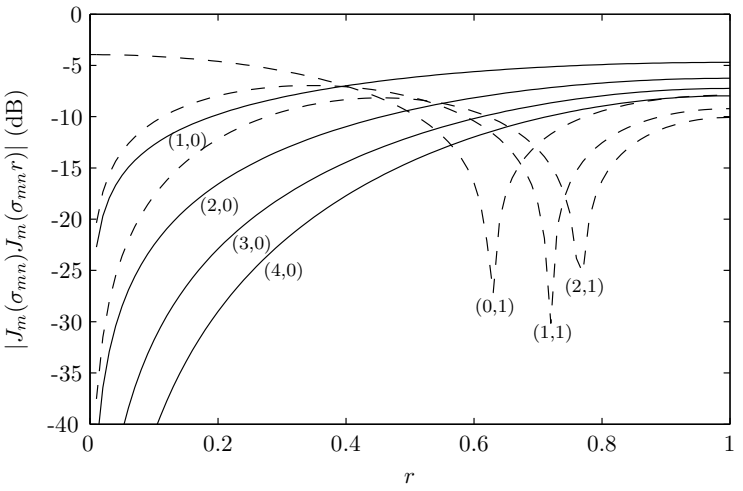

FIGURE 3.12: Product of the source and receiver terms of the mode shape function, $J_m(\sigma_{mn})J_m(\sigma_{mn}r)$, for various (m, n) combinations as a function of r.

where $p(k_z)$ is the pressure wavenumber spectrum. For simplicity the pressure contribution at each axial wavenumber is assumed to be constant, that is $p(k_z) = p_0$.

The beamformer output is given by

$$b(z_b) = \mathbf{w}^H \mathbf{p} \tag{3.19}$$

where $\mathbf{p} = [p(z_i) \dots p(z_{N-1})]$, z_b is the axial location of the focus point and $\mathbf{w} = (\mathbf{g}^H \mathbf{g})^{-1}\mathbf{g}$. Following equation (3.18) the Green's function is assumed to take the form,

$$g(z_i, z_b) = \int_0^{\frac{k}{1-M}} e^{-\mathrm{i}k_z(z_i - z_b)} dk_z \tag{3.20}$$

Noting that $k = \omega/c$, evaluating the integrals in equation (3.20) and (3.18) and inserting into equation (3.19), the beamformer output can be written

$$|b(z_b)| = \frac{\displaystyle\sum_{i=0}^{N-1} \frac{\sin \frac{1}{2}kz_i}{\frac{1}{2}kz_i} \frac{\sin \frac{1}{2}k(z_i - z_b)}{\frac{1}{2}k(z_i - z_b)}}{\displaystyle\sum_{i=0}^{N-1} \frac{\sin^2 \frac{1}{2}k(z_i - z_b)}{(\frac{1}{2}k(z_i - z_b))^2}} \tag{3.21}$$

where $z_s = 0$.

Figure 3.13 is a plot of the axial beamformer output calculated using the full formulation of equation (3.1) derived in section 3.2 with a 10 ring array with 25 microphones per ring at $ka = 10$ and axial flow speed $M = 0$. The source is located at $r_s = 0.8a$, and the first ring of the microphone array is at 10λ. The total length of the array is 1λ. The dotted curve in figure 3.13 is given by the simple model of equation (3.21) when, $z_i = -5\lambda, -4\lambda, \cdots, 0, \cdots, 4\lambda, 5\lambda$. In equation (3.21) the microphone locations are close

to the scanning locations, $z_i \approx z_b$, and for suitably large N equation (3.21) converges to

$$|b(z_b)| = \frac{\sin \frac{1}{2}kz}{\frac{1}{2}kz} \tag{3.22}$$

and since $k = 2\pi/\lambda$, the zero crossings are located at $\pm a\lambda$, where a is an integer.

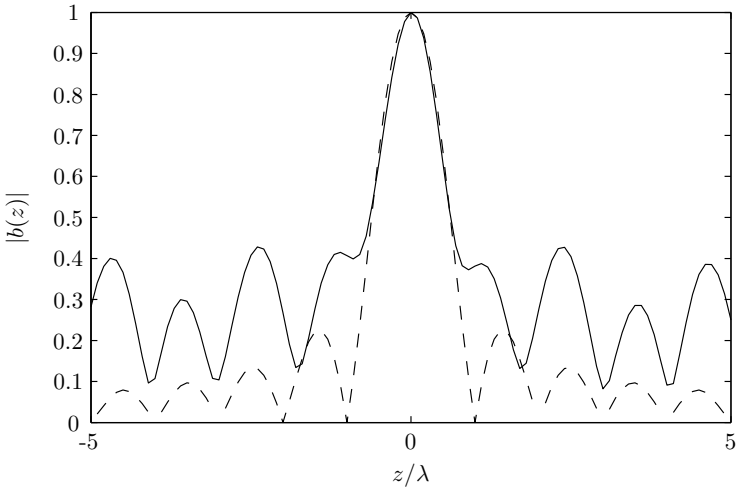

FIGURE 3.13: Comparison of the beamformer response calculated using the full model (solid line), and that predicted by the simple model in equation (3.21) (dotted line)

When the sensor array is moved far away from the source, the simple model fails to predict the beam response given by the full formulation. With the array far away from the source, the path differences between individual sensors becomes small, and the simple model beamformer can no longer focus on the source. In the full formulation this is not the case - with sensors arranged in rings the path length differences are maintained, and focusing in the axial direction is possible.

3.5.3 Azimuthal resolution

In this section we investigate the azimuthal resolution of the beamformer. A narrow beamwidth in the azimuthal direction is required if the beamformer is to resolve sources on adjacent fan blades. To be able to measure the sources on a B-bladed fan, the beamwidth $\Delta\theta$ must be less than $2\pi/B$. In this section we first consider the influence of array geometry on the azimuthal beamwidth, and then investigate the effects of frequency. Azimuthal beamwidth is calculated from the beamformer output due to a single source at $r_s = 0.8a, \tilde{\theta}_s = 0, z_s = 0$ rotating with an angular speed of $M_t = 0.5$. The beam is rotated at $r = 0.8a, z = 0$, and the beamwidth, $\Delta\theta_{\frac{1}{2}}$, of the mainlobe is quantified.

3.5.3.1 Azimuthal resolution as a function of N_θ and array length

Figure 3.14 is a plot of beamwidth as a function of the number of microphones per ring, N_θ, for a microphone array with 1, 2, and a 10 ring microphone array of length 1λ. In figure 3.14 the variation in beamwidth for $N_\theta < m_T$, reduces as the number of rings increases. When there are at least as many sensors per ring, N_θ, as azimuthal modes included in the calculation of $\mathbf{G}_\Omega$, the beamwidth is independent of N_θ.

Note that for rotating sources, $m^+ > m^-$ and therefore $m_T < 2m^+$; in other words, the number of sensors per ring required for beamforming is less than that required to perform the model decomposition necessary for the measurement of p_Ω. For all practical microphone arrays the number of microphones will be sufficient to perform in-duct beamforming.

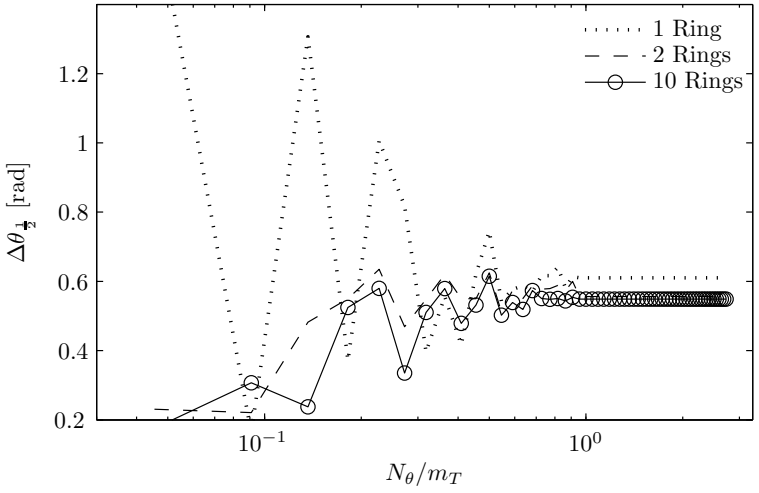

FIGURE 3.14: A plot of beamwidth in the azimuthal direction as a function of the number of microphones per ring, N_θ, for a 1,2, and 10 ring microphone array of length 1λ.

The behaviour observed in figure 3.14 can be explained by the use of a simple model. Consider N_θ sensors equally spaced in a single ring mounted in a duct containing $m_T = m^+ + m^- + 1$ spinning modes. A simple one-dimensional model, that ignores the path length differences in the radial and axial directions of the Green's function between a point source at θ_b and a receiver at θ_i is

$$g(\theta_i, \theta_b) = \sum_{m=m^-}^{m^+} e^{\mathrm{i}m(\theta_i - \theta_b)} \tag{3.23}$$

The pressure at the i^{th} sensor due to a source of unit strength at θ_s is therefore given by

$$p(\theta_i) = \sum_{m=m^-}^{m^+} e^{\mathrm{i}m(\theta_i - \theta_s)} \tag{3.24}$$

The beamformer output is formed by multiplying the vector of measured pressures $\mathbf{p} = [p(\theta_1), \ldots, p(\theta_{N_\theta})]$, by the weighting vector $\mathbf{w} = [w(\theta_1, \theta_b), \ldots, w(\theta_{N_\theta}, \theta_b)]$ where

$$w(\theta_i, \theta_b) = \left[g^H(\theta_i, \theta_b) g(\theta_i, \theta_b)\right]^{-1} g(\theta_i, \theta_b) = \sum_{m=m^-}^{m^+} \sum_{m'=m^-}^{m^+} \sum_{m''=m^-}^{m^+} e^{\mathrm{i}(m-m')(\theta_i-\theta_b)} e^{\mathrm{i}m''(\theta_i-\theta_b)} \tag{3.25}$$

The beamformer output is therefore

$$b(\theta_b) = \mathbf{p}\mathbf{w}^H = \sum_{i=1}^{N_\theta} \sum_{m=m^-}^{m=m^+} e^{\mathrm{i}m(\theta_i-\theta_s)} \sum_{m=m^-}^{m^+} \sum_{m'=m^-}^{m^+} \sum_{m''=m^-}^{m^+} e^{\mathrm{i}(m-m')(\theta_i-\theta_b)} e^{\mathrm{i}m''(\theta_i-\theta_b)} \tag{3.26}$$

For $N_\theta > m_T$ equation (3.26) reduces to

$$|b(\theta_b)|^2 = |\frac{1}{N_\theta} \sum_{m=m^-}^{m^+} e^{\mathrm{i}m(\theta_s-\theta_b)}|^2 \approx \frac{\sin^2 m_T(\theta_s - \theta_b)}{m_T^2(\theta_s - \theta_b)^2} \tag{3.27}$$

The zero crossings in the $\sin x/x$ function in equation (3.27) occur when $\theta_s - \theta_b = \pi/m_T$. Therefore the beamwidth, determined from the "distance" between the two zero crossings on either side of the main lobe, is $2\pi/m_T$. This is in agreement with the beamwidth observed in the simulations, and also azimuthal resolution limit established for the inversion technique in section 2.3.5.1. The resolution limit for the inversion technique was a "hard" limit below which inversion was impossible due to very poorly conditioned matrices, whereas with a beamformer, discrimination of sources becomes gradually poorer as they are moved closer together than a beamwidth.

Note that since m_T is the total number of propagating modes, the beamwidth decreases as the frequency increases. This also explains why beamwidth is largely independent of the microphone array geometry; as long as the microphone array is sufficient to perform the modal decomposition, the best possible beamwidth can be achieved.

3.5.3.2 Azimuthal beamwidth as a function of array length

In the previous section we established that the number of microphones required in each ring of the microphone array must be greater than the total number of modes included in the calculation of $\mathbf{G}_\Omega$. In this section we investigate whether azimuthal beamwidth is dependent on the length of the array.

Figure 3.15 is a plot of the azimuthal beamwidth as a function of the array length for microphone arrays with 1,2,3,5 and 10 rings of microphones. Each ring has 25 microphones, such that $N_\theta/m_T = 1.14$.

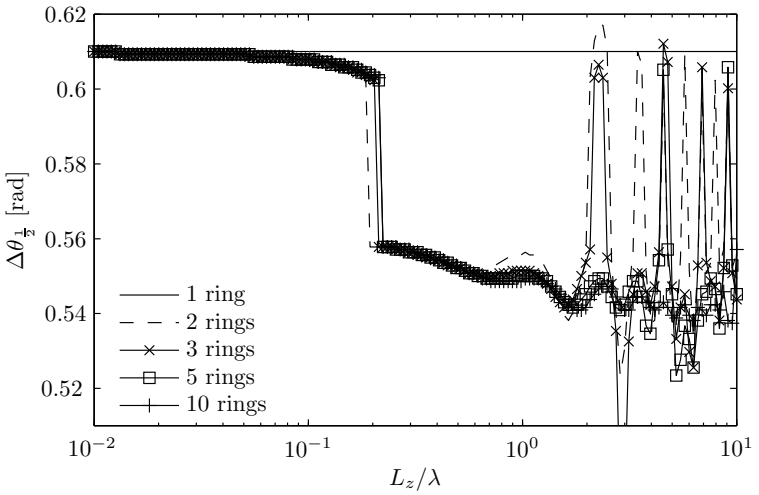

FIGURE 3.15: Azimuthal beamwidth as a function of array length for microphone arrays with 1,2,3,5 and 10 rings of 25 microphones.

In figure 3.15 the very short arrays ($L_z/\lambda < 0.1$) have a beamwidth that is very close to that of a single ring. For longer arrays the beamwidth for each array tends to $\Delta\theta_{\frac{1}{2}} \approx 0.54$. At $L_z/\lambda \approx 0.2$ the beamwidth exhibits a sudden jump. The cause of this jump is unclear, but is possibly due to a numerical artifact. Note that the scale on the y-axis is comparatively small, and this exaggerates the appearance of the jump.

3.5.3.3 The effect of frequency on azimuthal resolution

In this section we investigate the dependence of the azimuthal beamwidth on the measurement frequency. In figure 3.16 the dashed curve is a plot of azimuthal beamwidth as a function of frequency. At each frequency the microphone array is a single ring of $N_\theta = m_T$ microphones.

The solid curve in figure 3.16 is described by the equation $\Delta\theta_{\frac{1}{2}} = 2\pi/m_T$. The two curves have a very similar gradient, with the small difference in magnitude being dependent on the definition of beamwidth. Figure 3.16 demonstrates that the azimuthal resolution depends strongly on the highest mode order present, or in other words, on the highest spatial frequency component in the azimuthal direction. The peaks in the beamwidth-*ka* curve correspond to modal cuton frequencies, and were investigated in the context of axial resolution in section 3.5.2.4.

3.5.4 Radial resolution

In this section we investigate the radial resolution of the beamformer. Radial resolution is important as a measure of the ability of the beamformer to quantify the distribution of source strength along individual rotor and stator blades.

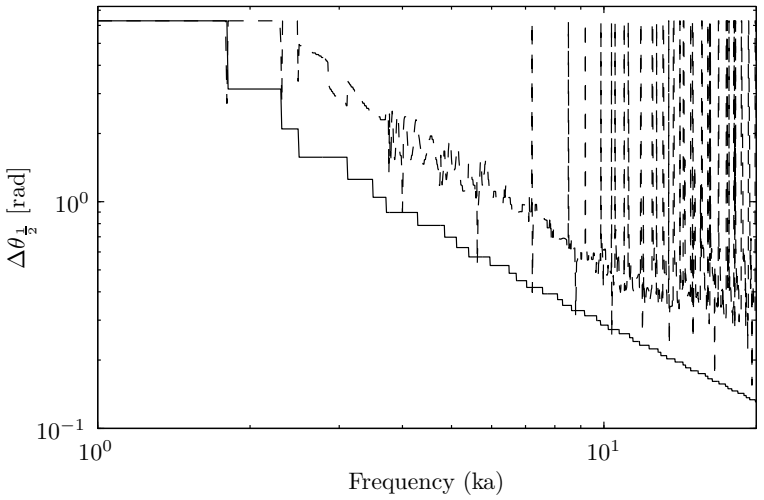

FIGURE 3.16: Azimuthal beamformer width as a function of frequency. The solid line is a plot of the equation $\Delta\theta_{\frac{1}{2}} = 2\pi/m_T$

The beamformer output $|b(r)|$ is predicted for a single point dipole source located at a radial distance r_s, rotating with an angular velocity $M_t = 0.5$. Figure 3.17 shows some example beamformer output at $ka = 20$ as a function of radial scanning position, for different source locations, calculated for an array with 3 rings of 50 sensors.

3.5.4.1 Effect of N_θ on radial beamwidth

In this section the source is located at $r_s = 0.8a$, and the frequency of calculation is $ka = 10$. Figure 3.18 is a plot of radial beamwidth, $\Delta r_{\frac{1}{2}}$ as a function of the number of microphones per ring for a 1, 2 and 10 ring microphone array. As is the case for azimuthal and axial resolution, it is necessary for the number of microphones per ring to be greater than m_T for the beamwidth to become independent of N_θ.

3.5.4.2 Effect of array length on radial beamwidth

In the previous section we established that in order for beamwidth to be independent of N_θ the condition $N_\theta > m_T$ must be satisfied. We now consider the effect on $\Delta r_{\frac{1}{2}}$ of varying the array length. Figure 3.19 is a plot of radial beamwidth as a function of array length L_z for an array with between 2 and 10 rings of 25 microphones per ring ($N_\theta/m_T = 1.14$). The beamwidth obtained with a single ring is plotted for comparison. Figure 3.19 shows that for arrays longer than 2λ, the beamwidth is at its narrowest and becomes weakly dependent on array length. Arrays with a greater number of rings exhibit a weaker dependence of beamwidth on array length than those with fewer rings. However increasing the number of rings has no significant effect on the average beamwidth.

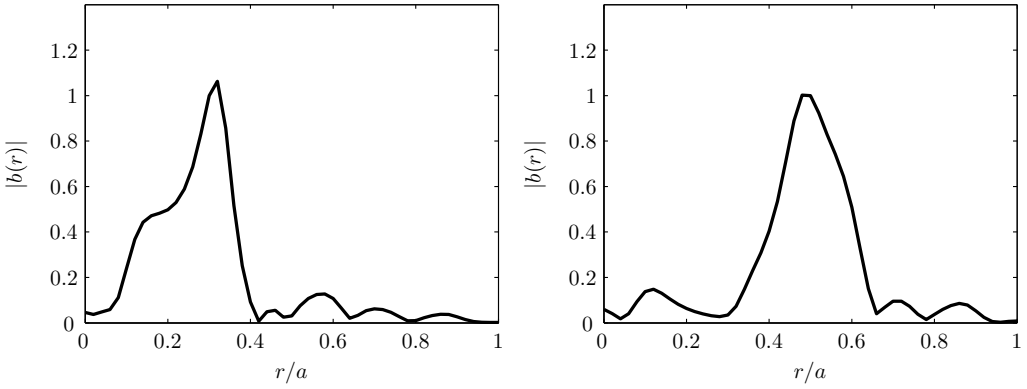

(a)Source located at $r_s = 0.3a$

(b)Source located at $r_s = 0.5a$

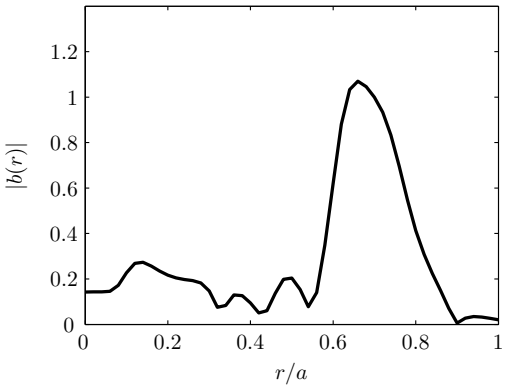

(c)Source located at $r_s = 0.7a$

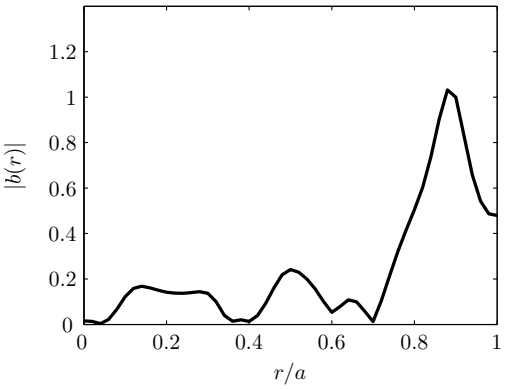

(d)Source located at $r_s = 0.9a$

FIGURE 3.17: Beamformer output $b(r)$ as a function of radial scanning location, r, for a single point dipole source, rotating at $M_t = 0.5$, located at varying radial locations r_s.

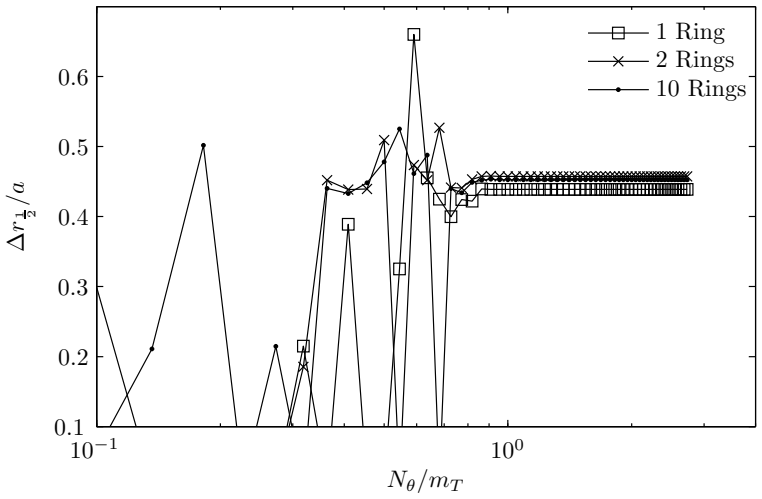

FIGURE 3.18: A plot of radial beamwidth, $\Delta r_{\frac{1}{2}}$ as a function of the number of microphones per ring, N_θ for a 1,2 and 10 ring microphone array.

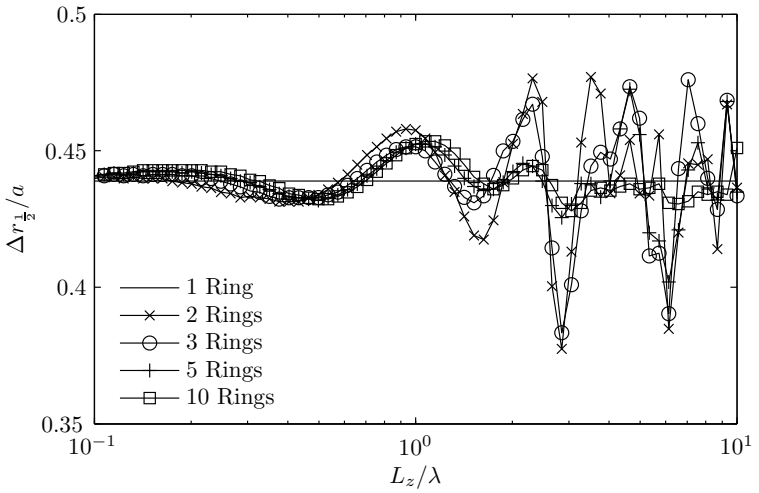

FIGURE 3.19: A plot of radial beamwidth, $\Delta r_{\frac{1}{2}}$ as a function of array length L_z for an array with between 2 and 10 rings of 25 microphones per ring such that $N_\theta/m_T = 1.14$.

3.5.4.3 Effect of frequency on radial resolution

In section 3.5.3.3 we noticed that the azimuthal beamwidth is strongly dependent on the number of modes. As a result it is to be expected that as the frequency increases, and the number of propagating radial modes increases, the radial beamwidth will also decrease. Figure 3.20 is a plot of radial beamwidth as a function of frequency calculated using a single ring microphone array with m_T microphones. The source is located at $r_s = 0.8a$. Note that below approximately $ka = 10$ the beamwidth as measured by the 3dB down point is larger than the duct radius, and hence by this measure, beamwidth is undefined. Above $ka = 10$ radial beamwidth is approximately proportional to $1/n_0$.

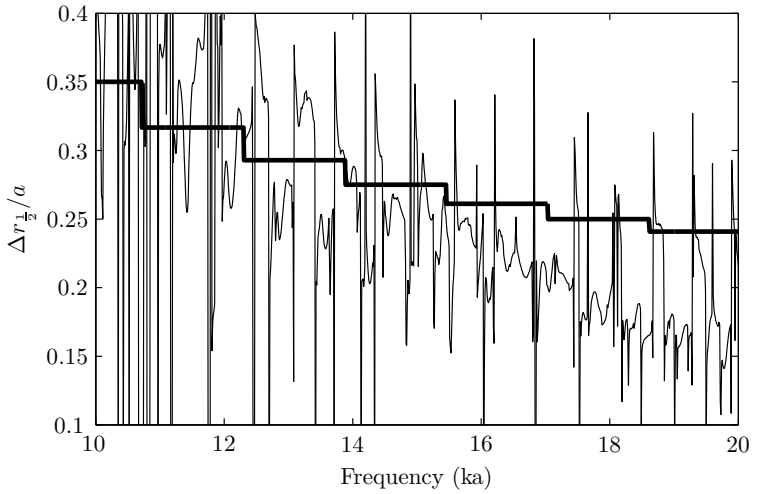

FIGURE 3.20: Radial beamwidth as a function of frequency calculated for a source at $r_s = 0.8a$ with a single ring of m_T microphones. The solid black line is proportional to $1/n_0$.

3.6 Conclusions

An experimental technique, based on a rotating focus beamformer, has been proposed. Beamforming is based on the measurement of a modified pressure, and the formulation of a modified Green's function that allows the point of focus to rotate at the same speed as the rotor.

The rotating-focus beamformer is able to differentiate between rotor and stator based sources by virtue of two properties:

1. A finite mainlobe and sidelobe rejection common to all phased-array beamformers.
2. Additional suppression of stationary sources when detected by a rotating beam and vice-versa, due to the "smearing" effect.

The resolution limits of the beamformer have been investigated in detail, and can be summarised to give the following microphone array design guidelines for in-duct beamforming:

- The array should consist of multiple rings. In each ring the number of sensors, N_θ, should be greater than the number of modes, m_T, included in the calculation of $\mathbf{G}_\Omega$. Where $m_T = \frac{ka}{1-M_t} + \frac{ka}{1+M_t} + 1$.
- Optimal axial and azimuthal beamwidth is achieved for an array of length less than one wavelength.
- Care must be taken to avoid beamforming at frequencies close to the modal cuton frequencies. This becomes increasingly difficult at higher frequencies, where the cuton frequencies become increasingly closer together as frequency is increased.

Chapter 4

Estimation of far-field directivity using an in-duct axial array

4.1 Introduction

This chapter presents a measurement technique that estimates the far-field directivity of the sound radiated from a duct from measurements of pressure made inside the duct. The technique is restricted to broadband, multi-mode sound fields whose directivity patterns are axi-symmetric, and whose modes are mutually uncorrelated. The principle application of the technique is for fan rigs where direct measurement of directivity, for example by use of an anechoic chamber, is impossible.

The technique is based on the observation that the angle of the main radiation lobe associated with a particular mode is close to the in-duct axial propagation angle [56]. In the no-flow case the two angles are identical. The variation of in-duct mean square pressure with axial propagation angle, ϕ, is estimated by an axial beamformer comprising a number of uniformly spaced microphones located at the duct wall . The far-field radiation, $|p_f(\phi,\omega)|^2$, is then related to the beamformer output, $|b(\phi,\omega)|^2$, via a transfer function, $|H(\phi,\omega)|^2$,

$$|p_f(\phi,\omega)|^2 = |H(\phi,\omega)|^2 |b(\phi,\omega)|^2 \tag{4.1}$$

where $|H(\phi,\omega)|^2$ is predicted from numerical simulation. Note that for a semi-infinite duct containing mutually incoherent modes in which reflection can be ignored, $|b(\phi,\omega)|^2$, is indepedent of the location of the array within the duct. Later we predict $|H(\phi,\omega)|^2$ for zero-flow hollow cylindrical ducts, and idealised aeroengine inlets and exhausts.

Crucially, the measurement principle is only useful if the transfer function, $|H(\phi,\omega)|^2$, does not depend on the amplitude distribution (or equivalently the sound source distribution) in the duct. This requirement will be investigated later in the chapter. We begin

by expressing the pressure field in the duct in terms of mode-ray angles, this allows for a more intuitive derivation of the beamformer response as a function of beam-steer angle.

4.2 Theory

4.2.1 In-duct sound field in terms of mode-ray angles

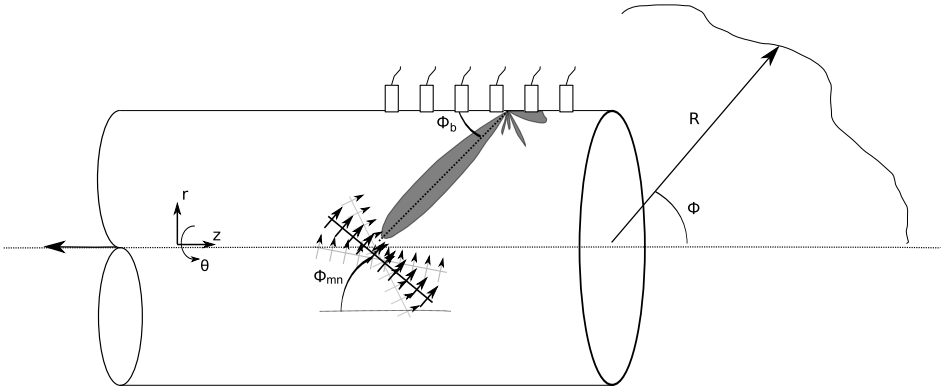

FIGURE 4.1: A schematic of the measurement setup. An axial array of microphones mounted at the duct wall are used to steer a beam at an angle ϕ_b. Individual modes are incident on the array with mode-ray angles ϕ_{mn}. The polar radiation angle is denoted ϕ

At a single frequency, ω, the sound field in a semi-infinite, hard-walled, hollow cylindrical duct with uniform mean-flow, M, is of the form,

$$p(\mathbf{x},\omega) = \sum_{mn} A_{mn}\Psi_{mn}e^{\mathrm{i}(k_{zmn}z+\omega t)} \tag{4.2}$$

where $\mathbf{x} = (r,\theta,z)$ is a location in the duct coordinate system and Ψ_{mn} is a normalised mode of pressure amplitude A_{mn}. Mode shape functions for cylindrical and annular ducts and their normalisation constants are given in appendix A. In the following, it is convenient to use the notation given by Chapman[57]. Equation (4.2) can be re-written,

$$p(\mathbf{x},\omega) = \sum_{mn} A_{mn}\Psi_{mn}e^{\mathrm{i}(M+\cos\bar{\phi}_{mn})k\bar{\bar{z}}+i\omega t} \tag{4.3}$$

Here the pressure is expressed in Prandtl-Glauert transformed coordinates, with a bar denoting devision by the Doppler factor $\beta = \sqrt{(1-M^2)}$, and unless otherwise stated a double bar denoting division by β^2.

In this notation $\bar{\phi}_{mn}$ is the transformed mode ray angle of the mode (m,n) lying in the range $0 \leq \bar{\phi} \leq \pi/2$, defined by,

$$\sin\bar{\phi}_{mn} = \frac{\sigma_{mn}}{k\bar{a}} \tag{4.4}$$

where σ_{mn} is the eigenvalue of the m, n^{th} mode. The axial wavenumber is given by

$$k_{zmn} = (M + \cos\bar{\phi}_{mn})k/\beta^2 \tag{4.5}$$

Note that $\bar{\phi}_{mn}$ is related to the actual propagation angle ϕ_{mn} by

$$\sin\phi_{mn} = \frac{\sin\bar{\phi}_{mn}}{(1 - M^2\cos^2\bar{\phi}_{mn})^{\frac{1}{2}}} \tag{4.6}$$

4.2.2 Far-field radiation

Our investigation of $|H(\phi,\omega)|^2$, defined in equation (4.1), will initially be predicted using the far-field modal directivity pattern for a flanged, semi-infinite duct. The expression, expressed here in Chapman's [57] notation, for far-field radiation in which the flow speed is the same everywhere is

$$p_f(\bar{\phi},\omega) = \sum_{mn} A_{mn}\Lambda_{mn}a^2\cos\bar{\phi}_{mn}\frac{(-i)^{m+1}k}{2\beta^2\bar{\bar{R}}}e^{-\mathrm{i}m\theta+iMk\bar{\bar{z}}+ik\bar{\bar{R}}}d(\bar{\phi},\bar{\phi}_{mn}) \tag{4.7}$$

where $\bar{\bar{R}} = (\bar{\bar{z}}^2 + \bar{r})^{\frac{1}{2}}$ (see figure 4.1) is the distance from the centre of the open duct face to the far-field measurement location, and

$$d(\bar{\phi},\bar{\phi}_{mn}) = \frac{-2(\sin\bar{\phi})J'_m(k\bar{a}\sin\bar{\phi})e^{-\mathrm{i}k\bar{\bar{d}}(\cos\bar{\phi}-\cos\bar{\phi}_{mn})}}{k\bar{a}(1 - m^2/\sigma_{mn}^2)J_m(\sigma_{mn})(\sin^2\bar{\phi} - \sin^2\bar{\phi}_{mn})} \tag{4.8}$$

are the non-dimensional modal directivity functions given by Chapman [57] such that $d(\bar{\phi},\bar{\phi}_{mn}) = 1$ for $\bar{\phi} = \bar{\phi}_{mn}$. Rice showed that the angle $\bar{\phi}_{mn}$ at which peak radiation occurs corresponds to the group velocity angle, i.e. the angle at which energy is transmitted from the duct.

In section 4.5 we use a more realistic model for far-field radiation to predict $|H(\phi,\omega)|^2$ that takes into account, for example, shear layers in the flow and geometry effects.

4.2.3 Beamformer formulation

The axial beamformer comprises N equally spaced microphones arranged along the duct wall, $\bar{r}_l = \bar{a}$, at a fixed circumferential position, such that $\bar{\bar{z}}_l = l\Delta z/\beta^2$ ($l = 0, 1, \ldots, N-1$), where Δz is the spacing between adjacent microphones at the duct wall. The beamformer response is formulated by multiplying the complex pressures at each microphone by a complex weighting coefficient, w_l^*, and summing such that the signals at each microphone add in phase for a single mode propagating at the beam-steer angle,

$\bar{\phi}_b$,

$$b(\bar{\phi}_b, \omega) = \frac{1}{N} \sum_{l=0}^{N-1} p(\bar{\bar{z}}_l, \omega) w_l^*(\bar{\phi}_b) \tag{4.9}$$

where

$$w_l(\bar{\phi}_b) = e^{+i(M+\cos\bar{\phi}_b)k\bar{\bar{z}}_l} \tag{4.10}$$

Substituting equation (4.3) for the pressure into (4.9) gives

$$b(\bar{\phi}_b, \omega) = \sum_{mn} A_{mn} \Psi_{mn} T(\bar{\phi}_{mn}, \bar{\phi}_b) \tag{4.11}$$

where the time dependence has been dropped and $T(\bar{\phi}_{mn}, \bar{\phi}_b)$ is the beamformer response function,

$$T(\bar{\phi}_{mn}, \bar{\phi}_b) = \frac{1}{N} \sum_{l=0}^{N-1} e^{\mathrm{i}(\cos\bar{\phi}_{mn} - \cos\bar{\phi}_b)k\bar{\bar{z}}_l} \tag{4.12}$$

Note that because the phase delay in equation (4.10) is chosen to correspond to the modal phase velocity (see Chapman [57]) the dependence on Mach number in the beamformer response cancels and the maximum output of the beamformer occurs when the group velocity angle of the mode equals the beamformer angle, $T(\bar{\phi}_{mn}, \bar{\phi}_b) = 1$ for $\bar{\phi}_b = \bar{\phi}_{mn}$, that is the angle of the principal radiation lobe.

For broadband noise, the modes may be assumed to be uncorrelated and the mod-square beamformer output can be written as

$$|b(\bar{\phi}, \omega)|^2 = \sum_{mn} |p_w(\bar{\phi}_{mn}, \omega)|^2 |T(\bar{\phi}_{mn}, \bar{\phi}_b)|^2 \tag{4.13}$$

where $|p_w(\phi_{mn}, \omega)|^2$ is the square pressure at the duct wall due to the $(m,n)^{\text{th}}$ mode, given by, for the case of a hollow cylindrical duct,

$$|p_w(\bar{\phi}_{mn}, \omega)|^2 = \frac{|A_{mn}|^2}{1 - \frac{m^2}{\sigma_{mn}^2}} \tag{4.14}$$

where the term $[1 - \frac{m^2}{\sigma_{mn}^2}]^{-1}$, which arises from the normalisation constant given in Appendix A, can therefore be interpreted as the ratio of the squared pressure at the wall, $|p_w(\omega)|^2$, to that averaged over a duct cross-section, where

$$|p_w(\omega)|^2 = \sum_{mn} |p_w(\bar{\phi}_{mn}, \omega)|^2 \tag{4.15}$$

4.2.4 In-duct to far-field transfer function

Combining equations (4.1), (4.7), (4.13) and (4.14) the in-duct to far-field transfer function for a flanged duct is of the form,

$$4\left(\frac{\bar{\bar{R}}}{\bar{a}}\right)^2 |H(\bar{\phi},\omega)|^2 = \frac{(k\bar{a})^2 \sum_{mn} |A(\bar{\phi}_{mn})|^2 \Lambda_{mn}^2 |d(\bar{\phi},\bar{\phi}_{mn})|^2 \cos^2\bar{\phi}_{mn}}{\sum_{mn} |A(\bar{\phi}_{mn})|^2 \left(1-\frac{m^2}{\sigma_{mn}^2}\right)^{-1} |T(\bar{\phi}_{mn},\bar{\phi})|^2} \tag{4.16}$$

where the steer-angle of the beamformer matches the radiation angle, $\bar{\phi}_b = \bar{\phi}$.

An essential condition for the measurement technique to be valid is that the transfer function, $|H(\bar{\phi},\omega)|^2$, must be independent of the mode amplitude distribution. In subsequent sections we demonstrate that this condition does indeed hold for no-flow ducts, and typical exhaust and inlet configurations appropriate for aeroengine experiments.

4.2.4.1 Mode amplitude distribution models

The simulations later in the chapter are based on idealised mode amplitude distribution models. Joseph *et al.* [58] present a number of expressions for $|A(\bar{\phi}_{mn})|^2$ based on various models for sound generation in ducts. The first model used here assumes *equal amplitude per mode* and is,

$$|A(\bar{\phi}_{mn})^{\mathrm{ea}}|^2 = \mathcal{A}^2 \tag{4.17}$$

where $\mathcal{A}$ is the modulus of the modal pressure, assumed constant for all cut-on modes.

The second model assumes *equal energy per mode* namely that all cut-on modes carry equal sound power

$$|A(\bar{\phi}_{mn})^{\mathrm{ee}}|^2 = \frac{2\rho c}{\pi a^2}\varpi \frac{1}{(\cos\bar{\phi}_{mn})} \frac{(1-M\cos\bar{\phi}_{mn})^2}{\beta^2} \tag{4.18}$$

where ϖ is the sound power carried by a single mode above cut-off.

Joseph *et al.* [58] present another family of mode distribution models obtained by assuming that the source plane can be modelled as a distribution of incoherent point-sources of arbitrary temporal and spatial order, ν and μ respectively,

$$|A(\bar{\phi}_{mn})|^{\mu,\nu}|^2 \propto \frac{1}{\cos^2\bar{\phi}_{mn}} \left(\frac{M-\cos\bar{\phi}_{mn}}{\beta^2}\right)^{2\mu} \left(\frac{1-M\cos\bar{\phi}_{mn}}{\beta^2}\right)^{2\nu} \tag{4.19}$$

Under this indexing convention the source distributions take the indices $(\mu,\nu) = (0,2)$ for volume velocity (monopole) sources, a source distribution used later in the chapter.

4.3 No-flow results

In this section we will present some simulation results that illustrate the use of the technique for determination the radiation directivity from a hollow cylindrical duct with no-flow. Although this situation is unrepresentative of aeroengine situations the comparative simplicity of the problem allows physical interpretation of the results to be made. Additionally, this simplified case is analysed experimentally in chapter 5. In later sections the in-duct to far-field transfer function for more realistic exhaust and intake configurations are investigated.

4.3.1 Beamformer response due to the presence of a single mode

Figure 4.2 shows the beamformer output as a function of steering angle due to a single mode of unit amplitude at the duct wall, $|p_w(\phi_{mn}, \omega)|^2 = 1$, for the $(0,0)$, $(10,0)$ and $(17,0)$ modes for $M = 0$ at $ka = 20$. The array has 11 microphones separated by a distance $\Delta z = \lambda/2$ to give a total array length of 5λ. The maximum output of the beamformer in each case can be seen to correspond to the mode ray angles, which are $\phi_{mn} = 0°$, $\phi_{mn} = 36°$ and $\phi_{mn} = 73°$ respectively. Note also that the beamwidth increases as the beam is steered towards $\phi_b = 0$ (end-fire).

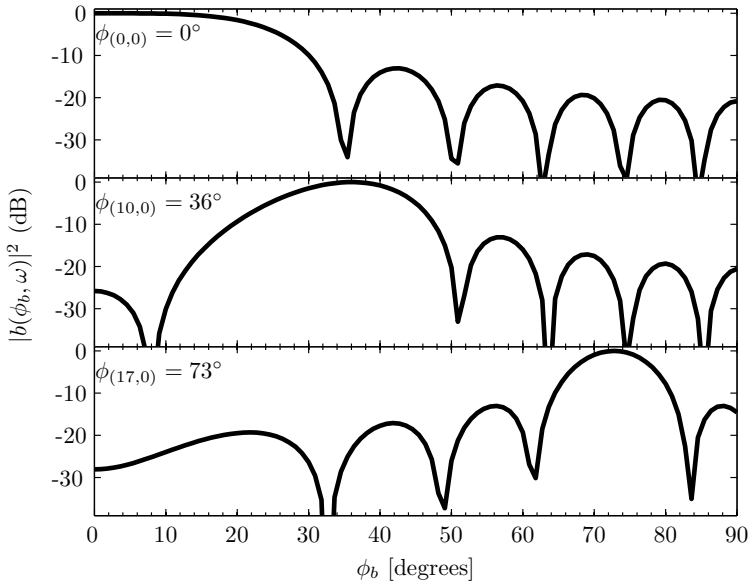

FIGURE 4.2: Beamformer output as a function of steering angle calculated for excitation by the $(0,0)$ (top), $(10,0)$ (middle) and $(17,0)$ (bottom) mode at $ka = 20$. As the mode order increases the modes become progressively less well cut-on and the mode-ray angle increases (equation (4.4)).

We now investigate the beamformer output for a multi-mode sound field for the idealised mode amplitude distribution models given in section 4.2.4.1.

4.3.2 Beamformer response to multi-mode sound field

Before presenting beamformer outputs due to multi-mode sound fields it is first necessary to introduce a beamwidth correction that must be applied at small beam-steer angles.

We can derive an expression for the variation of beamwidth with steering angle by noting that the beamformer directivity function, equation (4.12), for a fixed microphone spacing $\Delta\bar{\bar{z}}$, has the closed form expression

$$T(\bar{\phi}_{mn}, \bar{\phi}_b) = \frac{\sin\left[\frac{N}{2}k\Delta\bar{\bar{z}}(\cos\bar{\phi}_{mn} - \cos\bar{\phi}_b)\right]}{N\sin\left[\frac{1}{2}k\Delta\bar{\bar{z}}(\cos\bar{\phi}_{mn} - \cos\bar{\phi}_b)\right]} \tag{4.20}$$

We define the beamwidth, $\bar{\phi}_{\mathrm{BW}}$, as one-half of the angle between the first zero crossings, $T(\bar{\phi}_{mn}, \pm\bar{\phi}_0) = 0$, either side of the mainlobe peak $\bar{\phi}_{mn}$. The zero crossings occur when the numerator of equation (4.20) is zero. For simplicity we assume the beampattern is symmetrical about its peak. The beamwidth for a beam steered at $\bar{\phi}_b = \bar{\phi}_{mn}$ is given by,

$$\bar{\phi}_{\mathrm{BW}} = \frac{1}{2}[2(\bar{\phi}_0 - \bar{\phi}_{mn})] = \cos^{-1}\left[\frac{2\pi}{Nk\Delta\bar{\bar{z}}} - \cos\bar{\phi}_{mn}\right] - \bar{\phi}_{mn} \tag{4.21}$$

Equation (4.21) shows that the beamwidth is inversely proportional to the length of the array $L_z = (N-1)\Delta\bar{\bar{z}}$, and increases for $\bar{\phi}_{mn}$ close to zero. However a consequence of beamforming inside the duct is that as the mainlobe of the beam approaches the end-fire angles, progressively more of the mainlobe is "lost" to angles outside of the duct. The area under the mainlobe decreases, and in the multi-mode case this will cause a reduction in the beamformer output. To compensate for this, for angles from $\bar{\phi}_b = 0$ to $\bar{\phi}_b = \bar{\phi}_{\mathrm{BW}}$ the following correction is applied

$$b(\bar{\phi}_b) = \begin{cases} b(\bar{\phi}_b) + b(\bar{\phi}_{\mathrm{BW}} - \bar{\phi}_b) & \text{for } \bar{\phi}_b \leq \bar{\phi}_{\mathrm{BW}} \\ b(\bar{\phi}_b) & \text{for } \bar{\phi}_b > \bar{\phi}_{\mathrm{BW}} \end{cases} \tag{4.22}$$

this can be interpreted as adding to the beamformer output in the correction region that which would be measured "outside" of the duct.

Figure 4.3 is a plot of the corrected beamform output as a function of steering angle for the three mode models presented in section 4.2.4.1. The array parameters are $N = 11$, $\Delta\bar{\bar{z}} = \lambda/2$, the frequency is $ka = 20$. To allow the comparison between the different mode models the beamformer output is normalised by $\int_0^{\pi/2} |b(\phi, \omega)|^2 \sin\phi d\phi$. Note that in figure 4.3 the response due to an equal energy per mode sound field is very nearly independent of beam-steer angle for angles below approximately 70°.

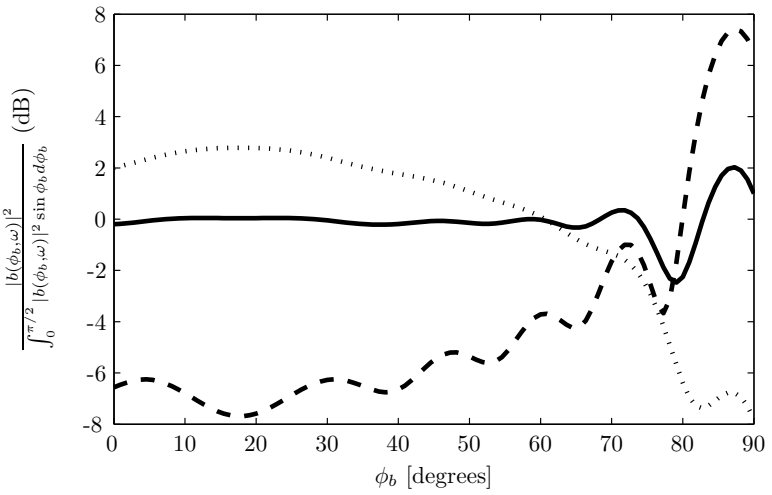

FIGURE 4.3: Beamformer output as function of steering angle for excitation at $ka = 20$ by an equal energy per mode sound field (solid), an equal modal amplitude sound field (dotted) and a distribution of volume velocity sources (dashed).

4.3.3 Influence of array length on beamformer output

In this section we investigate beamformer output as a function of array length in order to identify the minimum array length that allows details of the far-field directivity to be resolved. This is important because in typical applications the length of duct available to mount the array will be limited.

Figure 4.4 is a plot of the beamformer output for various array lengths of $L_z/\lambda = 2, 5, 10, 20$ and 50, as a function of steering angle, in the presence of an equal energy per mode sound field at $ka = 20$. In each case the beamformer output has been corrected for small angles by equation (4.22). To allow the curves in figure 4.4 to be compared, they are normalised using the procedure discussed in section 4.3.6.

For beam-steer angles between 0° and about 60°, collapse of the beamformer output for the various array lengths is better than 1 dB. Figure 4.4 shows that when appropriately normalised, the beamformer output is largely independent of the array length, even for the shortest array $L_z/\lambda = 2$.

The $L_z/\lambda = 50$ array has a highly oscillatory beamformer repsonse. This can be attributed to the large number of side-lobes present in the beam-pattern as the array length increases.

4.3.4 Far-field radiation from a zero flow cylindrical duct

Figure 4.5 is a plot of the far-field squared pressure versus polar angle, ϕ, predicted by equation (4.7) for a zero-flow cylindrical duct at $ka = 20$ when all the modes carry unit sound-power (solid curve). The dotted curve in figure 4.5 is the high-ka approximation to

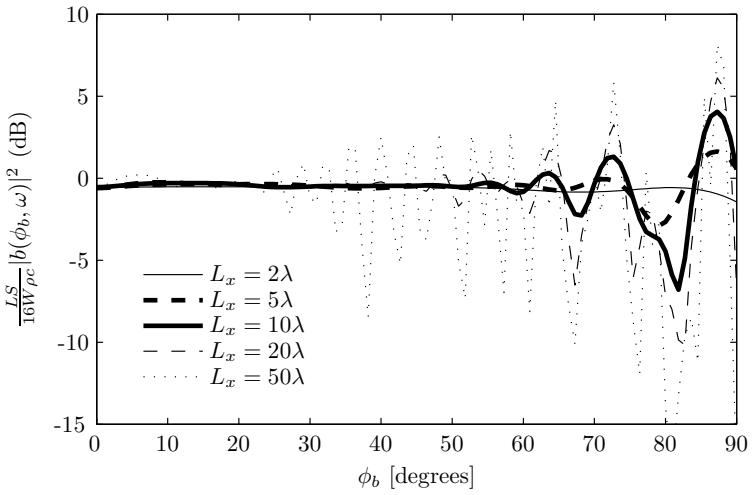

FIGURE 4.4: Beamformer output as a function of beam-steer angle for various lengths of array. The sound field has equal energy per mode at $ka = 20$

the directivity predicted by Joseph and Morfey [59] given by equation (4.23) in the next section. We use this high-ka approximation in section 4.3.6 to calculate an approximate transfer function. Note that agreement between the exact and asymptotic expression improves as ka tends to infinity.

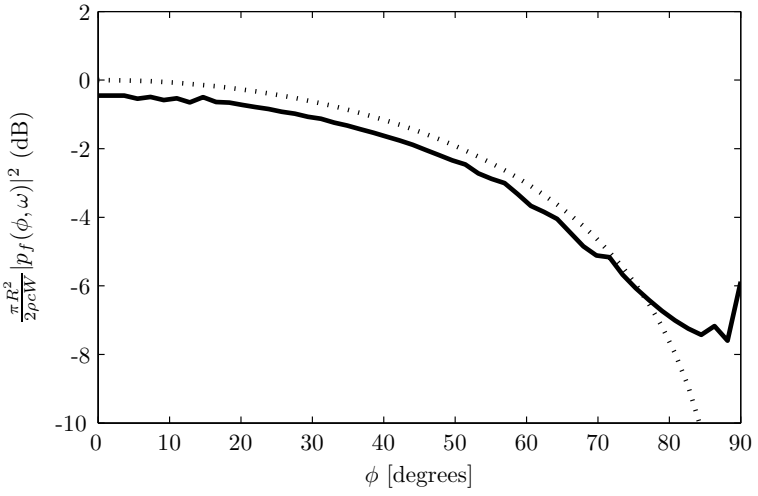

FIGURE 4.5: Comparison of the far-field radiation predicted by equation (4.7) (solid) with the $\cos\phi$ directivity predicted by Joseph and Morfey [59] (dotted) at $ka = 20$.

4.3.5 Transfer function $|H(\phi,\omega)|^2$ for the zero-flow cylindrical duct

Figure 4.6 is a plot of $|H(\phi,\omega)|^2$, calculated from equation (4.16), as a function of steering angle calculated for the three different mode amplitude distributions (equal amplitude, equal energy and volume velocity) at $ka = 20$. The in-duct array has a length $L_z = 5\lambda$ with $\Delta z = \lambda/2$, and zero flow is assumed. For normalisation purposes, $|H(\phi,\omega)|^2$ is multiplied by $(8/N)(R/a)^2$ as explained below.

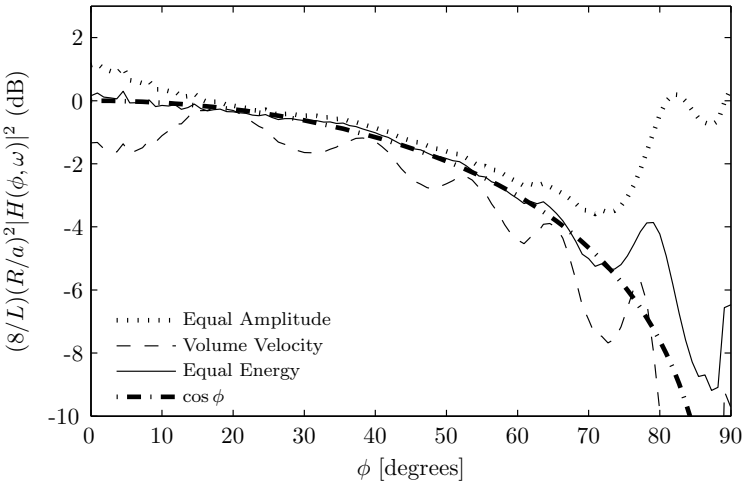

FIGURE 4.6: A plot of the transfer function $|H(\phi,\omega)|^2$ as a function of steering angle, calculated for three different mode amplitude distributions at $ka = 20$.

Figure 4.6 shows that for angles below approximately 70° the transfer function $|H(\phi,\omega)|^2$ is largely independent, to within 2dB, of the chosen mode amplitude distribution. The bold dash-dot curve in figure 4.6 is a high-ka approximation to equation (4.16) which shall be derived in the next section.

The largest deviation from the high-ka approximation is observed for the volume velocity source model. This is due to $|A_{mn}|^2$ rapidly approaching infinity for angles close to 90° in equation (4.19). This causes the beamformer response to be dominated by individual modes close to cut-on.

4.3.6 A high-ka approximation for the in-duct to far-field transfer function $|H(\phi,\omega)|^2$

The transfer function in equation (4.16) can be predicted from knowledge of the array length, number of microphones and their axial spacing, together with an appropriate radiation model. However, in this section we derive a simple analytic expression for $|H(\phi,\omega)|^2$ that is valid in the high-ka limit and for zero flow.

In the previous section we demonstrated that $|H(\phi,\omega)|^2$ is largely insensitive to the mode amplitude distribution. We are therefore free to choose any arbitrary distribution that allows us to formulate a closed form expression for $|H(\phi,\omega)|^2$. If we assume the sound field in the duct has equal energy per mode and that the flow speed can be neglected, there exists a simple expression for the high-ka far-field radiation pattern. This result can then be used to derive a high-ka approximation for the beamformer output in an equal energy per mode sound field by showing first that this sound field is equivalent to a semi-isotropic noise field, for which a simple expression for $|b(\phi,\omega)|^2$ exists. Combining the two results gives a high-ka approximation to $|H(\phi,\omega)|^2$.

Following Joseph and Morfey [59] the far-field radiation from an unflanged duct containing an equal energy per mode sound field in the limit as ka tends to infinity is

$$|p_f(\phi,\omega)|^2 = \frac{2\rho c W}{\pi R^2}\cos\phi \qquad (ka \to \infty) \tag{4.23}$$

where R is the observer distance from the centre of the duct face and W is the total radiated sound power.

We now consider the in-duct beamformer output for an equal-energy-per-mode sound field. We will make use of a concept widely used in SONAR theory called the *Array Gain* of a phased array that quantifies the level of noise rejection by an array. It is defined as the ratio of the noise power of an omnidirectional sensor to the noise power output detected by the beamformer at a particular beam-steer angle. Applied to the present problem it may be written as,

$$\mathrm{AG}(\phi) = \frac{|p_w(\omega)|^2}{|b(\phi,\omega)|^2} = \frac{\sum_{mn}|p_w(\phi_{mn},\omega)|^2}{\sum_{mn}|p_w(\phi_{mn},\omega)|^2|T(\phi_{mn},\phi)|^2} \tag{4.24}$$

Noting that the mean-square pressure at the wall of the duct is approximately twice that averaged over the duct cross-section [58], and replacing the summation over (m,n) by an integral over ϕ, a high frequency approximation for the squared pressure at the duct wall is of the form

$$\sum_{mn}|p_w(\phi_{mn},\omega)|^2 \to 2N(ka)\int_0^{\pi/2}|A(\phi)^{\mathrm{ee}}|^2\, n(\phi)d\phi \qquad (ka \to \infty) \tag{4.25}$$

where $N(ka)$ is the total number of propagating modes at a frequency ka and $n(\phi)$ is the modal density function, which specifies the number of modes, $N(\phi)$ per unit propagation angle $\delta\phi$,

$$n(\phi) = \frac{1}{N(ka)}\frac{N(\phi) - N(\phi - \delta\phi)}{\delta\phi} \tag{4.26}$$

It may be shown using the modal density function due to Rice[60] expressed in terms of the cutoff ratio, that $n(\phi) = 2\cos\phi\sin\phi$. Noting that at high ka, $N(ka) \approx (\frac{1}{2}ka)^2$ (*ibid*), inserting equation (4.18) into (4.25) leads to a simple expression for the squared pressure at the duct wall of the form

$$\sum_{mn}|p_w(\phi_{mn},\omega)|^2 \to 2(ka)^2\frac{\rho c\varpi}{\mathcal{S}} \qquad (ka \to \infty) \tag{4.27}$$

where $\mathcal{S}$ is the duct cross-sectional area πa^2.

In Appendix D we demonstrate that an equal energy per mode sound field, in the high-ka limit, tends to a semi-isotropic sound field, in which the mean square pressure arriving per unit solid angle over a hemisphere is constant. The array gain for a line array of N sensors separated by a distance Δz, and steered at an angle ϕ in a semi-isotropic noise

field is given by[44],

$$\mathrm{AG}(\phi) = \frac{N^2}{2N + 4\sum_{l=1}^{N}(N-l)\cos(2\pi l \Delta z \cos\phi/\lambda)\mathrm{sinc}(2l\Delta z/\lambda)} \tag{4.28}$$

Here we have assumed that the array gain for a line array in a semi-isotropic noise field is half that in a fully isotropic noise field, since the noise due to a single sensor in the former case is half that in the latter, while the beamformed noise is largely the same in both cases. Substituting equations (4.27) and (4.28) into equation (4.24) gives,

$$|b(\phi,\omega)|^2 = \frac{2(ka)^2}{\mathrm{AG}(\phi)}\frac{\rho c \varpi}{\mathcal{S}} \qquad (ka \to \infty) \tag{4.29}$$

Finally, combining equations (4.29) and (4.23) and noting that for the case of equal energy per mode $W/\varpi \to (\frac{1}{2}ka)^2$ as $ka \to \infty$,

$$2\left(\frac{R}{a}\right)^2 \mathrm{AG}(\phi)|H(\phi,\omega)|^2 \to \cos\phi \qquad (ka \to \infty) \tag{4.30}$$

Note that for $\Delta z = \lambda/2$ in equation (4.28) the array gain $\mathrm{AG}(\phi) = \frac{1}{2}N$. In this case equation (4.29) simplifies to,

$$|b(\phi,\omega)|^2 = \frac{4(ka)^2\rho c\varpi}{N\mathcal{S}} \qquad (\Delta z = \lambda/2, \quad ka \to \infty) \tag{4.31}$$

and therefore,

$$\frac{8}{N}\left(\frac{R}{a}\right)^2 |H(\phi,\omega)|^2 \to \cos\phi \qquad (ka \to \infty) \tag{4.32}$$

Equation (4.32) is plotted in figure 4.6, and is seen to be in very close agreement with the exact calculation of $|H(\phi,\omega)|^2$ from equation (4.16).

4.3.7 Comparison of in-duct and ideal array gain

Figure 4.7 is a comparison of the array gain for a line array in a semi-isotropic noise field as predicted by equation (4.28), with the theoretical expression for a linear array at the duct wall versus frequency as predicted by equation (4.24) for an array of 11 sensors. The frequency axis is normalised to the reference frequency $ka_0 = 20$ at which $\Delta z = \lambda/2$. In general, good agreement between the ideal (dashed) curve and the in-duct Array Gain (solid curve) is observed. As frequency increases the Array Gain tends to a value of $10\log_{10}(N/2)$ (thin solid curve), except at $\phi_b = 0$ where the exact array gain is around 1dB less than the ideal array gain, attributable to the end-fire effect described in section 4.3.2. For a beam-steer angle of $\phi_b = 90°$ (broadside), the agreement with the ideal Array Gain is less close. The exact array gain fluctuates significantly, this can

be attributed to the fact that only a few modes have mode-ray angles close to 90° and hence the semi-isotropic assumption is less valid for angles close to broadside. At 45°, where the mode density is the highest, and the sound field is at its "most isotropic", the agreement is closest.

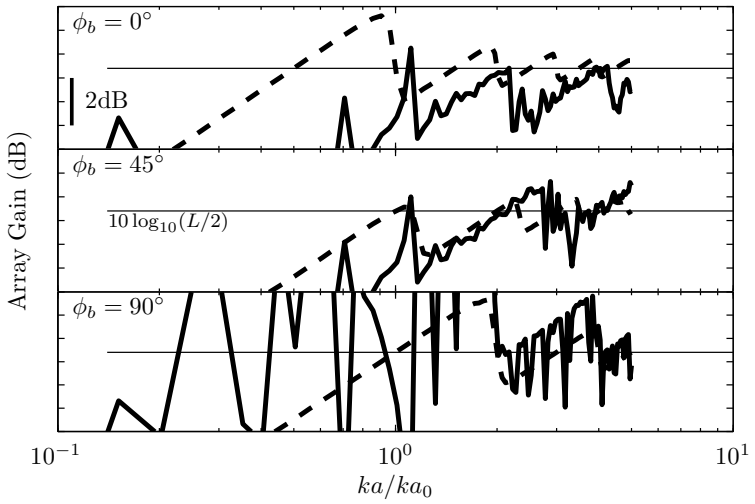

FIGURE 4.7: A comparison of array gain for a line array in a semi-isotropic noise field as predicted by equation (4.28) with that of a linear array at the duct wall as predicted by equation (4.24). Calculated for an array of 11 sensors as a function of frequency, where $ka_0 = 20$ is the frequency at which $\Delta z = \lambda/2$. From top to bottom the beam-steer angle is $\phi_b = 0°$ (endfire), $\phi_b = 45°$ and $\phi_b = 90°$ (broadside)

4.3.8 Estimation of mode amplitude distribution from $|b(\phi,\omega)|^2$

In this section we investigate the use of the beamformer for estimating the distribution of amplitude with propagation angle ϕ. We demonstrate that small variations in mode amplitude distribution are detected in the beamformer output, which can then be used to deduce corresponding changes in the far-field directivity.

In equation (4.13) the beamformer output is formulated as a convolution of the pressure measured at the duct wall, $|p_w(\phi_{mn},\omega)|^2$, with the beamformer response function. At high-ka the squared pressure at the duct wall is approximately twice that averaged over the duct cross section. Assuming that the variation of $|A(\phi_{mn})|^2$ within the beamwidth is small, the variation of $|A(\phi_{mn})|^2$ can be removed from the integral in equation (4.25), and the integral can be confined to the beamwidth of the array,

$$|b(\phi,\omega)|^2 \approx 2N(ka)|A(\phi_{mn})|^2 \int_{\phi-\Delta\phi}^{\phi+\Delta\phi} n(\phi)\, d\phi \tag{4.33}$$

where the integral over ϕ specifies the number of modes in the beamwidth $2\Delta\phi$ divided by the total number of modes. Noting that for a cylindrical duct $n(\phi) = \sin 2\phi$ (Rice [60]), and performing the integration allows the estimation of the squared mode amplitude

averaged over a beamwidth

$$|A(\phi)|^2 \approx \frac{|b(\phi,\omega)|^2}{N(ka)\,[2\sin 2\phi \sin 2\Delta\phi]} \tag{4.34}$$

Angles $\phi - \Delta\phi$ less than zero correspond to part of the mainlobe being outside of the duct, and ϕ is taken to be zero. The variation of mode amplitude with ϕ calculated by the approximation in equation (4.34) is plotted in figure 4.8 a for an equal-energy-per-mode sound field with unit power per mode at $ka = 20$. Also shown is the exact distribution (crosses). The beamformer has 21 equally spaced sensors $\Delta z = \lambda/2$ apart. Figure 4.8 b shows a comparison between the estimated and an exact mode amplitude distribution that varies with ϕ on a scale larger than a beamwidth. Figure 4.8 c is the corresponding result when $|A(\phi)|$ varies on a scale roughly equal to a beamwidth. The beamwidth in the simulations varies from approximately 20° at $\phi = 0$, to approximately 6° at $\phi = 90$.

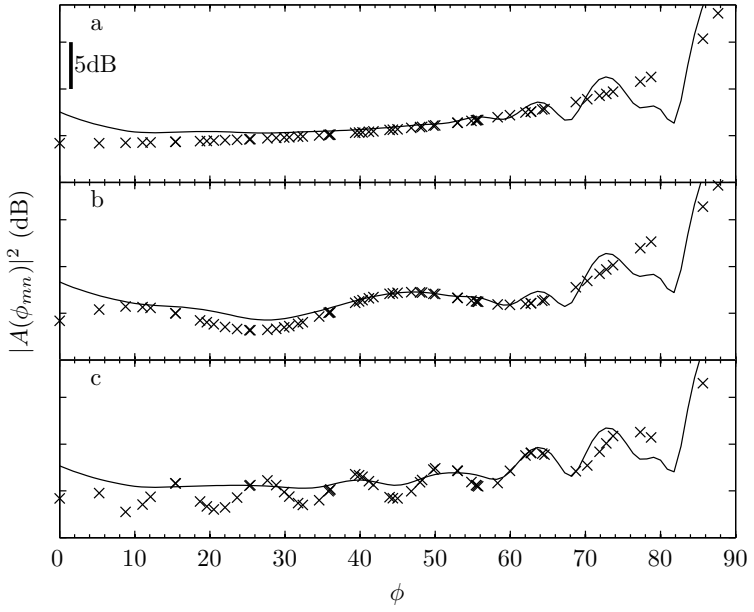

FIGURE 4.8: A comparison of the true mode amplitudes (crosses) and the approximation calculated from the beamformer response function using equation (4.34) at $ka = 20$ with an array of 21 sensors spaced $\Delta z = \lambda/2$. The top plot is for an equal energy per mode sound field, the middle plot has $|A(\phi_{mn})|^2$ varying on a scale larger than a beamwidth and the lower plot has $|A(\phi_{mn})|^2$ varying on a scale approximately equal to a beamwidth.

In figure 4.8 the error between the actual and estimated mode amplitude distribution is smallest in the range of propagation angles between 20° to 70°. At low beam-steer angles the difference between the actual and estimated mode amplitudes is larger although the error is still only of the order $3dB$ at 0°. This error can be attributed to the "end-fire" effect mentioned above, where the mainlobe of the beam lays partly outside the duct. With the mode amplitude distribution that varies on a scale larger than a beamwidth, figure 4.8 b, the measurement obtained using the in-duct beamformer captures the main variation of the distribution especially in the angle range 20° to 70°. When the variation

of mode amplitude is on a scale equal to or smaller than the beamwidth, the beamformer is not able to follow all of the details of the variation, especially at beam-steer angles close to endfire. However an "average" modal distribution is captured, and increasing the length of the array (thereby reducing the beamwidth), would improve resolution of the mode amplitude variation.

4.3.9 Sound power estimation using the in-duct beamformer

In this section we investigate the use of the beamformer measurement for the determination of radiated sound power. The radiated sound power can be inferred from measurements of the far-field intensity by integrating over a surface enclosing the duct exit. For axi-symmetric radiation, confined to angles $0 \leq \phi \leq \frac{\pi}{2}$,

$$W(\omega) = \frac{2\pi R^2}{\rho c} \int_0^{\pi/2} |p_f(\phi, \omega)|^2 \sin\phi \, d\phi \tag{4.35}$$

The far-field radiated pressure, $|p_f(\phi, \omega)|^2$, can be estimated from the transfer function, $|H(\phi, \omega)|^2$, derived earlier. Substituting equation (4.1) and the approximation to $|H(\phi, \omega)|^2$ from equation (4.32) into equation (4.35) gives an expression for the radiated sound power in terms of the in-duct beamformer measurements,

$$W(\omega) = \frac{\mathcal{S}N}{8\rho c} \int_0^{\pi/2} |b(\phi, \omega)|^2 \sin 2\phi \, d\phi \tag{4.36}$$

In equation (4.36) we assume that there are no reflections from the open end of the duct, and that the energy propagating in the mode-ray angles from 0 to $\pi/2$ is radiated to the far-field. In the case where reflections can be considered important equation (4.36) can be modified by subtracting the reflected sound power from the power flowing towards the open end,

$$W(\omega) = W_{\text{incident}} - W_{\text{reflected}} = \frac{\mathcal{S}N}{8\rho c} \left(\int_0^{\pi/2} |b(\phi, \omega)|^2 \sin 2\phi \, d\phi - \int_{\pi/2}^{\pi} |b(\phi, \omega)|^2 \sin 2\phi \, d\phi \right) \tag{4.37}$$

Figure 4.9 is a plot of the beamformer output between 0° and 180° for an equal energy per mode sound field using an array of N sensors separated axially by $\lambda/2$, with N chosen such that the array length L_z varies from 2λ to 50λ. The frequency is $ka = 20$ and reflections from the open end are assumed to be completely absent. The beamformer output in the range of beam-steer angles from 90° to 180° is due to the presence of sidelobes pointing upstream. The output in this range of angles is approximately 10dB lower than the maximum output. This implies that equation (4.37) can be used to separate incident and reflected sound power if the difference between them is less than approximately 10dB, that is when the intensity reflection coefficient is greater than 0.1. It

may be possible to improve on this by choosing beamformer weights (known as "shading") that increase side-lobe rejection, at the expense of increased main-lobe width. This is beyond the scope of the current work, but in-depth coverage is available, for example, by Burdic [44].

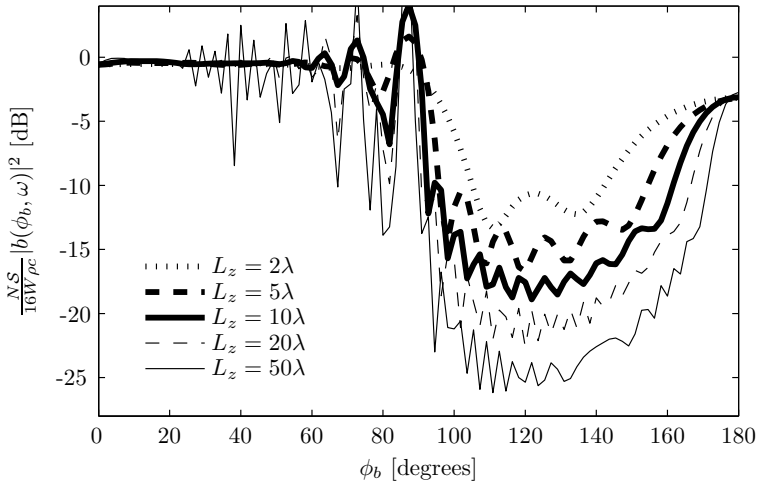

FIGURE 4.9: Beamformer output as a function of beam-steer angle ϕ_b for an equal energy per mode sound field using arrays of varying length L_z with sensors separated axially by $\lambda/2$ at $ka = 20$.

In the case where the microphones separation distance $\Delta z = \lambda/2$, and the noise field is perfectly isotropic, the pressure at the wall at each of the individual sensors is uncorrelated (see for example Burdic [44]). The beamformer output is then simply,

$$|b(\phi,\omega)|^2 = \frac{1}{N^2}\Big[\,|p_w(\omega)|^2\,N\Big] \tag{4.38}$$

Substituting equation (4.38) into equation (4.36) gives

$$W(\omega) = \frac{\mathcal{S}|p_w(\omega)|^2}{4\rho c} \tag{4.39}$$

This result is identical to that obtained by Joseph *et al.*[58] for the determination of radiated sound power from measurements of pressure at the duct wall for an equal energy per mode sound field.

Having established some basic physical principles using a simplified no-flow model we now consider application of the technique to more realistic engine inlets and exhausts. We first compute $|H(\phi,\omega)|^2$ for an aeroengine inlet, then for an annular exhaust duct where there are two flow streams.

4.4 Estimation of sound-radiation from aeroengine inlets

To investigate the usefulness of the in-duct to far-field technique for an aeroengine inlet we introduce the effect of a uniform mean flow, $M > 0$, in the equations for the beamformer output (4.11) and the radiated sound field (4.7). For simplicity we assume that the flow speed is the same everywhere, both inside and outside of the duct. This calculation neglects the effect of non-uniform flow profiles and complex inlet geometries. Note however that some of these effects could be modelled using a more accurate radiation model in place of the Kirchoff solution given by equation (4.7). Examples of more sophisticated models are those that modify the Kirchoff solution to account for other geometries, such as bell-mouth inlets [61], or the use of numerical modelling software such as ACTRAN [62].

The beamformer output versus angle for the equal-energy-per-mode case for various flow speeds is shown in figure 4.10. The in-duct microphone array consists of 11 sensors spaced $\Delta\bar{\bar{z}} = \lambda/2$ apart. For all flow speeds the beamformer output varies by no more than ± 0.5dB with ϕ below 60°.

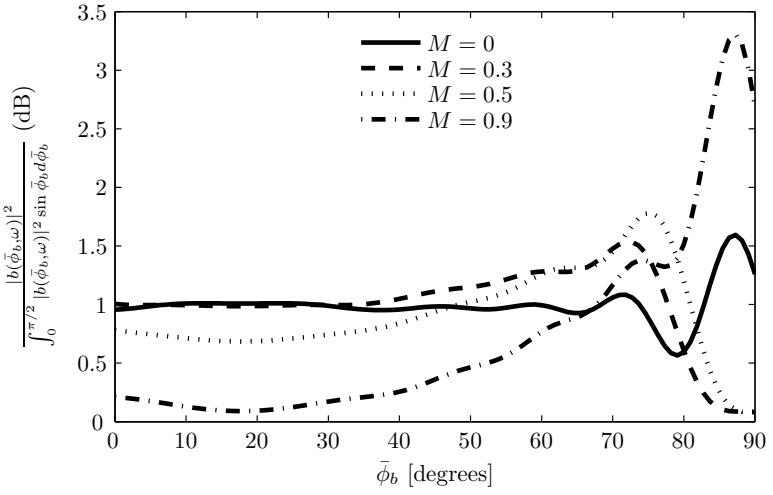

FIGURE 4.10: Beamformer output as a function of beam-steer angle $\bar{\phi}$ for flow speeds $M = 0$, $M = 0.3$, $M = 0.5$ and $M = 0.9$ at $ka = 20$ for an array of 11 sensors spaced $\Delta z = \lambda/2$ apart.

The corresponding far-field directivity is plotted in figure 4.11. It shows a stronger dependence on flow speed than the beamformer output. As the flow speed increases the radiation becomes increasingly more directional towards 90°.

Figure 4.12 is a plot of the corresponding $|H(\bar{\phi},\omega)|^2$ at $ka = 20$, with the addition of curves for the volume velocity and equal amplitude sources. Note that, as for the $M = 0$ case in figure 4.6, $|H(\bar{\phi},\omega)|^2$ is insensitive to the chosen mode amplitude distribution for flow speeds below $M = 0.7$. Above this flow speed $|H(\bar{\phi},\omega)|^2$ becomes more sensitive to mode amplitude distribution, with the volume-velocity model in particular showing large deviations from the other models. As in the no-flow case this sensitivity can be explained

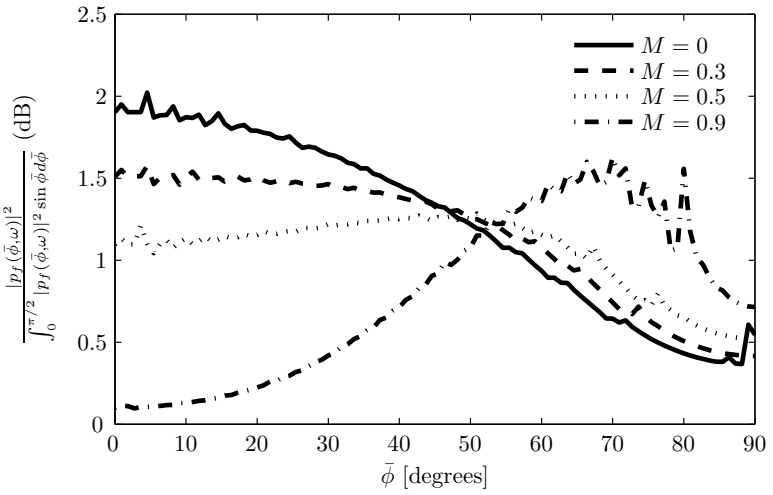

FIGURE 4.11: Far-field directivity as a function of angle $\bar{\phi}$ for flow speeds $M = 0$, $M = 0.3$, $M = 0.5$ and $M = 0.9$ at $ka = 20$.

by noting that the amplitude of modes close to cut-on approaches infinity rapidly in the volume velocity model, for angles close to 90° in equation (4.19). This effect is increased for $M > 0$ as M appears as a fourth power in equation (4.19).

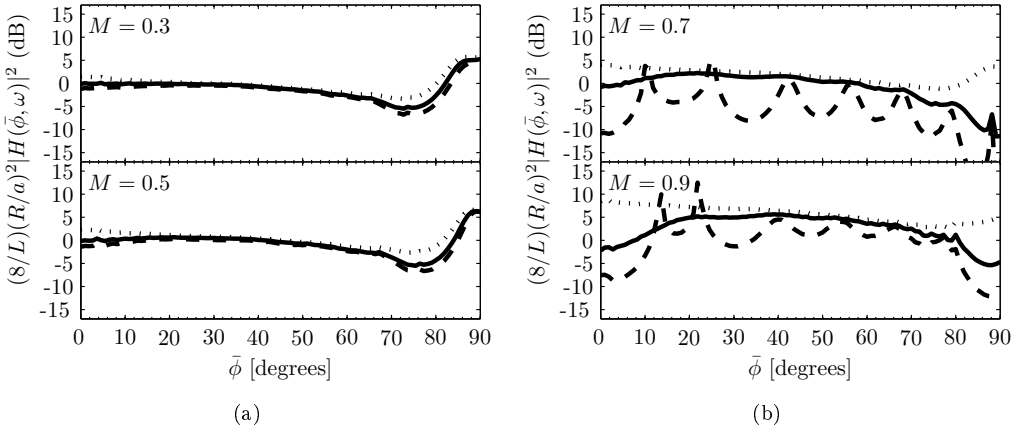

FIGURE 4.12: Normalised in-duct to far-field transfer function for equal amplitude (dotted), volume-velocity (dashed) and equal energy (solid) mode amplitude distributions as a function of angle $\bar{\phi}$. The in-duct microphone array consists of 11 sensors spaced $\Delta z = \lambda/2$ apart at a frequency $ka = 20$.

The effects of a uniform flow in the duct does not have a significant negative impact on the robustness of the transfer function, in terms of its sensitivity to mode amplitude distribution. At all but the lowest flow speeds the full transfer function must be calculated; one cannot use the $\cos(\bar{\phi})$ high-ka approximation of equation (4.32). This is not a significant disadvantage, as the transfer function prediction is computationally inexpensive using the analytical formulations provided earlier, and can be performed "off-line" if rapid far-field predictions are required.

We now consider the application of the technique to the prediction of far-field directivity from an aeroengine exhaust duct.

4.5 Estimation of sound-radiation from aeroengine exhausts

In this section we consider the use of the in-duct beamformer technique to predict the sound radiation from an aeroengine exhaust. The exhaust is modelled as a hard-walled annular duct with a hub-to-tip ratio (the ratio of the inner radius, R_1, to the outer radius, R_0) of 0.8. The calculation of the in-duct beamformer output proceeds as before for the cylindrical duct with the substitution of annular mode shape functions Ψ in equation (4.2). The annular mode shape functions used in the simulations are given in appendix A.

The radiation calculation is considerably more difficult than the no-flow and inlet cases presented above, due to the presence of two flow streams. One is the flow from the jet the other is the surrounding mean-flow. In this section we use Gabard and Astley's [63] solution for the radiation from an unflanged annular duct with an infinite centre body. The basic arrangement is shown in figure 4.13.

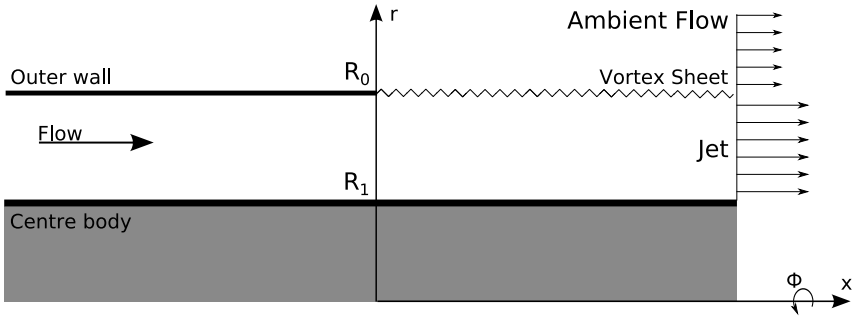

FIGURE 4.13: Annular duct sketch

This model, an extension of Munt's solution [64], provides an exact solution for the sound field radiated by a single duct mode from an un-flanged annular duct with a hard centre-body. Diffraction through the semi-infinite vortex sheet which separates the annular jet stream from the ambient external flow is included. The model has been successfully validated against no-flow experimental and numerical data by Sugimoto and Astley [65].

The flow-speeds used for the calculation are summarised in table 4.1. These correspond to those typically used in flight tests for the measurement of the noise levels at the three flight conditions defined in the ICAO noise certification. Figures 4.14 through 4.18 show the beamformer output, far-field directivity and transfer function for each flight condition in table 4.1.

Figures 4.14 a,b, and c are plots of the beamformer output, far-field directivity and transfer function respectively for a no-flow annular duct at $ka = 20$. An array of 11

Flight Condition	Exterior Mach Number (M_1)	Jet Mach Number (M_2)
Zero-flow	0	0
Approach	0.219	0.447
Cutback	0.269	0.737
Sideline	0.265	0.861

TABLE 4.1: Parameters used for exhaust simulations.

microphones spaced $\Delta\bar{\bar{z}} = \lambda/2$ apart was used for the in-duct beamformer. The figure shows curves for equal amplitude, equal energy and volume velocity mode amplitude distributions.

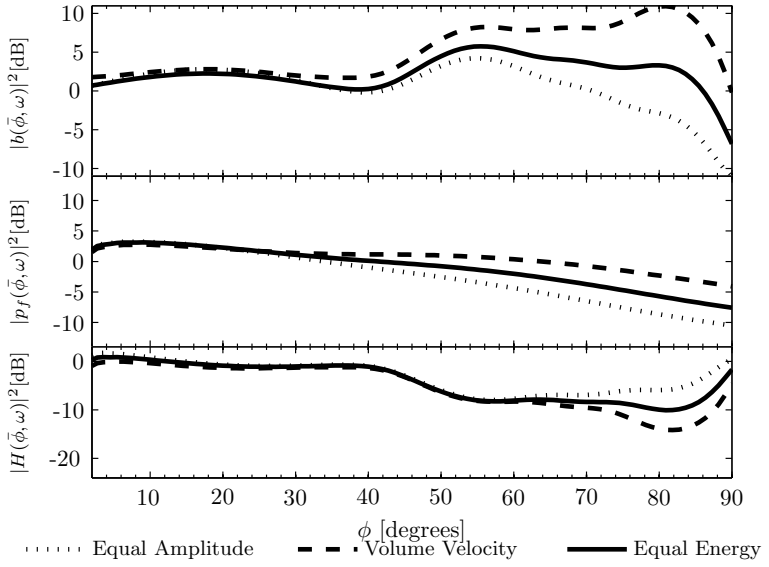

FIGURE 4.14: Beamformer output (top), far-field radiation (middle) and transfer function (bottom) for the zero-flow exhaust configuration. Three different mode-models are shown, the frequency of calculation is $ka = 20$.

For the equal energy case the beamformer output is weakly dependent on beam-steer angle, for angles below $\phi = 40°$. The increase in beamformer output at around 50° can be attributed to an increased density of modes at this angle. To explain this, figure 4.15 is a plot of the mode density normalised by the number of propagating modes $n(\phi)/N(ka)$ as a function of mode-ray angle ϕ, for a annular duct of hub-tip ratio $h = 0.8$. For comparision the same quantity is plotted for a cylindrical duct.

Note that at $ka = 20$ (figure 4.15(a)) there is a high density of modes close to the mode-ray angle 50°. This corresponds to the region where beamformer output increases in figure 4.16, and is related to the clustering of eigenvalues at this angle and frequency for the annular duct. At $ka = 200$, shown in figure 4.15(b), the difference in mode denisty as a function of mode ray angle between the cylindrical and annular ducts is much less. The approximation $n(\phi) \approx \sin 2\phi$ is valid for both cylindrical and annular ducts in the high-ka limit.

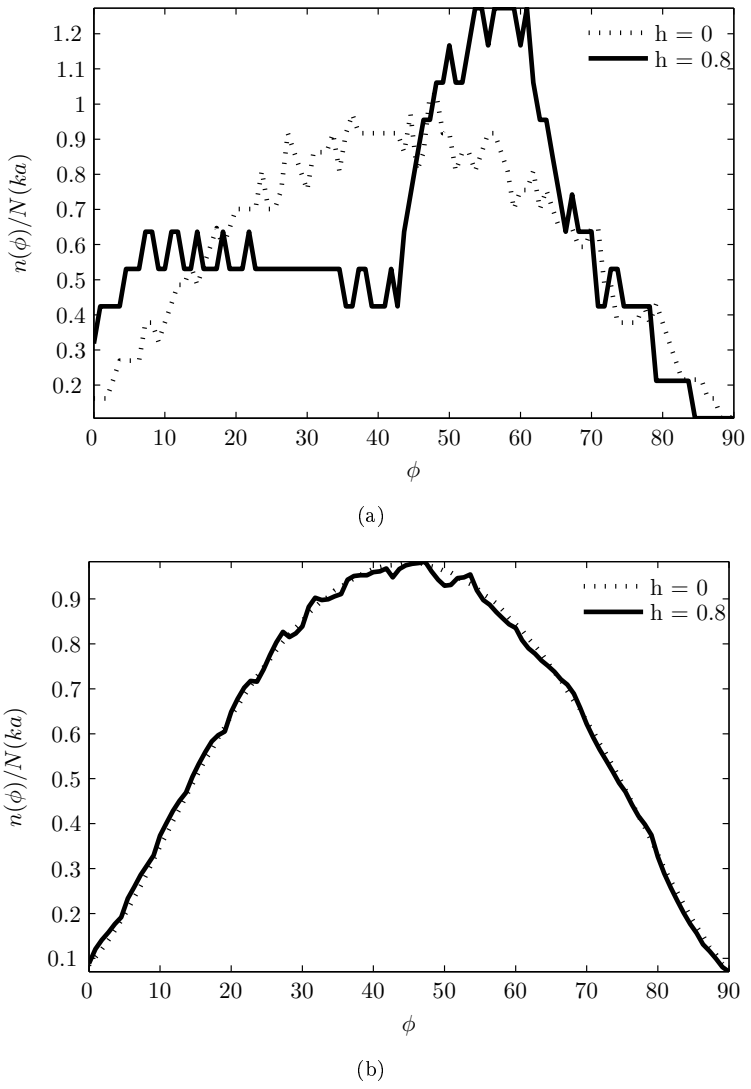

FIGURE 4.15: A plot of the mode density $n(\phi)$ normalised by the number of propagating modes $N(ka)$ for a cylindrical duct, and an annular duct of hub-tip ratio 0.8. The top figure is the numerically calculated mode density at $ka = 20$, the bottom at $ka = 200$.

The transfer function is largely insensitive to the chosen mode amplitude distribution up to approximately 70°. This is in agreement with the no-flow cylindrical results in section 4.3.5.

The introduction of flow, starting in figure 4.16 for the approach case introduces some additional features compared to the zero-flow case. The radiation is weak in the range of angles between 0° (on axis) and approximately 40° (peak radiation angle). This region is known as the "cone of silence", and corresponds to angles below the "critical angle" where total internal reflection takes places as the ray moves passes from the jet to the surrounding flow region. This effect is analogous to Snell's Law for light passing through an interface between two materials of differing refractive indexes. Sound is only able to enter the cone of silence by diffraction of the rays. This effect is discussed in more detail

by Goldstein [48]. The critical angle, ϕ_c, is defined as

$$\phi_c = \cos^{-1} \frac{1}{1 + (M_2 - M_1)} \tag{4.40}$$

Equation (4.40) predicts peak radiation angles of 35°, 47° and 51° for the approach, cutback and sideline cases respectively. This is in good agreement with the peak radiation angles in plots 4.16 to 4.18, although the agreement worsens as M_2 increases. Note that the simple geometric interpretation of equation (4.40), unlike the Gabard and Astley model, does not take into account diffraction into the cone of silence.

Since all three plots, figures 4.16c, 4.17c and 4.18c show a weak dependence of $|H(\phi, \omega)|^2$ on mode amplitude distribution, the technique is therefore applicable to these exhaust cases, and would also allow, for example, the effect of different flight speeds to be predicted from static engine-rig experiments.

For all of the flight conditions investigated, the transfer function is insensitive to the mode amplitude distribution for angles below approximately 60°. For the very high flow speed sideline case (figure 4.18) there is some sensitivity to the mode amplitude distribution for angles above 60°. In the approach and cutback cases, these differences are quite small except for angles very close to broadside.

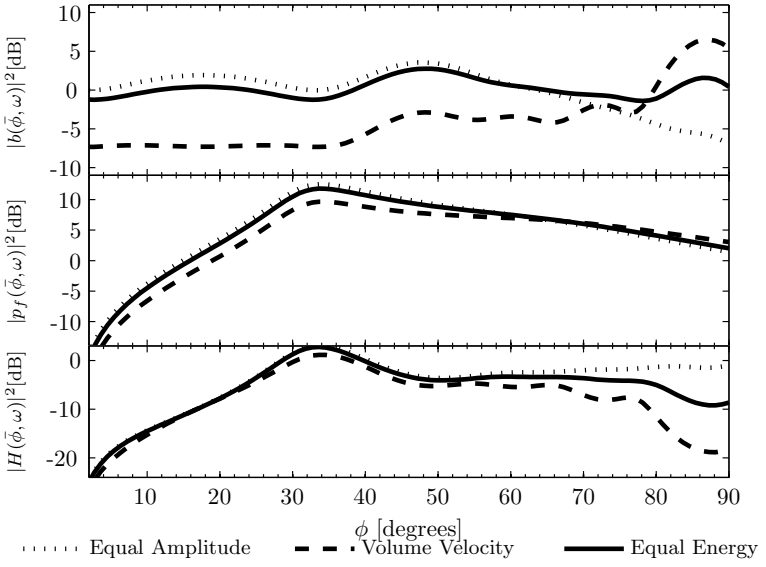

FIGURE 4.16: Beamformer output (top), far-field radiation (middle) and transfer function (bottom) for the approach exhaust configuration. Three different mode-models are shown, the frequency of calculation is $ka = 20$.

4.6 Conclusion

A phased array measurement technique has been proposed that uses an axial array of microphones in the duct to predict sound field radiated from the open end of the

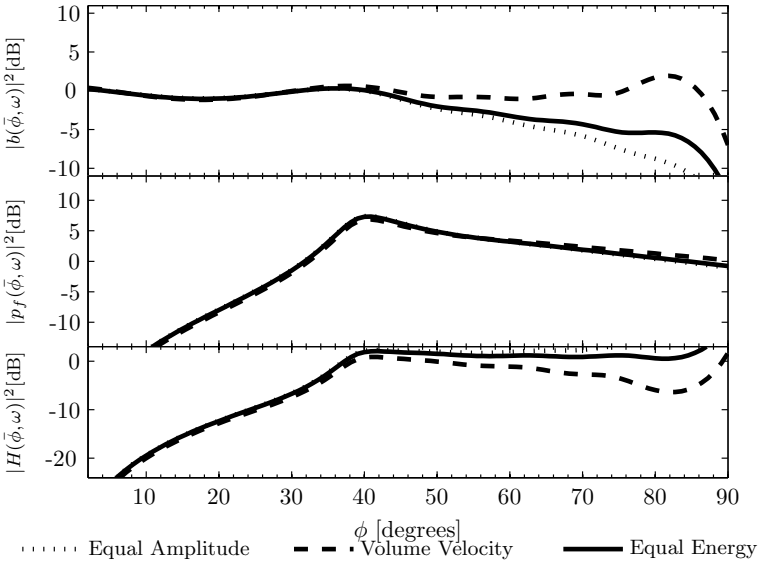

FIGURE 4.17: Beamformer output (top), far-field radiation (middle) and transfer function (bottom) for the cutback exhaust configuration. Three different mode-models are shown, the frequency of calculation is $ka = 20$.

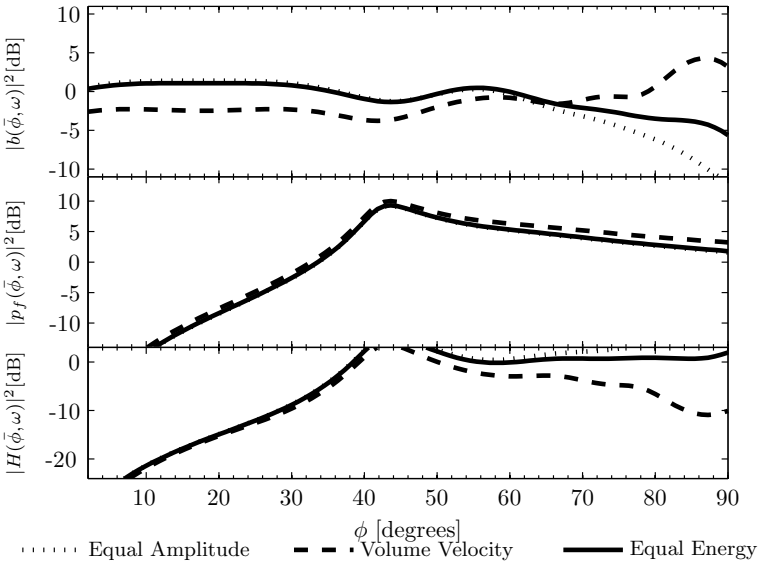

FIGURE 4.18: Beamformer output (top), far-field radiation (middle) and transfer function (bottom) for the sideline exhaust configuration. Three different mode-models are shown, the frequency of calculation is $ka = 20$.

duct. We have shown that the transfer function used to relate the in-duct beamformer output as a function of angle, to the corresponding radiated far-field directivity pattern is independent of the mode amplitude distribution in the duct.

The transfer function for a no-flow duct has been fully investigated, and a numerical transfer function for aeroengine inlet and exhaust ducts has been proposed.

The principle advantage of this technique, over, for example determining the mode amplitudes present by modal decomposition and using these as the input to a radiation model, is the relatively small number of microphones required. An array of around 10 microphones spaced half a wavelength apart is sufficient to predict the far-field directivity pattern. The transfer functions required could easily be calculated in advance of a measurement campaign. This would allow rapid prediction of far-field directivity, and give a first indication of the effect of build changes on the radiated sound.

In the next chapter the technique presented here is validated using a laboratory-scale no-flow experiment.

Chapter 5

Experimental validation of the in-duct to far-field technique

5.1 Introduction

This chapter presents an experimental verification of the in-duct to far-field measurement technique developed in chapter 4. The main aim of the experiment was to verify the no-flow results of chapter 4, in particular the estimation of far-field directivity using an in-duct axial microphone array.

5.2 Method

Figure 5.1 is a schematic of the experimental set-up. The experiment was performed in the large anechoic chamber and adjoining reverberation chamber at the ISVR. A 4.8 m hard-walled, steel duct of internal diameter 0.4 m was passed through the wall separating the anechoic and reverberation chambers. A thick panel was constructed to hold the duct and ensure good acoustic isolation of the two chambers.

A broadband noise field was created in the duct using a pair of loudspeakers located in the reverberation room, Both the in-duct acoustic pressure and the far-field acoustic pressure were measured simultaneously. The in-duct acoustic pressure was measured using an axial array of 15 microphones mounted at the duct wall, and to cross-check the axial array measurements also with an azimuthal ring of 30 microphones close to the open end of the duct. The far-field pressure was measured with an arc of 19 microphones in the anechoic chamber positioned every 5° from 0° to 90° at a distance of 3.45 m from the open end of the duct.

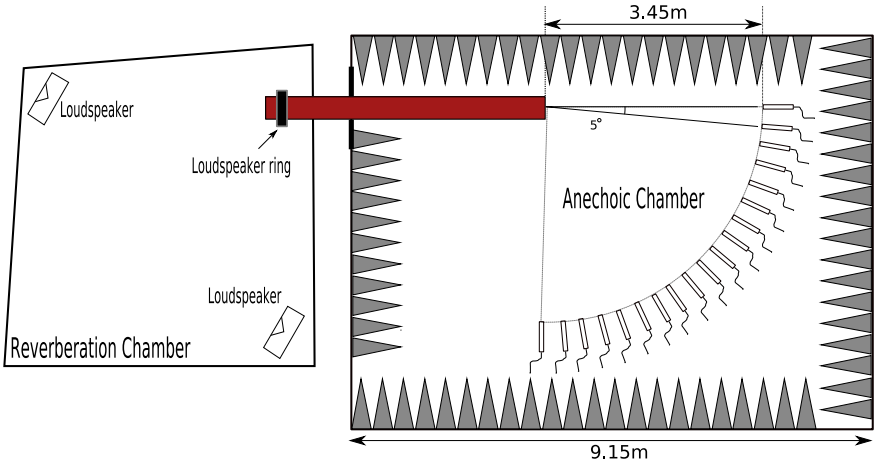

FIGURE 5.1: A plan-view schematic of the experimental set-up. The reverberation chamber is connected to the anechoic chamber by a 4.8 m steel duct. Noise is generated either by two loudspeakers or a ring of loudspeakers at the duct wall. In the anechoic chamber, the 19 far-field microphone positions trace a circular arc of radius 3.45 m, spaced 5° apart, from 0° (on axis) to 90°.

5.2.1 Reverberation Chamber

Broadband noise was generated in the duct using two Electro-voice 400 W loudspeakers driven by mutually incoherent white noise signals via two power-amplifiers. The white noise signals were pre-generated, pseudo-random sequences produced using MATLAB and stored onto 2 channels of a 24 channel Alesis-ADAT hard-disk recorder.

The reverberation room has nonparallel, highly reflective walls and a volume of 131 m^3. This ensures that the sound field in the room, and hence the sound-field incident on the open end of the duct, is reasonably diffuse. Joseph *et al.* [58] have shown that this form of excitation creates an *equal energy per mode* sound-field inside the duct, and ensures that all propagating modes are mutually incoherent. Incoherent modes is one of the main assumptions in the in-duct to far-field technique.

5.2.2 In-duct measurements

Figure 5.2 is a photograph of the in-duct microphone array. Fifteen 7 mm electret microphones were mounted on a thin plate of size 50 mm by 400 mm. The microphones were positioned at the edge of the plate, with the centre of the microphone capsules separated 25 mm apart. This spacing corresponds to $\lambda/2$ at $ka = 25$ (assuming a sound speed of 340 ms^{-1}), and is the maximum frequency at which the array can be used before aliasing occurs. The microphone cables passed through small holes in the plate, and were affixed to the underside of the plate so as to minimise their effect on the sound field in the duct.

FIGURE 5.2: A photograph of the in-duct microphone array. Fifteen 7 mm electret microphones were mounted on a thin 50 mm by 400 mm aluminium plate. The microphones were positioned at the edge of the plate, with the centre of the capsules 25 mm apart.

FIGURE 5.3: A photograph of the microphone array positioned in the duct. The microphones themselves lay on an axial line, and are as close as possible to the duct wall.

The microphone array was located along the bottom of the duct, and as close as possible to the duct wall (figure 5.3). The first microphone in the array was positioned 1.2 m from the open end of the duct, so as to minimise the effect of reflections from the open end.

Each microphone was connected to a custom-made signal amplifier. The time series were sampled simultaneously using a 32 channel SONY DAT recorder at a sampling rate of 48kHz with 16 bit resolution. The total recording time for each test was 1 min.

The array data was post-processed to create a cross-spectral matrix at each discrete frequency point using the MATLAB Signal Processing Toolbox functions `cpsd` and `pwelch`. A Welch spectral estimation algorithm was used (2048 point FFT, Hamming window and 50% overlap).

To account for the differences in magnitude and phase of the individual array microphones, calibration was performed by multiplying the complex pressure spectrum of the

i^{th} microphone $p_i(\omega)$ by a transfer function, $G_{iR}(\omega)$. The transfer function $G_{iR}(\omega)$ is the transfer function between the i^{th} array microphone and a reference microphone averaged over four loudspeaker positions. This transfer function was measured in an anechoic chamber by placing a B&K type 4185 microphone 5 mm away from the diaphragm of each of the array microphones in turn. White noise was generated with a loudspeaker, and the transfer function between the two microphones was measured.

The cross-spectral matrix, $\mathbf{S}_{pp}$, in each frequency bin was formed from,

$$\mathbf{S}_{pp} = \begin{bmatrix} |G_{1R}|^2 S_{p_1p_1} & G_{1R}S_{p_1p_2}G_{2R}^* & \dots & G_{1R}S_{p_1p_N}G_{NR}^* \\ G_{2R}S_{p_2p_1}G_{1R}^* & |G_{2R}|^2 S_{p_2p_2} & & \\ \vdots & \vdots & \ddots & \\ G_{NR}S_{p_Np_1} & & & |G_{NR}|^2 S_{p_Np_N} \end{bmatrix} \tag{5.1}$$

where $S_{p_ip_j} = E\{\frac{\pi}{T}p_i(\omega)p_j^*(\omega)\}$ is the pressure cross spectral density between microphone i and microphone j.

Following the theory presented in section 4.2.3 the beamformer output corresponding to a beamsteer angle ϕ, is,

$$S_{bb}(\phi,\omega) = \frac{1}{N^2}\mathbf{w}(\phi,\omega)\mathbf{S}_{pp}\mathbf{w}^H(\phi,\omega) \tag{5.2}$$

where $\mathbf{w}$ is the vector of weight coefficients, calculated from equation (4.10). Note equation (5.2) is simply a restatement of equation (4.9) in matrix form, with the measured cross-spectral matrix replacing the predicted pressures of equation (4.9).

In addition to the axial microphone array, an azimuthal ring of 30 electret microphones, of the same type used in the axial array, was also present in the duct. The microphones were equally spaced in 12° increments at a distance of 60 cm from the open-end of the duct closest to the reverberation room, as shown in figure 5.4. The microphones were calibrated in the same manner as those in the axial array. Their time signals were acquired simultaneously using the same hardware as the in-duct axial array.

5.2.3 Far-field measurements

Measurements of the far-field directivity were made in the anechoic chamber. The size of the chamber, not including wedges, is 7.33 m x 7.33 m x 5.50 m. The cutoff frequency of the wedges is 80 Hz[1]. The mesh floor of the chamber was removed to minimise reflections. Figure 5.5 is a photograph of the anechoic chamber taken from the main entrance showing the duct and the far-field array.

[1] `http://www.isvr.co.uk/faciliti/lg_anech.htm`

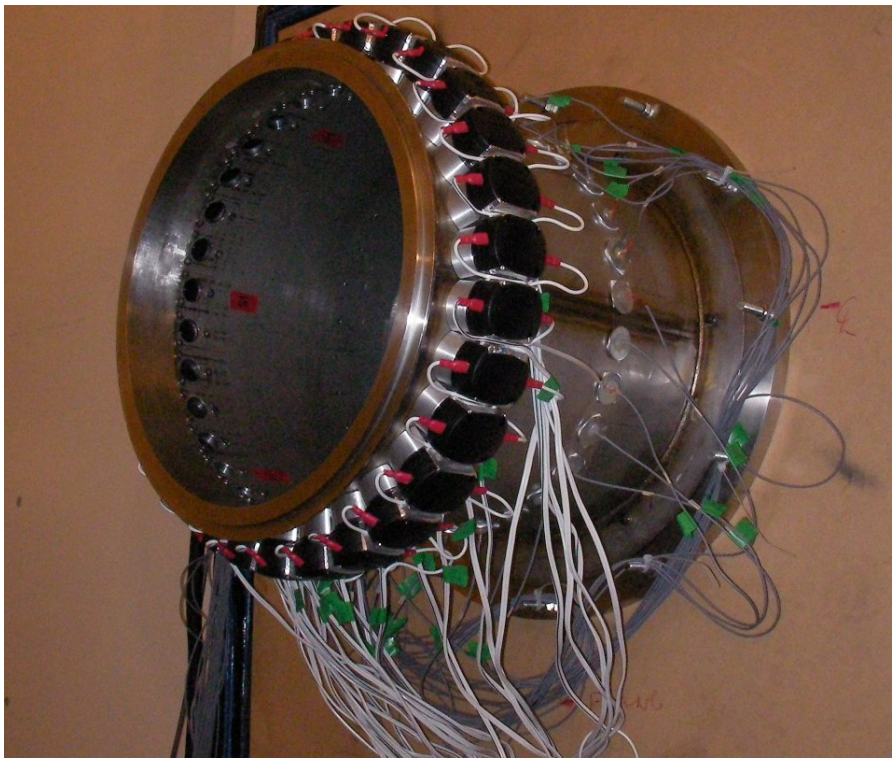

FIGURE 5.4: A photograph of the azimuthal microphone array mounted close to the open end of the duct. The microphone locations are indicated by the grey disks. Also shown is a ring of loudspeakers, not used in this experiment.

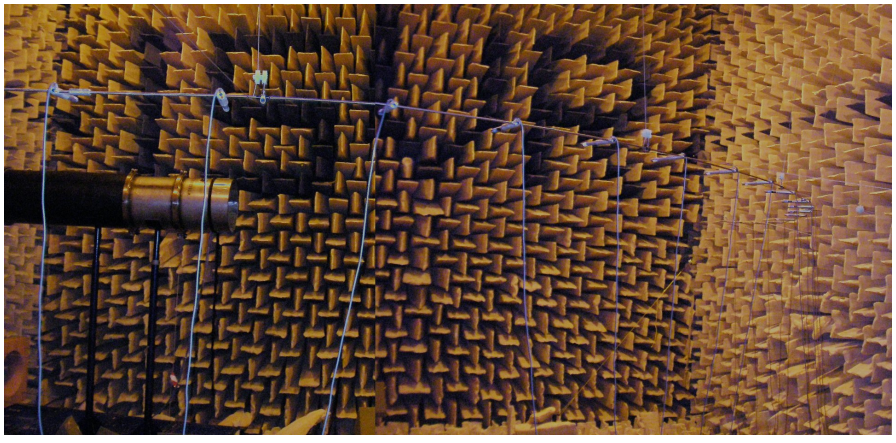

FIGURE 5.5: A photograph of the anechoic chamber taken from the main entrance. The far-field microphone array consists of 19 microphones suspended from the ceiling in a polar arc. The chamber floor has been removed to minimise reflections, except for a small area directly underneath the duct to allow access for the in-duct measurements. The duct is connected to the reverberation chamber through a baffled panel.

Far-field measurements were made at 19 positions spanning a 90° arc of 3.45 m radius, whose centre was located at the centre of the duct exit. The far-field microphone array was positioned at the same height as the centre of the duct exit, defined as an azimuthal angle of 0°. The microphones were positioned at 5° increments from 0° (on axis) to 90° (sideline) as shown in figure 5.1. The radiated sound field was assumed to be axi-symmetric consistent with the assumption of incoherent modes. Therefore the radiation is independent of azimuthal angle.

Far-field measurements were made using B&K type 4185 condenser microphones, connected to custom-made amplifiers. The same acquisition and post-processing hardware was used for both the in-duct and far-field microphones.

Noise-floor measurements were made both in-duct and in the far-field. Signal to noise ratio in the frequency range of interest, $ka < 30$, in the far-field was greater than 50 dB on axis falling to approximately 30 dB at 90 degrees. The in-duct signal to noise ratio was greater than 55 dB.

5.3 Results

Section 5.3.2 presents the predictions of far-field directivity using the in-duct beamformer measurements. We first determine radiated sound power using the induct measurements, as this provides a useful check of the validity of some of the assumptions made in the experiment.

5.3.1 Estimation of radiated sound power

Section 4.3.9 described how the sound power transmitted along the duct can be estimated using pressure measurements made at the duct wall for the special case of equal energy per mode. In this section the experimental data is used to validate the technique.

Assuming a multi-modal equal energy per mode sound field, the in-duct sound power, W_D, is calculated from in-duct pressure measurements by,

$$W_D = \frac{< \overline{p^2} > \mathcal{S}}{4\rho c} \tag{5.3}$$

where $< \overline{p^2} >$ denotes the average of the mean-square pressure at the 15 wall-mounted microphone positions in the case of the axial array, or the 30 positions in the case of the azimuthal microphone array. The far-field sound power, W_F, is estimated from the far-field assumption,

$$W_F = \frac{2\pi R^2}{\rho c} \int_\phi \overline{p_f^2} \sin\phi \, d\phi \tag{5.4}$$

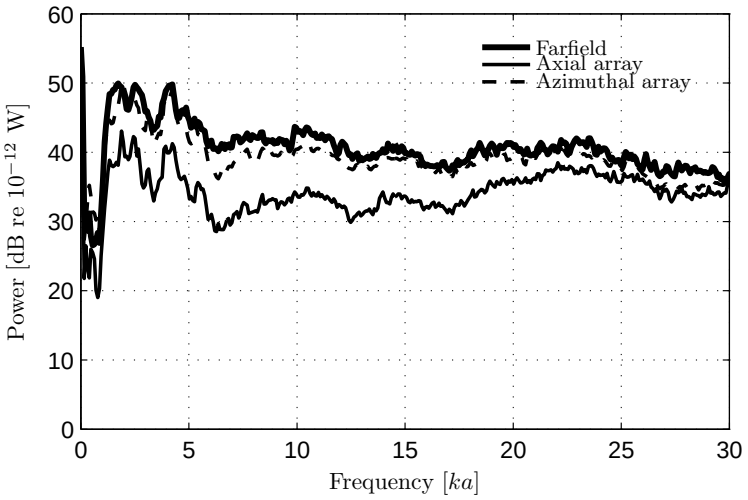

FIGURE 5.6: A plot of the sound power estimated using the induct axial array (solid curve) and azimuthal array (dashed curve) compared to the power measured in the far-field (thick solid curve) as a function of frequency, ka

where $R = 3.45\,\mathrm{m}$ is the distance from the centre of the duct exit to the far-field measurement locations.

Figure 5.6 is a comparison of the sound power estimated using the in-duct axial array (solid curve), and the power measured in the far-field (thick solid curve) as a function of frequency, ka. Also shown is the sound power estimated using the azimuthal microphone array (dotted curve). In the frequency range $ka = 18$ to $ka = 30$ the radiated sound power using the axial array is predicted to within 3dB, with the largest differences at $ka = 30$. At lower frequencies the in-duct axial array measurements under predicts the sound power by as much as 10dB. In comparison the in-duct azimuthal array predicts the sound power to within $1 - 2$dB across the whole range of frequencies. The source of the discrepancy between the power estimates using the two induct arrays is not clear. Considerable effort has been expended in determining the cause, possible explanations that remain are errors in calibrating the axial array, faulty equipment in the signal chain of the in-duct axial array, or differences caused by the axial array microphones not sitting exactly on the wall of the duct.

In the next section the in-duct array is used to predict the far-field directivity. A correction has been introduced in the measured magnitudes of the in-duct axial array microphones equivalent to the difference between the mean-square pressure measured by the azimuthal array, and that measured by the axial array. In effect the axial array has been calibrated, with respect to magnitude, using the azimuthal array data.

5.3.2 Prediction of far-field directivity from in-duct measurements

In this section the far-field polar directivity, calculated by multiplying the beamformer response by the predicted transfer function $|H(\phi, \omega)|^2$, is compared to the directly measured

far-field directivity. Predicted far-field directivities are obtained using the full transfer function, $|H(\phi,\omega)|^2$, given by equation (4.16) and based on a flanged duct model.

Far-field directivity predictions are presented in 1/3 octave frequency bands, as frequency averaging is found to improve agreement between predicted and measured directivities. The predicted far-field squared pressure in a given third-octave band with centre frequency ω_c, is the sum of the narrow band predicted directivities at frequencies between ω_l and ω_u,

$$|p_f(\phi,\omega_c)|^2 = \sum_{\omega_i=\omega_l}^{\min\{\omega_u,\omega_{\max}\}} |H(\phi,\omega_i)|^2 |b(\phi,\omega_i)|^2 \Delta\omega_i \tag{5.5}$$

where $\Delta\omega_i$ is the analysis frequency bandwidth, and $\omega_{\max}$ is the frequency at which the in-duct array is aliased.

5.3.3 Predictions of far-field directivity

This section contains the main experimental results of this chapter. The in-duct beamformer is used to predict the far-field directivities based on equation (5.5). Different array lengths are tested by extracting a sub-set of microphone measurements from the full array. Arrays consisting of the first 5, 10 or 15 microphones of the array are used and the results compared with the far-field measured directivity.

In the plots that follow the solid curves correspond to the predicted far-field directivity obtained using $|H(\phi,\omega)|^2$ calculated from equation (4.16). The crosses are the measured far-field directivities. The lower plots in each figure are the normalised beamformer outputs, $|b(\phi,\omega)|^2$, as a function of beamsteer angle. Solid horizontal lines in the lower plots show the beamwidth of the in-duct beamformer at 45°.

Figures 5.7 to 5.9 show the results for the 4000 Hz third-octave band, corresponding to $ka = 14.8$ (lower frequency $ka = 13$, upper frequency $ka = 16.4$), using 5, 10 and 15 microphones respectively. The shape of the predicted directivity is in good agreement with that measured from 10° to approximately 70°. At high angles the flanged duct model used in the prediction of $|H(\phi,\omega)|^2$ is the most probable cause of the discrepancies at high angles, and a model more appropriate to the unflanged duct used would improve the predictions.

The overall level in the far-field is well-predicted to within 1dB up to 70°. At low angles the technique under-predicts the far-field levels, this is likely due to a combination of the duct having greater on-axis directivity when fewer modes are able to propagate, and the low-angle beamformer correction presented in equation (4.22) not performing well at low-frequencies.

As the array length increases the amount of detail visible in the predicted directivity increases. This is due to the decreasing beamwidth as indicated by the horizontal lines

in the lower plots. In figure 5.9, using a 15 microphone array, the small inflection in the directivity pattern at 40° is reflected in the predicted far-field directivity. The scale of the details visible are comparable to the beamwidth, this is consistent with the simulations in section 4.3.8.

The normalised beamformer output in figures 5.7 to 5.9 has a magnitude variation of approximately 2dB over the range of angles $0° \leq \phi \leq 60°$. This variation is larger than that predicted for equal energy per mode in section 4.3.2 but not as large as for equal amplitude or the volume velocity source model.

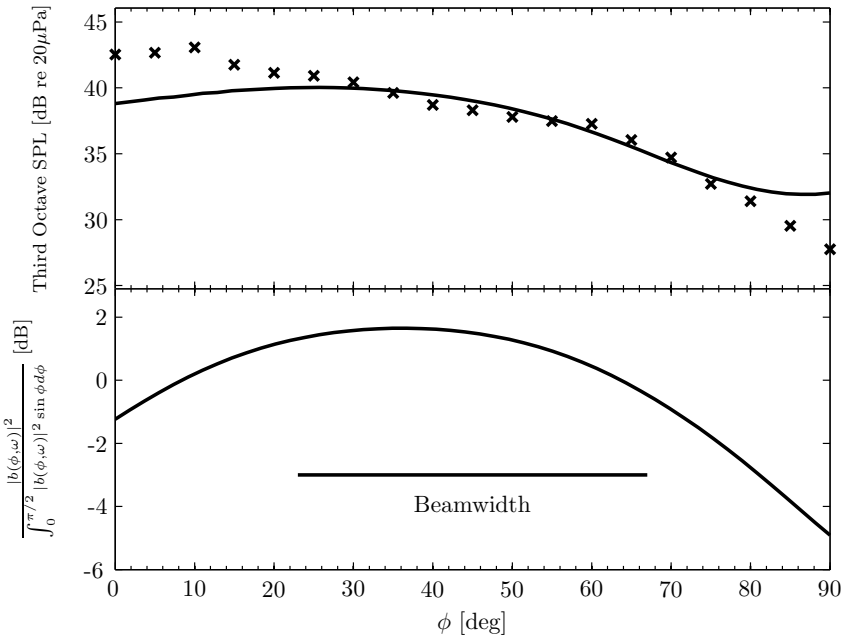

FIGURE 5.7: Predicted far-field directivities (top) and normalised beamformer output (bottom) in the 4000 Hz ($ka = 14.6$) third-octave band using an array of 5 microphones spaced 2.5 cm apart. The solid curve in the top plot uses the full transfer function and the crosses denote measured far-field pressures.

Figures 5.10 to 5.12 show the results for the 5000 Hz third-octave band, corresponding to $ka = 18.4$ (lower frequency $ka = 16.4$, upper frequency $ka = 20.6$). The estimated far-field levels in this case are now closer to those measured at lower angles, and continues to capture the measured directivity levels to within 11dB between 10° and 70°.

Figures 5.13, 5.14 and 5.15 show the results for the 6300 Hz third octave band, corresponding to $ka = 23.1$ (lower frequency $ka = 20.6$, upper frequency $ka = 25$), for an array with 5, 10 and 15 microphones respectively. This is the highest frequency band investigated, as frequencies above 6800 Hz ($ka = 25$) are aliased by the in-duct array. For each array size, the predicted directivity levels are less than 1dB away from the measured directivity from 0° to 70°. The predicted directivity pattern follows the measured pattern very closely.

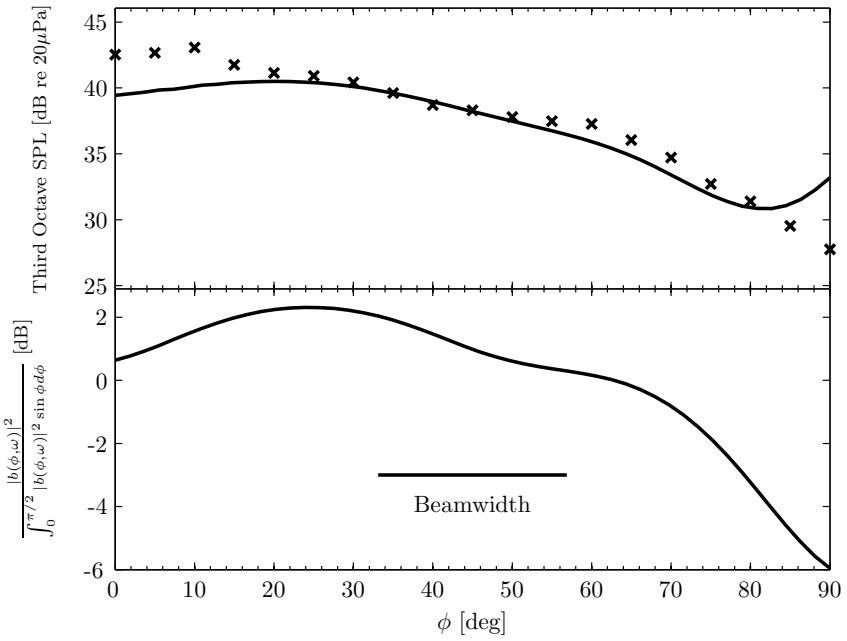

FIGURE 5.8: Predicted far-field directivities (top) and normalised beamformer output (bottom) in the 4000 Hz ($ka = 14.6$) third-octave band using an array of 10 microphones spaced 2.5 cm apart.The solid curve in the top plot uses the full transfer function and the crosses denote measured far-field pressures.

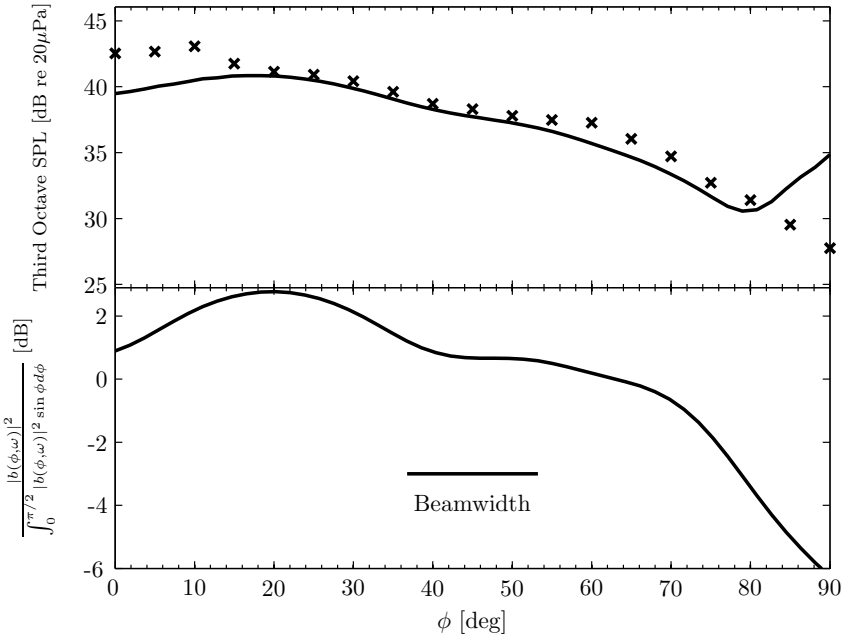

FIGURE 5.9: Predicted far-field directivities (top) and normalised beamformer output (bottom) in the 4000 Hz ($ka = 14.6$) third-octave band using an array of 15 microphones spaced 2.5 cm apart. The solid curve in the top plot uses the full transfer function and the crosses denote measured far-field pressures.

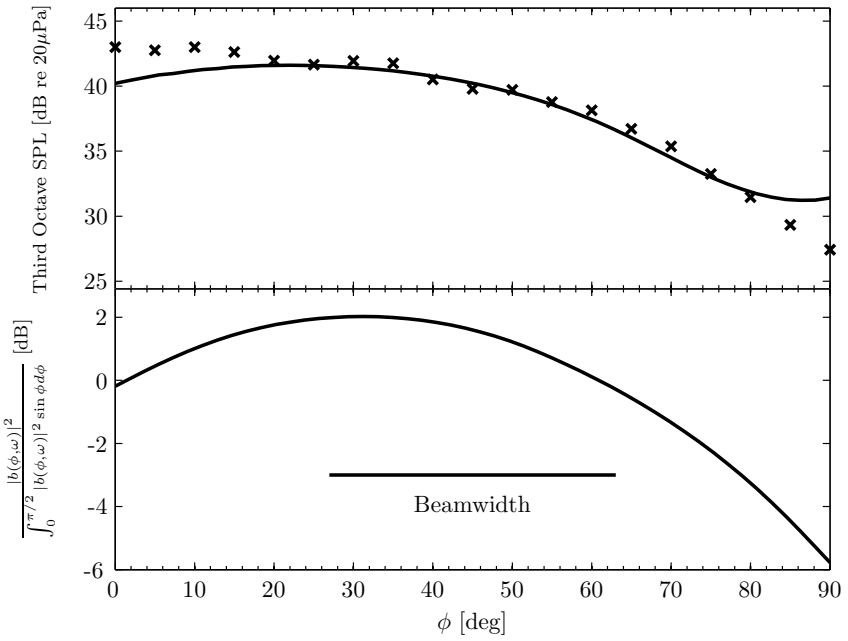

FIGURE 5.10: Predicted far-field directivities (top) and normalised beamformer output (bottom) in the 5000 Hz ($ka = 18.4$) third-octave band using an array of 5 microphones spaced 2.5 cm apart. The solid curve in the top plot uses the full transfer function and the crosses denote measured far-field pressures.

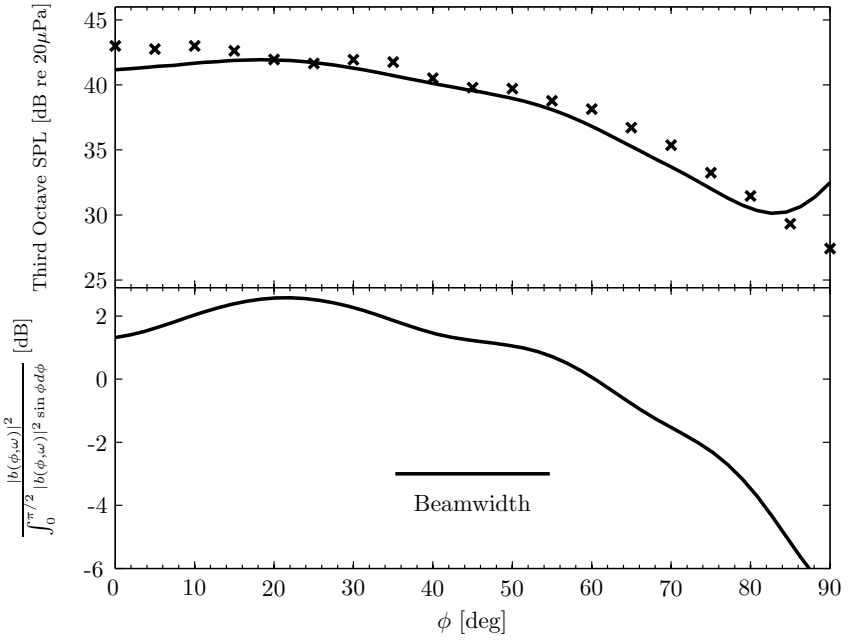

FIGURE 5.11: Predicted far-field directivities (top) and normalised beamformer output (bottom) in the 5000 Hz ($ka = 18.4$) third-octave band using an array of 10 microphones spaced 2.5 cm apart. The solid curve in the top plot uses the full transfer function and the crosses denote measured far-field pressures.

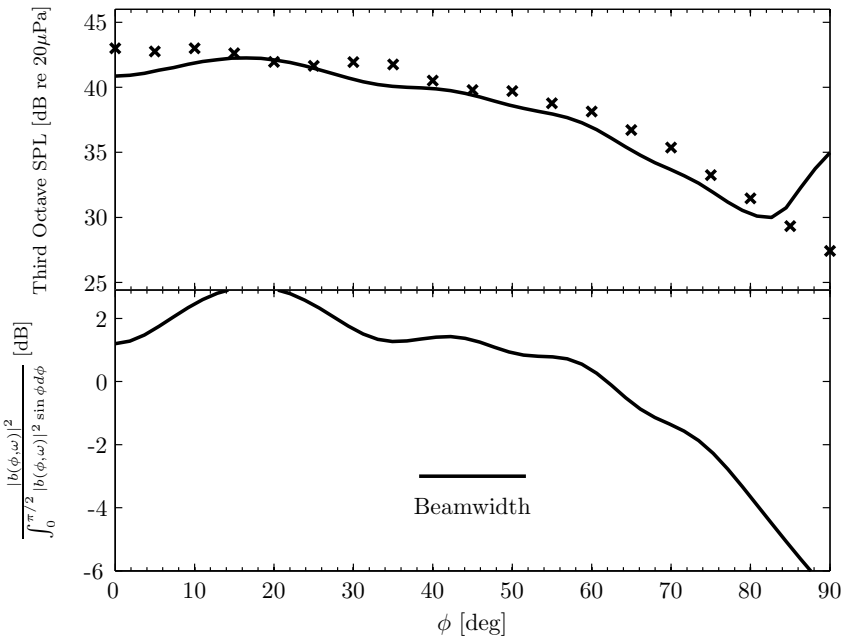

FIGURE 5.12: Predicted far-field directivities (top) and normalised beamformer output (bottom) in the 5000 Hz ($ka = 18.4$) third-octave band using an array of 15 microphones spaced 2.5 cm apart. The solid curve in the top plot uses the full transfer function and the crosses denote measured far-field pressures.

The variation in level of the normalised beamformer output in this frequency band is also much smaller, indicating that the sound field has approximately equal energy per mode.

For the 15 microphone array, figure 5.15, the resolution is sufficiently good that the technique is able to predict small oscillations in the radiated directivity pattern. Note that the small "dip" in the directivity pattern close to 30°, and a point of inflection at 60° have both been captured by the in-duct to far-field technique.

5.4 Conclusion

In this chapter the in-duct to far-field prediction technique developed in chapter 4 has been validated using a no-flow laboratory-scale experiment. Results from the experiment show that the in-duct to far-field technique can accurately predict the shape of the radiated far-field directivity pattern when the in-duct sound field has incoherent modes. Prediction of the magnitude is also good, although a correction was introduced to account for a failure of the sound power predicted with the axial microphone array to agree with that predicted by the azimuthal microphone array. The most accurate predictions are achieved for frequencies close to the optimum frequency of the array, where $\Delta z = \lambda/2$. The ability of the technique to predict detailed features in the radiated directivity pattern is greatest when the longest array, consisting of 15 microphones, is used.

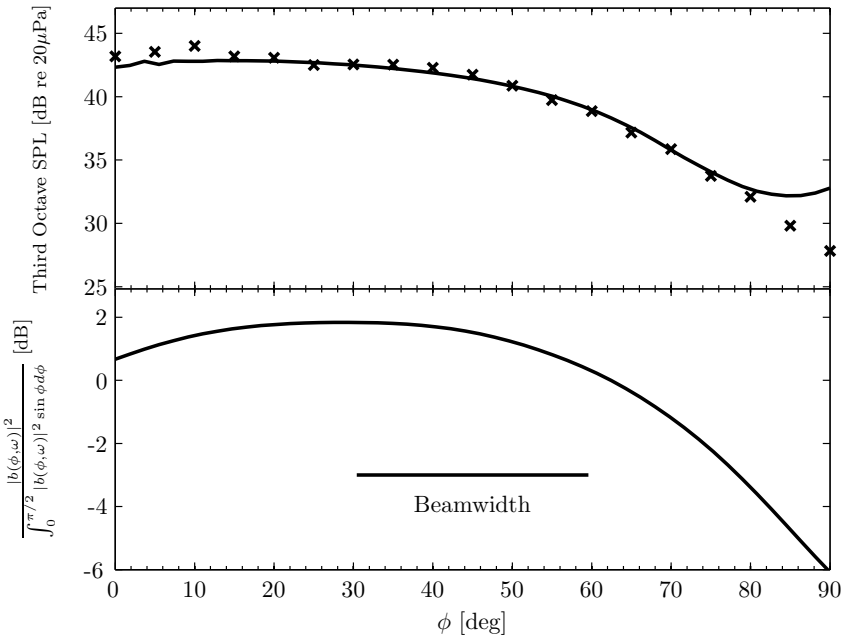

FIGURE 5.13: Predicted far-field directivities (top) and normalised beamformer output (bottom) in the 6300 Hz ($ka = 23.15$) third-octave band using an array of 5 microphones spaced 2.5 cm apart. The solid curve in the top plot uses the full transfer function and the crosses denote measured far-field pressures.

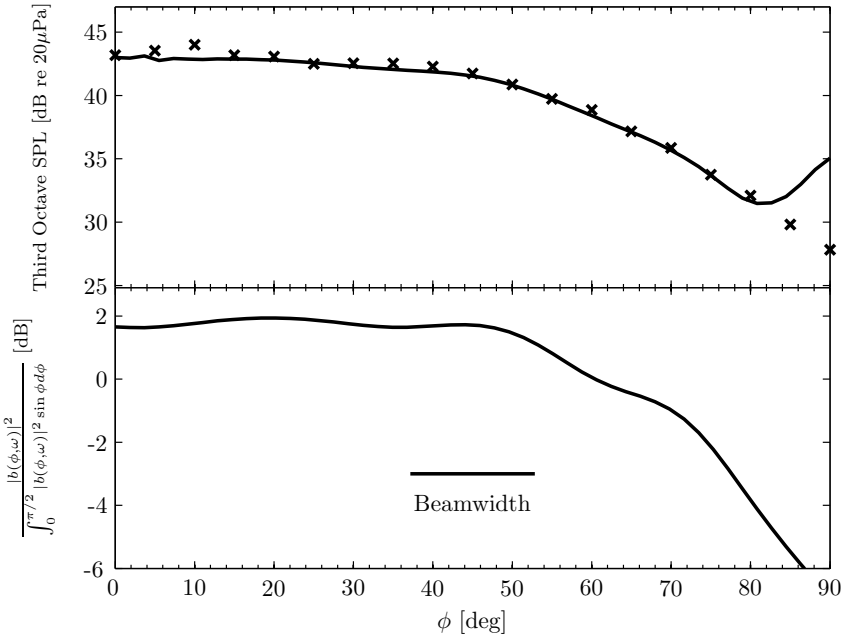

FIGURE 5.14: Predicted far-field directivities (top) and normalised beamformer output (bottom) in the 6300 Hz ($ka = 23.15$) third-octave band using an array of 10 microphones spaced 2.5 cm apart. The solid curve in the top plot uses the full transfer function and the crosses denote measured far-field pressures.

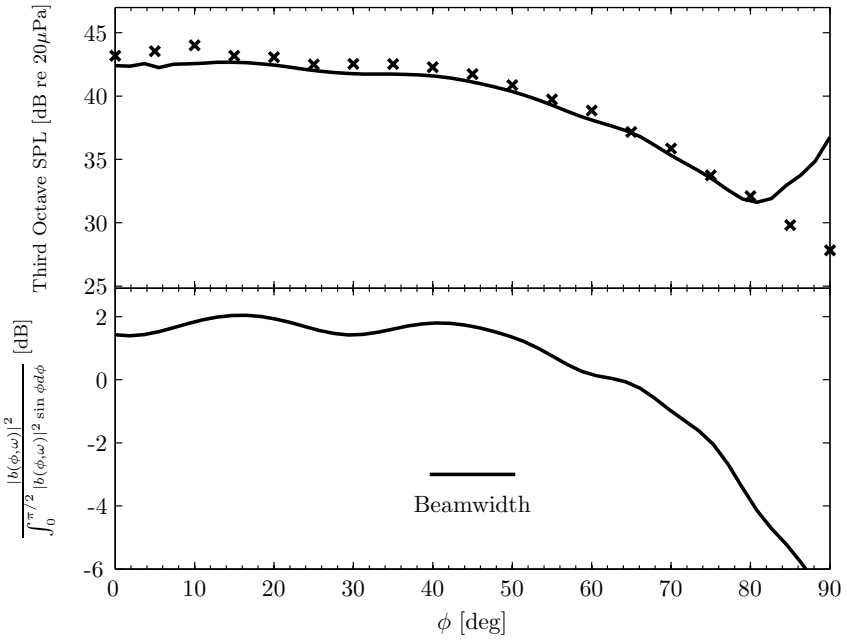

FIGURE 5.15: Predicted far-field directivities (top) and normalised beamformer output (bottom) in the 6300 Hz ($ka = 23.15$) third-octave band using an array of 15 microphones spaced 2.5 cm apart. The solid curve in the top plot uses the full transfer function and the crosses denote measured far-field pressures.

Chapter 6

An *in-situ* phase calibration technique for in-duct axial microphone arrays

6.1 Introduction

In the previous chapter an axial beamformer at the duct wall was used to estimate far-field directivity. The beamformer output was formed from multiplying the complex pressure signals by complex weighting factor and then summing. The microphones were first calibrated with respect to magnitude and phase, therefore the microphones themselves did not introduce any additional weighting factors due to differences between them.

Calibration of the microphone sensitivity is typically achieved using a piston-phone. The microphone is placed in a sound field with a known pressure level. The resulting voltage output from the microphone is related to the known level and, by assuming that the microphone has a linear response, the sensitivity (typically expressed in millivolts per Pascal) is determined.

Phase calibration is more difficult, however. Unless expensive "phase-matched" microphones are used, manufacturing differences between individual microphones cause them to have differing phase responses. To correct for this, each microphone will typically be placed close to a *reference microphone* in the presence of a broadband sound field and the relative phase response as a function of frequency between the two microphones will be measured. This was the technique used to calibrate the microphone array for the experiment presented in chapter 5. For large arrays, for example those needed for mode detection, or the inverse techniques described earlier in the thesis, this is a time consuming process. Moreover for in-duct microphone arrays this technique cannot be performed *in-situ*. The microphones must therefore be calibrated outside of the duct.

However this is unsatisfactory as changes in the phase response that result from mounting the microphones in the duct wall after calibration, where they are exposed to flow and temperature effects, and the effects of the microphone mounting are not accounted for.

In this chapter a calibration technique is proposed that allows the simultaneous *in-situ* calibration of in-duct axial microphone arrays. This technique is an extension of a technique proposed for SONAR applications to calibrate towed arrays. It relies on the observation that the measured pressure cross-spectral matrix, $\mathbf{S}_{pp}$, for a microphone array with equally spaced identical sensors, in a sound-field without reflections is Töplitz. A Töplitz matrix is one in which the elements in each diagonal are identical. Thus, the cross-spectrum is only a function of the separation distance between sensors. In this chapter the calibration technique is investigated in relation to ducted sound fields. Experimental data from chapter 5 is used to validate the technique.

6.2 Theory

Consider a phased array of N equally spaced sensors mounted in an axial line at the duct wall. From chapter 4 the beamformer output is given by

$$S_{bb} = \mathbf{w}\mathbf{S}_{pp}\mathbf{w}^H \tag{6.1}$$

where $\mathbf{w}$ is a vector of weighting factors defined in equation (4.10) and $\mathbf{S}_{pp}$ is the measured cross-spectral matrix of pressures at the microphone array. Equation (2.3) for the sound field in an infinite duct, under the assumption of incoherent modes and the absence of reflections from the open end of the duct, shows that for equally-spaced identical sensors, $\mathbf{S}_{pp}$ has a Hermitian Töplitz structure, that is

$$S_{p_i p_j} = S_{p_k p_l} \quad \text{when} \quad i - j = k - l \tag{6.2}$$

$$S_{p_i p_j} = S^*_{p_j p_i} \tag{6.3}$$

where $S_{p_i p_j}$ is the $(i,j)^{\text{th}}$ element of $\mathbf{S}_{pp}$. This property arises from the fact that in the absence of reflections the pressure cross-spectrum is only a function of the separation distance between the sensors, and not their absolute position.

For non-identical microphones, each microphone has a different phase and amplitude response and the measured cross-spectral matrix deviates from the Hermitian Töplitz form. Instead it takes the Hermitian form

$$\tilde{\mathbf{S}}_{pp} = \Gamma\mathbf{S}_{pp}\Gamma^H \tag{6.4}$$

where Γ is a diagonal matrix of complex errors with gain, g_i, and phase, ϕ_i

$$\Gamma = \mathrm{diag}(g_1 e^{\mathrm{i}\phi_1}, g_2 e^{\mathrm{i}\phi_2}, ..., g_N e^{\mathrm{i}\phi_N}) \tag{6.5}$$

For an array in an infinite duct the Töplitz structure is expected to be a valid assumption for both the gain and phase components of $\mathbf{S}_{pp}$. This is because reflections from the open end of a duct can be assumed to be small except at very low frequencies, $ka < 1$, as long as the frequency is not close to a modal cut-on frequency. In this chapter we consider phase calibration, since amplitude calibration is readily performed using, for example, a piston-phone.

We denote the difference in phase between microphones i and j arising entirely from their different locations Φ_{ij}, which we assume has the property $\Phi_{ij} = \Phi_{kl}$ for $i - j = k - l$. From equation (6.4) the phase of the measured cross-spectral matrix $\tilde{\mathbf{S}}_{pp}$ therefore has the form

$$\mathrm{angle}(\tilde{\mathbf{S}}_{pp}) = \begin{pmatrix} 0 & \Phi_{12}+\phi_1-\phi_2 & \Phi_{13}+\phi_1-\phi_3 & \cdots & \Phi_{1N}+\phi_1-\phi_N \\ & 0 & \Phi_{23}+\phi_2-\phi_3 & \cdots & \Phi_{2N}+\phi_2-\phi_N \\ & & 0 & \ddots & \vdots \\ & & & 0 & \Phi_{(N-1)N}+\phi_{(N-1)}-\phi_N \\ & & & & 0 \end{pmatrix} \tag{6.6}$$

where $\tilde{\mathbf{S}}_{pp}$ is Hermitian and for clarity only the upper triangular half of the matrix is shown.

Using the property, $\Phi_{ij} = \Phi_{kl}$ when $i - j = k - l$, we can write the system of equations from equation (6.6)

$$\phi_i - 2\phi_{i+1} + \phi_{i+2} = \nu_i = \mathrm{angle}(\tilde{\mathbf{S}}_{p_i p_{(i+1)}}) - \mathrm{angle}(\tilde{\mathbf{S}}_{p_{(i+1)} p_{(i+2)}}) \qquad (i = 1, 2, \ldots, N-2) \tag{6.7}$$

where ν_i is the measured difference in phase between *adjacent* elements in the leading diagonal of $\tilde{\mathbf{S}}_{pp}$.

Note that the left hand side of equation (6.7) contains only microphone phase errors while the right hand side contains only measurable phase quantities. The solution of the system of equations (6.7) for the reconstructed phase errors $\hat{\boldsymbol{\phi}} = [\hat{\phi}_1, \hat{\phi}_2, \ldots, \hat{\phi}_N]^T$ follows from multiplying the vector of phase differences $\boldsymbol{\nu} = [\nu_1, \nu_2, \ldots, \nu_N]^T$ by the pseudo-inverse of the coefficient matrix $\mathbf{C}$,

$$\hat{\boldsymbol{\phi}} = \mathbf{C}^{+}\boldsymbol{\nu} \tag{6.8}$$

where, from equation (6.7), $\mathbf{C}$ is a $(N-2)\times N$ banded matrix of the form,

$$\mathbf{C} = \begin{bmatrix} 1 & -2 & 1 & 0 & 0 & 0 & 0 \\ 0 & 1 & -2 & 1 & 0 & 0 & 0 \\ 0 & 0 & \ddots & \ddots & \ddots & 0 & 0 \\ 0 & 0 & 0 & 1 & -2 & 1 & 0 \\ 0 & 0 & 0 & 0 & 1 & -2 & 1 \end{bmatrix} \tag{6.9}$$

The cross-spectral matrix, $\hat{\mathbf{S}}_{pp}$, corrected for phase errors is then given by

$$\hat{\mathbf{S}}_{pp} = \hat{\mathbf{\Gamma}}\tilde{\mathbf{S}}_{pp}\hat{\mathbf{\Gamma}}^H \tag{6.10}$$

where

$$\hat{\mathbf{\Gamma}} = \mathrm{diag}(e^{-\mathrm{i}\hat{\phi}_1}, e^{-\mathrm{i}\hat{\phi}_2}, ..., e^{-\mathrm{i}\hat{\phi}_N}) \tag{6.11}$$

Calibration of the phase errors in an axial hydrophone array performed using equation (6.8) was proposed by Sng and Li [67]. Their work was a specific formulation of the general technique proposed in an earlier paper by Paulraj and Kailath [68]. The Paulraj and Kailath method was based on using a larger system of equations obtained from the differences of *all* the elements of equation (6.6) where $i-j=k-l$. This chapter will investigate the effectiveness of both techniques for calibrating the phase of in-duct microphones.

Note from equation (6.9) that the rank of the coefficient matrix, $\mathbf{C}$, is $N-2$ and hence the system of equations is under-determined. The coefficient matrix $\mathbf{C}$ has two vectors in its null-space, $[1,1,\ldots,1]^T$ and $[1,2,\ldots,N]^T$. When solving for the phase errors in a least-square sense, using equation (6.8), the first null-space vector implies that the phase of the microphones can only be determined to within an arbitrary reference. This is not a problem for the phase calibration of in-duct microphone arrays, since we are only interested in the relative phase between microphones. The second null-space vector implies that phase errors can only be determined to within an arbitrary progressive phase factor. As noted by Paulraj and Kailath this can manifest itself in the recovered phase errors as a rotation of the beam by an arbitrary angle. In practice, as will be demonstrated by the simulations and experimental results in this chapter, this effect is rarely noticable when the technique is used for in-duct array calibration.

6.3 Application of the array calibration technique to simulated data

To illustrate the application of the phase calibration technique we now consider some simple simulated examples of applying the technique to perform the calibration of a

microphone array in a circular, hard-walled infinite duct. Figure 6.1 is a plot of the beamformer output as a function of steering angle in the presence of a single $(15, 0)$ mode with mode ray angle of 58°. The microphone array comprises 15 equally spaced microphones, $\lambda/2$ apart. In figure 6.1a the beamformer output with perfectly calibrated sensors (dashed curve) is compared to the output obtained in which each sensor has an additional phase error (dotted curve) obtained randomly from a normal distribution with 0° mean and 30° standard deviation. When phase errors are introduced there is a considerable increase in the level of the side lobes particularly at angles greater than 90°. The locations of the sidelobe patterns are also less clearly defined.

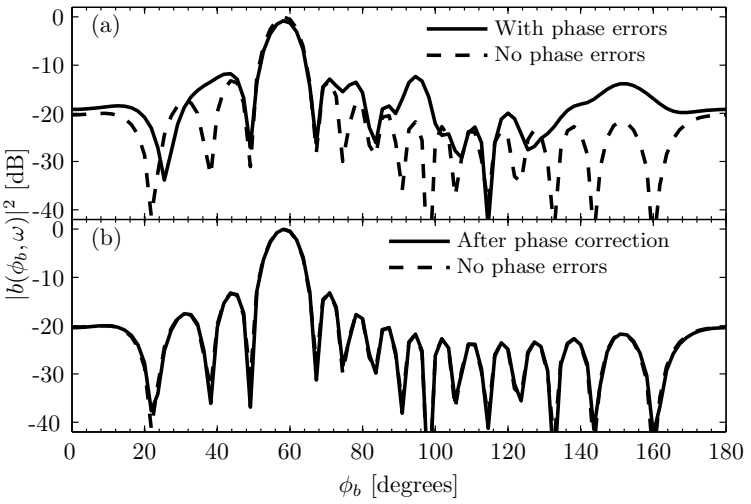

FIGURE 6.1: Beamformer output as a function of steering angle due to a single $(15, 0)$ mode with mode ray angle 58° incident on the array. The top figure shows the beamformer output with perfectly calibrated sensors (dashed) and with sensors where phase errors have been introduced (solid). The lower figure is a plot of the beamformer output calculated with sensor errors reconstructed using the Sng method (solid) compared to the perfectly calibrated sensors (dashed)

Figure 6.1b shows the beamformer output after correcting for the phase errors using the calibration technique in section 6.2. The solid line is the beamformer output obtained using the phase errors obtained by equation (6.8). The dashed line again is the solution obtained with perfectly calibrated sensors. The difference between the two curves is very small for all beamsteer angles, indicating that the least-squares approach of equation (6.8) recovers the phase errors close enough to dramatically improve the beamformer response. The accuracy of the recovery of phase errors by the technique is investigated in section 6.4.2.

Figure 6.2 is the beamformer output obtained by following an identical procedure to that in figure 6.1, but in a multi-mode equal energy per mode sound field. In figure 6.2a the introduction of phase errors to the microphone signals increases significantly the level of the sidelobes in the range of beam-steer angles $90° \leq \phi \leq 180°$. In practice, this would lead to an erroneous measurement of the sound power reflected from the duct termination. Note, however, that in this sound field, even with phase errors present the

beamformer output is relatively independent of beam-steer angle between 0° and 70°. This is consistent with the observation that an equal energy per mode sound field results in incoherent signals at the microphones when they are spaced $\lambda/2$ apart. A greater sensitivity to phase errors is therefore anticipated for other types of sound field.

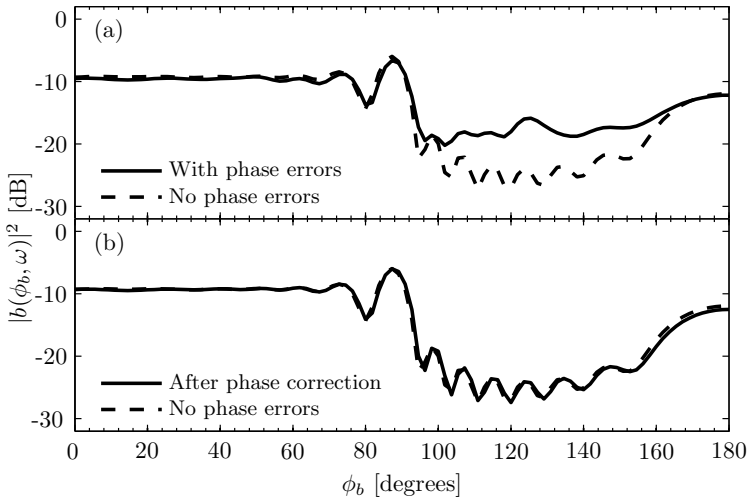

FIGURE 6.2: Beamformer output as a function of steering angle due to an equal energy per mode sound field in the duct. The top figure shows the beamformer output with perfectly calibrated sensors (dashed) and with sensors where phase errors have been introduced (solid). The lower figure is a plot of the beamformer output calculated with sensor errors reconstructed using the Sng method (solid) compared to the perfectly calibrated sensors (dashed)

In figure 6.2b the beamformer output obtained from equation (6.8) (solid) is compared to that obtained using perfectly calibrated sensors (dashed). The difference between the two curves is small across all angles, indicating that the phase calibration technique has recoved the sensor errors well enough to improve the beamformer performance. The performance of the technique depends on the exact distribution of random phase errors introduced, however experience indicates that performance comparable with figure 6.2 is achieved for most simulations using this random distribution of phase errors.

6.4 Experimental validation of the array calibration technique

In this section the experimental data presented in chapter 5 is used to validate the array calibration technique proposed in this chapter. We start by verifying the assumption that the measured cross-spectral matrix has a Töplitz structure. We then apply the technique of section 6.2 to the data and attempt to determine the phase errors for each microphone. These phase errors will be compared to those obtained by comparison with a calibrated reference microphone.

6.4.1 Evidence for the Töplitz structure of $\mathbf{S}_{pp}$

The solid curve in figure 6.3 is a plot of measured phase difference, Φ_{ij}, measured in the duct averaged over 14 adjacent pairs of phase-calibrated microphones 1.5cm apart, as a function of normalised frequency $\Delta z/\lambda$. The phase difference has been "unwrapped" (that is absolute jumps greater than *pi* are changed to their 2π complement) for clarity of presentation. The error bars show plus and minus one standard deviation, σ_Φ, from the mean across the 14 phase estimates.

Frequency (Hz)	Frequency (ka)	σ_Φ
2750	10	7°
5490	20	14°
8225	30	21°

TABLE 6.1: Standard deviation of the measured phase in figure 6.3.

Below approximately $\Delta z/\lambda = 1$ ($13.6k$Hz,$ka = 50$) the standard deviation, σ_Φ is small, less than 30°. The standard deviation at particular frequencies is tabulated in table 6.1. The small standard deviation indicates that $\mathbf{S}_{pp}$ has the required Töplitz form to this level of accuracy. The standard deviation increases as frequency increases, and becomes very large for $\Delta z/\lambda > 0.85$. When the wavelength is smaller than the microphone separation distance the phase differences become significantly larger.

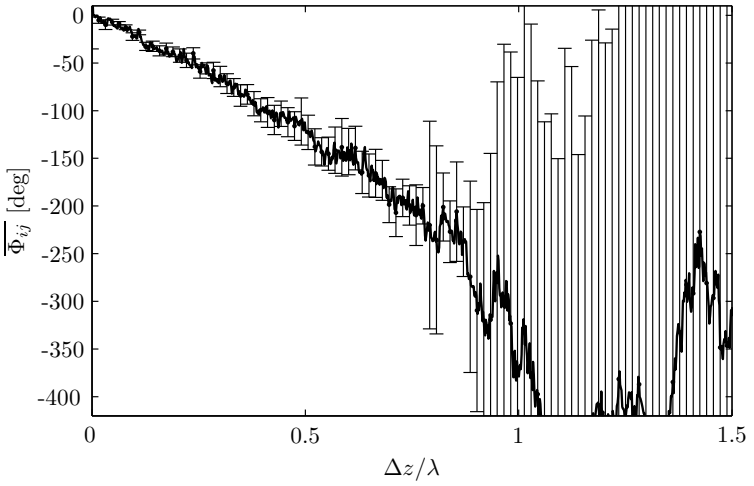

FIGURE 6.3: Mean and standard deviation of the phase angle between adjacent microphones in a duct when $\Delta z = 2.5\,$cm. Statistics based on 15 microphones.

Figure 6.4 plots the mean and standard deviation for the phase differences of the second off-diagonal elements of $\mathbf{S}_{pp}$, that is for pairs of microphones spaced 5 cm apart. Below a normalised frequency of $\Delta z/\lambda = 1$ ($6.8k$Hz,$ka = 25$) the standard deviation is approximately 20°, and increases dramatically for $\Delta z/\lambda 0.851$

The behaviour observed in figures 6.3 and 6.4 is the direct result of the uncertainty in making the phase spectrum measurements. Piersol [69] has shown that the phase

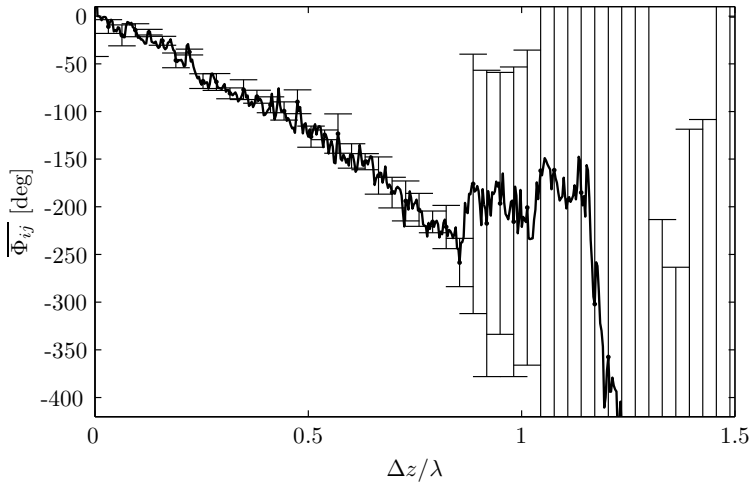

FIGURE 6.4: Mean and standard deviation of the phase angle between adjacent microphones in a duct when $\Delta z = 5\,\text{cm}$. Statistics based on 8 microphones.

spectrum has a variance of

$$\sigma_\Phi \approx \frac{1-\gamma^2}{2r\gamma^2} \tag{6.12}$$

where r is the number of data segments used in the phase estimate. Thus at microphone separation distances greater than approximately $\lambda/2$, the coherence, γ^2, between two microphones in a multi-mode broadband sound field tends to zero, leading to large random errors in the measured spectrum. Figure 6.5 is a plot of the coherence between a pair of microphones separated by 2.5 cm and a pair separated by 5 cm, as a function of $\Delta z/\lambda$. The upper plot is obtained from the raw data, the lower plot is processed with a 200 Hz moving average. The coherence drops to approximately 0.2 at $\Delta z/\lambda = 0.85$ for both separation distances. This, and the large variability shown in the upper plot, causes σ_Φ in equation (6.12) to become large above this frequency, as seen in figures 6.3 and 6.4.

6.4.2 Application of the calibration technique to the in-duct microphone array

The calibration technique is now applied to determine the phase errors of the microphones used in chapter 5. Figure 6.6 is a plot of the measured phase errors relative to microphone 1 as a function of frequency for microphones 1, 3, 5 and 11, obtained by comparison with a calibrated reference microphone, as described in section 5.2.2. Phase errors below $12k$Hz are observed to be less than approximately 20° and are typically 10°.

Figure 6.7 is a plot of the reconstructed phase errors as a function of frequency of microphone 3 using the Paulraj (top) and Sng (bottom) methods. The Sng method (which uses just the first off-diagonal elements of the cross-spectral matrix) is observed to reconstruct the directly measured phase error to within a few degrees up to approximately $4k$Hz. Above this frequency the deviation of the reconstructed phase errors from the measured

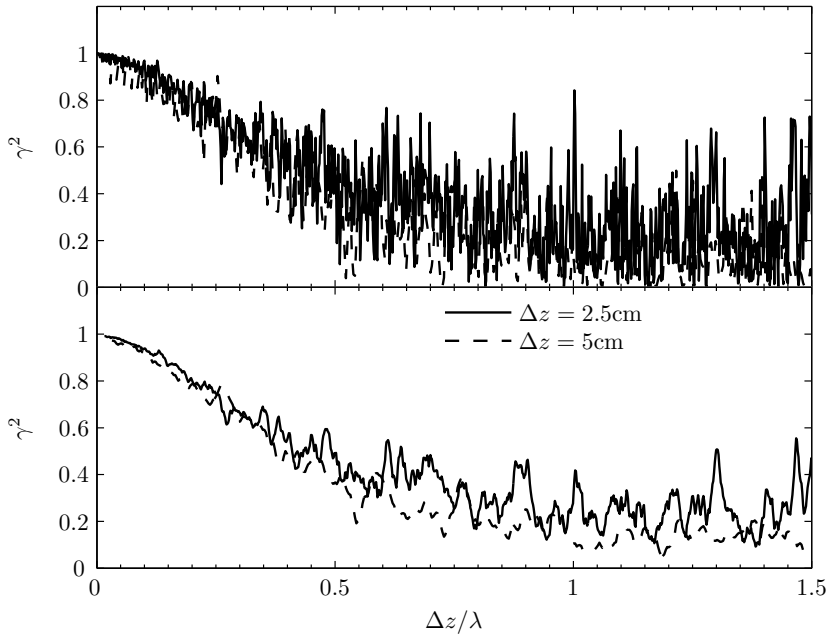

FIGURE 6.5: Measured coherence between a pair of microphones separated by 2.5 cm (solid line) and 5 cm (dashed line) as a function of $\Delta z/\lambda$. The upper plot is obtained from the raw data, the lower plot is processed with a 200 Hz moving average.

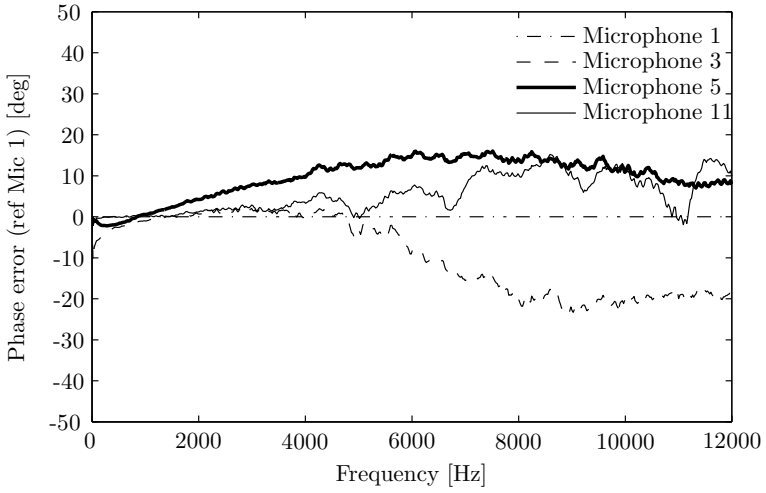

FIGURE 6.6: A plot of the measured phase errors relative to microphone 1 as a function of frequency for microphones 1, 3, 5 and 11.

phase errors is appreciably greater, although the mean trend of the measured curve is reasonably well captured. The Paulraj method, which uses the entire $\mathbf{S}_{pp}$ cross-spectral matrix, performs less well than the Sng method, reconstructing the measured phase errors to within a few degrees only up to approximately 1000 Hz. Random fluctuations of the phase estimate about the mean are also significantly greater.

As discussed in section 6.4.1 the pressure cross-spectral matrix using calibrated sensors has a form closer to Töplitz for diagonals close to the leading diagonal, i.e. for pairs of microphones that are closest together. Since the Paulraj method uses all diagonals in $\mathbf{S}_{pp}$, the results are contaminated by the data from those microphone pairs which suffer

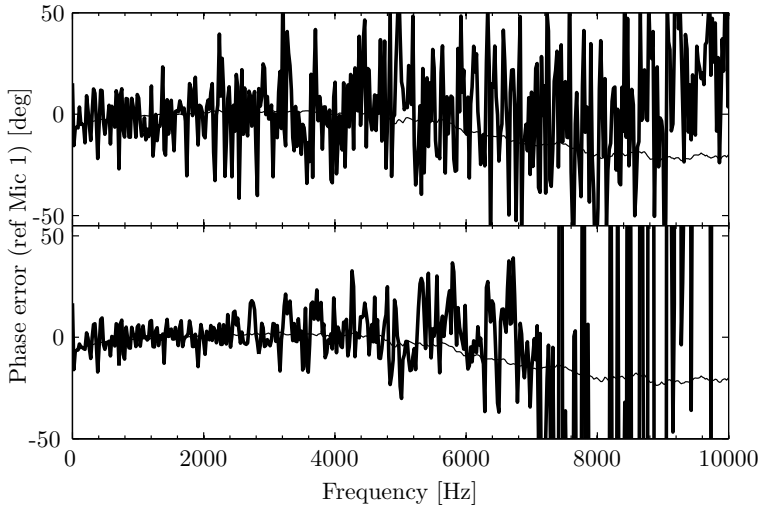

FIGURE 6.7: A plot of the reconstructed phase errors as a function of frequency of microphone 3 using the Paulraj (top) and Sng (bottom) methods. The thin line is the measured phase error, the thicker line is the reconstructed phase error.

from large coherence loss, that is when $\Delta z > \lambda$. The method proposed by Sng uses the first diagonal of $\mathbf{S}_{pp}$ only, and hence a large proportion of the data used to deduce the phase errors are obtained from microphones separated by more than a wavelength.

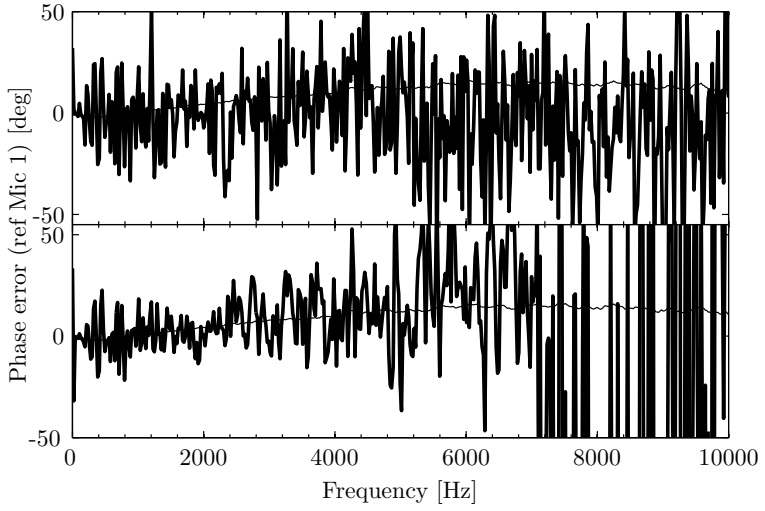

FIGURE 6.8: A plot of the reconstructed phase errors as a function of frequency for microphone 5 using the Paulraj (top) and Sng (bottom) methods. The thin line is the measured phase error, the thicker line is the reconstructed phase error.

Figures 6.8 and 6.9 are plots of the reconstructed phase errors for microphones 5 and 11 using both methods. The Sng method recovers the shape of the phase error curve more closely than the Paulraj method for both microphones.

The random fluctuations present on the reconstructed phase data in figures 6.7, 6.8 and 6.9 may be significantly reduced by frequency averaging. This approach is justified if the phase errors to be reconstructed can be assumed to be relatively slowly varying. Figure 6.10 is a plot of the reconstructed phase errors after the application of a 10 point

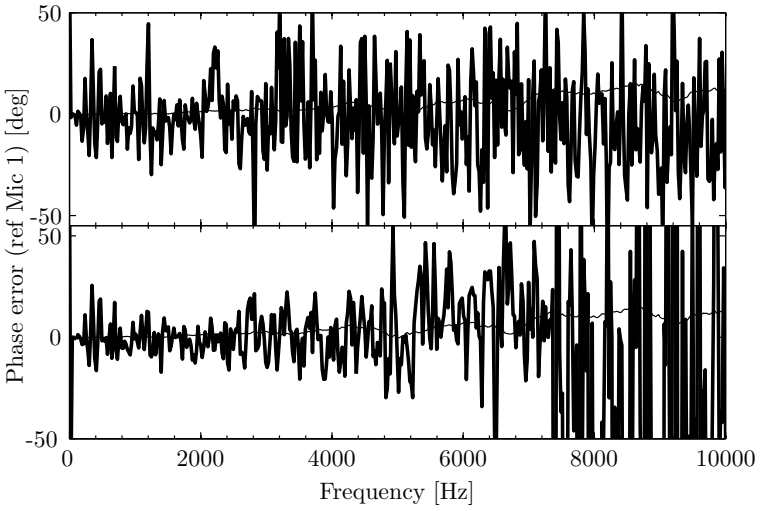

FIGURE 6.9: A plot of the reconstructed phase errors as a function of frequency of microphone 11 using the Paulraj (top) and Sng (bottom) methods. The thin line is the measured phase error, the thicker line is the reconstructed phase error.

moving average, corresponding to a bandwidth of 200 Hz. This process removes some of the variability from the data and allows the underlying trend to be more easily seen. The shape of the phase error curve has been well captured for each microphone up to a frequency of approximately 5000 Hz.

The most significant source of error in this technique is the deviation of the cross spectral pressure matrix from perfect Töplitz structure. The departure from Töplitz structure in phase is of the same magnitude as the phase errors we wish to determine using the technique, as shown in figure 6.3. Calibration of the microphones to greater accuracy is therefore not possible.

6.5 Conclusions

In this chapter a technique has been proposed to allow the phase calibration of in-duct axial arrays. The advantage of this technique over simple free-field calibration is that it allows the array to be rapidly calibrated *in-situ*.

The technique is an extension of the SONAR linear array calibration technique proposed by Paulraj *et al.* [68] and Sng *et al.* [67]. This chapter contains the first experimental comparison of both methods. The Sng method has been shown to perform better than the Paulraj method on the experimental data tested.

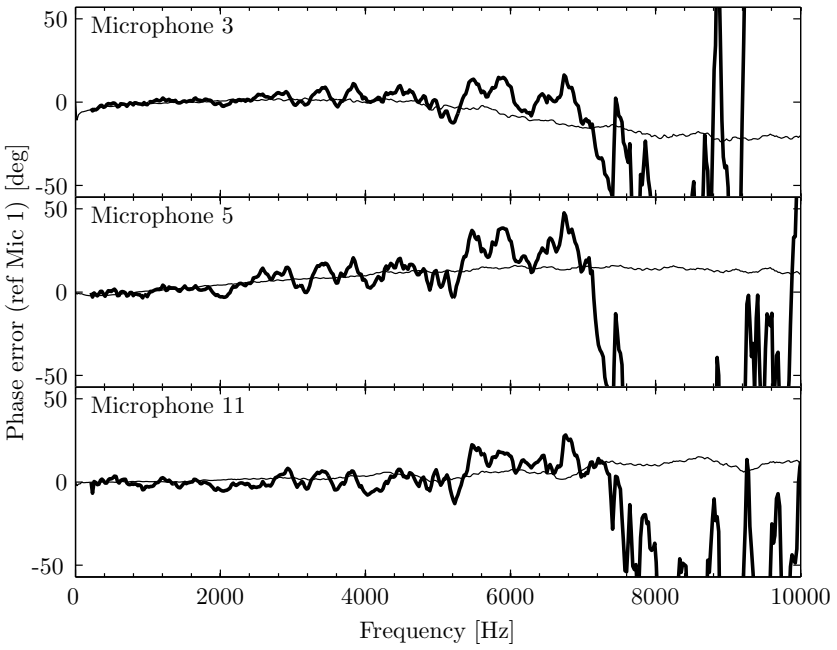

FIGURE 6.10: A plot of the reconstructed phase errors as a function of frequency Sng method for microphone 3 (top), 5 (middle) and 11 (bottom). The reconstructed phase errors are processed using a 10 point (200 Hz) moving average.

Chapter 7

Conclusions and Further Work

7.1 Conclusions

This chapter is a summary of the conclusions from the previous chapters. Section 7.2 suggests some possibilities for further work.

In chapter 1 a survey of the literature indicated an absence of satisfactory experimental techniques which allow the rotor and stator based broadband sources in an aeroengine to be individually differentiated. Chapter 1 also identified a need for measurement technique to allow far-field directivity to be estimated from in-duct measurements.

In chapter 2 the first new measurement technique of the thesis was presented. An inversion technique suitable for the determination of rotating, broadband sources in a duct was developed. The novel aspect of this technique is that it allows the determination of source strengths in the rotating reference frame.

It was shown that the rotation of sources in a duct causes a coupling between source and propagation terms. Existing inversion techniques therefore cannot be used for the determination of aerodynamic sources on rotor blades. The inversion technique was based on the derivation of a new Green's function, which includes the effects of source rotation.

One disadvantage of the technique is that the resolution limits have been shown to be significantly larger than the effective separation distance of uncorrelated sources located on the fan blade trailing edge. This causes the matrix to be inverted to be ill-conditioned. In order to improve the resolution limits, measurements must be made in the near field of the rotor, and this requires a large number of sensors.

In chapter 3 a method was proposed that allowed source quantification without matrix inversion. The method was based on a focused beamformer technique whose principle

application was to quantify how much of the radiated broadband noise from the fan can be attributed to the rotor alone and how much is due to the stator.

The rotating focus beamformer was shown to be able to differentiate between rotor and stator sources by virtue of two properties. Firstly due to its finite mainlobe and sidelobe rejection, and secondly due to additional suppression of stationary sources when detected by a rotating beam and vice-versa. This "smearing" effect was exploited to allow simulated rotor and stator based sources to be quantified. The factors that influence the resolution of the beamformer were also investigated in detail.

Chapter 4 presented a different approach to characterise broadband aeroengine noise. Rather than attempt to quantify the sources on the fan, the technique proposed in chapter 4 used an array of in-duct microphones to deduce the radiated directivity from the duct. The technique is restricted to broadband, multi-mode sound fields whose directivity patterns are axi-symmetric, and whose modes are mutually uncorrelated.

The technique provides a relationship between the output of an in-duct axial beamformer and the far-field polar directivity pattern. This relationship is described by a transfer function. The transfer function appropriate for radiation from a no-flow, hard-walled cylindrical duct was derived in detail. Transfer functions appropriate to aeroengine inlet and exhaust ducts were also presented. One of the main advantages of this technique is the relatively small number of microphones required. An array of around 10 microphones spaced half a wavelength apart was shown to be sufficient in predicting the far-field directivity pattern.

The in-duct to far-field technique proposed in chapter 4 was experimentally validated in chapter 5. The main aim of the experiment was to verify the no-flow results of chapter 4, in particular the estimation of far-field directivity using an in-duct axial microphone array.

The experiment showed that the in-duct to far-field technique can accurately predict both the shape and magnitude of the radiated far-field directivity pattern when the in-duct sound field has incoherent modes. The most accurate predictions were achieved for frequencies close to the optimum frequency of the array, where the inter-microphone spacing was equivalent to half a wavelength. The technique was able to predict detailed features in the radiated directivity pattern, especially when the longest array, consisting of 15 microphones, was used.

All three techniques proposed in the thesis rely on measurements of pressure to be made using in-duct microphone arrays. The calibration of such arrays is complicated by the fact that not only must their individual sensitivities be known, but also their phase characteristics. Calibrating the microphones individually, outside of the duct, and then mounting them can alter their phase responses. In chapter 6 an *in-situ* phase calibration technique was proposed to allow rapid calibration of in-duct microphone arrays.

The technique proposed in chapter 6 is an extension of a linear array calibration technique for SONAR hydrophone arrays first proposed by Paulraj *et al.* [68] and later modified by Sng *et al.* [67]. Chapter 6 contained the first experimental comparison of both methods. The experimental validation showed that phase errors of most of the microphones used in the experiment could be determined to within a few degrees using the Sng method.

In conclusion, this thesis has presented three novel experimental techniques which all have the potential to give new insights into broadband aeroengine noise and its generation mechanisms.

7.2 Suggestions for further work

The following is a list of suggestions for further work that has arisen as a result of the work presented in this thesis:

- One of the major disadvantages of the inversion technique proposed in chapter 2 is that the matrix to be inverted becomes ill-conditioned as the complexity of the problem increases. To overcome this it may be possible to apply regularisation techniques such as those proposed in the context of acoustic inversion problems by Kim and Nelson [29].
- In chapter 3 a focused beamformer was developed. One of the limitations of beamforming is the difficulty of accurately determining acoustic source strengths, due to the presence of sidelobes in the beam pattern. Deconvolution methods, as proposed in the context of aeroacoustic beamforming problems by Brooks and Humphreys [70] aim to remove the influence of the beam pattern. These techniques, and similar methods as summarised in a review article by Ehrenfried and Koop [71], would potentially improve the results obtained from the technique proposed in chapter 3.
- The in-duct measurement techniques proposed in chapters 2 and 3 have yet to be experimentally verified. Such an experiment would be complex, due to the large number of microphones required. It may be possible to validate the technique using pre-existing experimental data. It would be particularly interesting to compare the technique in chapter 3 with the rotating beamformer proposed by Sijtsma [40].
- Further work is required to refine the in-duct to far-field prediction technique proposed in chapter 4 for use on industrial fan rigs. In particular the developement of transfer functions that take into account the effect of complex exhaust geometries, which is most likely to be achieved by using numerical radiation codes in place of the analytical ones currently used. A detailed experimental comparison of the far-field predictions obtained using this technique, and those obtained using a full-modal decomposition coupled with a mode-by-mode propagation model is also required.

- The array calibration technique proposed in chapter 6 shows promising early experimental results. More study is required to determine whether the accuracy of the results will improve when the phase errors to be reconstructed are larger than the standard deviation of the Töplitz form of the pressure cross spectral matrix.

Appendix A

Normalised mode shape functions

In this thesis Ψ_{mn} are normalised mode shape functions given by

$$\Psi_{mn}(r,\theta) = \frac{1}{\Lambda_{mn}}\psi_{mn}(r)e^{-im\theta} \tag{A.1}$$

where in the case of a cylindrical, hollow duct,

$$\psi_{mn} = J_m(\sigma_{mn}\frac{r}{a}) \tag{A.2}$$

and for a cylindrical, annular duct,

$$\psi_{mn} = AJ_m(\alpha_{mn}\frac{r}{a}) - BY_m(\alpha_{mn}\frac{r}{a}) \tag{A.3}$$

where α_{mn} is the radial wavenumber that satisfies the boundary condition at both the inner and outer walls of the duct, and

$$A = \cos(\tau), \quad B = \sin(\tau), \quad \tau = \tan^{-1}\left(\frac{J'_m(\alpha_{mn})}{Y'_m(\alpha_{mn})}\right) \tag{A.4}$$

using the notation of Rienstra *et al.* [72], where a prime denotes derivation.

The normalisation constants Λ_{mn} are introduced to satisfy the condition

$$S^{-1}\int_S |\Psi_{mn}|^2 dS = 1 \tag{A.5}$$

Taking the square of equation (A.1) and inserting into (A.5) gives, for the hollow cylindrical duct,

$$\Lambda_{mn}^2 = \frac{2}{a^2}\int_0^a |J_m(\sigma_{mn}\frac{r}{a})|^2 r dr \tag{A.6}$$

The integral in equation (A.6) evaluates (Abramowitz and Stegun [73] eq. 11.4.2) to

$$\Lambda_{mn}^2 = \begin{cases} |J_m(\sigma_{mn})|^2 & \text{for } m = 0, n = 0 \\ (1 - \frac{m^2}{\sigma_{mn}^2})|J_m(\sigma_{mn})|^2 & \text{for } m \neq 0, n \neq 0 \end{cases} \tag{A.7}$$

In the annular duct case, a similar, but more complicated analytical expression for Λ_{mn}^2 is also obtainable, as given for example, by Rienstra *et al.* [72].

Appendix B

Flat plate turbulence model

In the flat-plate turbulence model used in section 2.4 γ is an experimentally determined constant, typically 0.7 and the turbulent eddy convection velocity, U_c, over a flat plate, is approximately related to the free stream velocity U_∞ by

$$U_c = 0.7U_\infty \tag{B.1}$$

The single-point frequency spectrum of wall pressure fluctuations $\Phi_{ff}(r_s, \omega)$ in equation (2.51) is [51] is

$$\Phi_{ff}(\omega, r_s) \propto \begin{cases} \rho_0^2 U_\tau^4 (\delta/U_c)(\omega\delta/U_c)^2 & \text{for } \frac{\omega\delta}{U_c} \leq 1 \\ \rho_0^2 U_\tau^4 \omega^{-1} & \text{for } 1 < \frac{\omega\delta}{U_c} \leq \frac{\frac{1}{30}U_\tau\delta}{\nu} \\ \rho_0^2 (U_\tau^4)^{-1} (\omega\delta/U_c)^{-4} & \text{for } \frac{\omega\delta}{U_c} > \frac{\frac{1}{30}U_\tau\delta}{\nu} \end{cases} \tag{B.2}$$

where U_τ, δ and U_c all vary with radial position r_s along the blade. The turbulent boundary layer thickness is approximately [51]

$$\delta = \frac{c}{Re_c^{0.2}} \tag{B.3}$$

where c is the rotor chord length, ν is the kinematic viscosity and Re_c the Reynolds number cU_∞/ν defined with respect to c.

In equation (B.2) the hydrodynamic friction velocity U_τ, is an experimentally defined ratio which for a smooth flat plate [51] is $U_\tau/U_\infty = 0.037$.

Appendix C

Interpretation of p_Ω

In this appendix it is shown that the pressure p_Ω is the pressure that would be measured by a microphone rotating around the duct axis at the same angular frequency Ω as the source distribution.

If the microphones are made to rotate around the the duct axis at an angular frequency Ω, so that $\theta = \tilde{\theta} - \Omega t$, where $\tilde{\theta}$ is the angular position of the sensor in the rotating reference frame, equation (2.15) for the time varying acoustic pressure measured by the rotating microphones becomes

$$p(\tilde{\mathbf{x}},t) = \int_{\tilde{S}} \sum_{m=-m^-}^{m^+} f(\tilde{\mathbf{y}},\omega - m\Omega) \int_{-\infty}^{\infty} \sum_{n=0}^{n_0} \Big[\gamma_{mn}^{\pm}\cos\beta + \frac{m}{r_s}\sin\beta\Big] \frac{\psi_{mn}(r)\psi_{mn}^*(r_s)e^{im(\tilde{\theta}-\tilde{\theta}_s)}}{\Lambda_{mn}} \times \\ \times \int_{-\infty}^{\infty} \frac{e^{i(\omega-m\Omega)t}e^{-i\gamma_{mn}^{\pm}(z-z_s)}}{\kappa_{mn}(\omega)} d\omega d\tilde{S}(\tilde{\mathbf{y}}) \tag{C.1}$$

where $\tilde{\mathbf{x}}$ is the measurement position in the rotating reference frame $\tilde{\mathbf{x}} = [r, \tilde{\theta}, z]$.

Fourier transforming equation (C.1) with respect to t,

$$p(\tilde{\mathbf{x}},\omega') = \frac{1}{2\pi}\int_{-\infty}^{\infty} p(\tilde{\mathbf{x}},t)e^{-i\omega' t}dt \tag{C.2}$$

gives the frequency spectrum as observed by the rotating microphone as

$$p(\tilde{\mathbf{x}},\omega') = \int_{\tilde{S}}\int_{-\infty}^{\infty} \sum_{m=-m^-}^{m^+} f(\tilde{\mathbf{y}},\omega - m\Omega) g_m(\tilde{\mathbf{y}},r,x,\omega)\delta(\omega-\omega'-m\Omega)e^{im\tilde{\theta}}d\omega d\tilde{S}(\tilde{\mathbf{y}}) \tag{C.3}$$

i.e.,

$$p(\tilde{\mathbf{x}},\omega') = \int_{\tilde{S}} \sum_{m=-m^-}^{m^+} f(\tilde{\mathbf{y}},\omega') g_m(\tilde{\mathbf{y}},r,x,\omega'+m\Omega)e^{im\tilde{\theta}}d\tilde{S}(\tilde{\mathbf{y}}) \tag{C.4}$$

Comparison of equation (C.4) with equation (2.33) shows that

$$p(\tilde{\mathbf{x}}, \omega) = p_\Omega(\mathbf{x}, \omega) \tag{C.5}$$

The two equations are therefore identical with $\mathbf{x} = \tilde{\mathbf{x}}$. This suggests that the acoustic pressure, p_Ω defined by equation (2.34) is precisely equivalent to that measured by the sensors rotating at the shaft rotational velocity Ω in which the sources appear stationary.

Appendix D

The equivalence of an equal energy per mode sound field and isotropic noise.

Here we show that an equal energy per mode sound field in a duct in the high-ka limit is equivalent to a semi-isotropic noise field. Assuming incoherent modes the total squared pressure at the duct wall, $|p_w(\omega)|^2$, can be written as the sum of the squared modal pressure due to each mode,

$$|p_w(\omega)|^2 = \sum_{mn} |p_w(\phi_{mn}, \omega)|^2 \tag{D.1}$$

In the high-ka limit the summation in equation (D.1) can be written as an integral over ϕ,

$$|p_w(\omega)|^2 = \int_0^{\pi/2} |p_w(\phi, \omega)|^2 \, d\phi \tag{D.2}$$

where $|p_w(\phi, \omega)|^2$ is integrated over the *continuous* mean square pressure per unit angle ϕ. By taking the integral from 0 to $\pi/2$ we are assuming sound propagation in one direction only.

From equation (4.18) the squared model amplitude in an equal energy per mode sound field varies as, $|A(\phi_{mn})|^2 \propto 1/\cos(\phi_{mn})$. Therefore $|p_w(\phi, \omega)|^2$ can be written as

$$|p_w(\phi, \omega)|^2 \propto \frac{n(\phi)}{\cos\phi < \Lambda >} \tag{D.3}$$

where $< \Lambda >$ is the normalisation constant (defined for a hard-walled cylindrical duct in equation (A.7)) averaged over m and n, introduced to correct for the fact that measurements are made at the duct wall. Joseph *et al.* show that $< \Lambda > \rightarrow 2$ as $ka \rightarrow \infty$.

Noting from Rice[60] that $n(\phi)$ may be written as

$$n(\phi) = 2\sin\phi\cos\phi \tag{D.4}$$

Combining equations (D.3) and (D.4) the mean square pressure in an elementary bandwidth $d\phi$ is

$$|p_w(\phi,\omega)|^2 d\phi \propto \sin\phi d\phi \tag{D.5}$$

In equation (D.5) $\sin\phi d\phi$ is also proportional to the elementary solid angle since $d\Omega = 2\pi\sin\phi\, d\phi$. Thus the mean square pressure per unit solid angle $d\Omega$ is constant.

Bibliography

[1] P.F. Joseph and M.G. Smith. *Advanced Applications in Acoustics, Noise and Vibration*, chapter Aircraft Noise, pages 292–346. Spon Press, 2004. Edited by Frank Fahy and John Walker.

[2] International Civil Aviation Organization. Annex 16 - environmental protection. volume 1 - aircraft noise., July 2005. 4th Edition.

[3] N. Tandon. Aircraft noise. *Noise & Vibration Worldwide*, 34:11–14(4), 1 April 2003.

[4] G.P. Howell, A.J. Bradley, M.A. McCormick, and J.D. Brown. De-dopplerization and acoustic imaging of aircraft flyover noise measurements. *Journal of Sound and Vibration*, 105(1):151 – 67, 1986.

[5] L. Brusniak, J.R. Underbrink, and R.W. Stoker. Acoustic imaging of aircraft noise sources using large aperture phased arrays. In *12th AIAA/CEAS Aeroacoustics Conference*, Cambridge, Massachusetts, 2006. AIAA-2006-2715.

[6] S. Guérin and U. Michel. Aero-engine noise investigated from flight tests. In *12th AIAA/CEAS Aeroacoustics Conference*, Cambridge, Massachusetts, 2006. AIAA-2006-2463.

[7] Society of Automotive Engineers. Measurement of far field noise from gas turbine engines during static operation. ARP1846, February 1990.

[8] Donald S. Weir and Jeff M. Mendoza. Static and flight aeroacoustic evaluations of a variable exhaust nozzle. In *11th AIAA/CEAS Aeroacoustics Conference*, volume 5, pages 3087 – 3097, Monterey, CA, United States, 2005.

[9] Donald S. Weir, Bruce Bouldin, and Jeff M. Mendoza. Static and flight aeroacoustic evaluations of a scarf inlet. In *12th AIAA/CEAS Aeroacoustics Conference*, volume 2, pages 808 – 826, Cambridge, MA, United States, 2006.

[10] P.G.J. Schwaller, N.J. Baker, J.D. Tomlinson, P. Sijtsma, and R. Hemmings. Noise validation of model fan rig with engine. In *12th AIAA/CEAS Aeroacoustics Conference*, volume 2, pages 1014 – 1025, Cambridge, MA, United States, 2006.

[11] Peter Bartlett, Nick Humphreys, Pam Phillipson, Justin Lan, Eric Nesbitt, and John Premo. The joint rolls-royce/boeing quiet technology demonstrator programme. In *10th AIAA/CEAS Aeroacoustics Conference*, volume 1, pages 806 – 816, Manchester, United Kingdom, 2004.

[12] M.J. Fisher, M. Harper-Bourne, and S.A.L. Glegg. Jet engine noise source location: The polar correlation technique. *Journal of Sound and Vibration*, 51(1):23 – 54, 1977.

[13] S.A.L. Glegg. *Jet Noise Source Location*. PhD thesis, Institute of Sound and Vibration Research, University of Southampton, 1979.

[14] J.P. Battaner-Moro. A large polar array for full-scale aero-engine noise source location and breakdown. In *12th AIAA/CEAS Aeroacoustics Conference*, Cambridge, Massachusetts, 2006. AIAA-2006-2652.

[15] Sang Soo Lee. Phased-array measurement of modern regional aircraft turbofan engine noise. In *12th AIAA/CEAS Aeroacoustics Conference*, volume 5, pages 3315 – 3336, Cambridge, MA, United States, 2006.

[16] U. Michel. Characterization of jet noise with phased microphone arrays. In *A review of the AARC Engine Noise Phased Array Workshop (editor: Stewart Glegg)*, Cambridge, MA, May 11-12 2006.

[17] F.O. Castres and P.F. Joseph. Mode detection in turbofan inlets from near field sensor arrays. *Journal of the Acoustical Society of America*, 121(2):796 – 807, 2007.

[18] J. Lan, J. Premo, and D. L. Sutliff. Inlet mode measurements with an inlow control device microphone array. In *8th AIAA/CEAS Aeroacoustics Conference*, Breckenridge, CO, 2002.

[19] F. Farassat, D. Nark, and H. Russel. The detection of radiated modes from ducted fan engine. In *7th AIAA/CEAS Aeroacoustics Conference*, Maastricht, The Netherlands, 2001.

[20] R. Thomas, F. Farassat, L. Clark, C. Gerhold, J. Kelly, and L. Becker. A mode detection using the azimuthal directivity of a turbofan model. In *5th AIAA/CEAS Aeroacoustics Conference*, Bellevue, WA, 1999.

[21] Ulrich W. Ganz, Paul D. Joppa, Timothy J. Patten, and Daniel F Scharpf. Boeing 18-inch fan rig broadband noise test. Technical Report CR-1998-208704, NASA, 1998.

[22] U. Bolleter and M.J. Crocker. Theory and measurement of modal spectra in hard-walled cylindrical ducts. *Journal of the Acoustical Society of America*, 51(5):1439 – 47, 1972.

[23] J.M. Tyler and T.G. Sofrin. Axial flow compressor noise studies. *Transactions of the society of automotive engineers*, 70:309–32, 1962.

[24] L. Enghardt, C. Lowis, and L. Neuhaus. Broadband sound power determination in flow ducts. In *AIAA/CEAS*, Manchester, UK, 2004.

[25] L. Enghardt, A. Holewa, and U. Tapken. Comparison of different analysis techniques to decompose a broad-band ducted sound field in its mode constituents. In *13th AIAA/CEAS Aeroacoustics Conference*, Rome, 21 - 23 May 2007. AIAA-2007-3520.

[26] International Standards Organisation 5136:2003. Acoustics: Determination of sound power radiated and other air-moving devices. in-duct method, 2003.

[27] J. Billingsley and R. Kinns. The acoustic telescope. *Journal of Sound and Vibration*, 48(4):485 – 510, 1976.

[28] M. J. Fisher and K. R. Holland. Measuring the relative strengths of a set of partially coherent acoustic sources. *Journal of Sound and Vibration*, 201(1):103–125, 1997.

[29] Y. Kim and P.A. Nelson. Spatial resolution limits for the reconstruction of acoustic source strength by inverse methods. *Journal of Sound and Vibration*, 265(3):583–608, 2003.

[30] Y. Kim and P. A. Nelson. Estimation of acoustic source strength within a cylindrical duct by inverse methods. *Journal of Sound and Vibration*, 275(1-2):391–413, 2004.

[31] E.G. Williams. *Fourier Acoustics. Sound radiation and nearfield acoustic holography.* Academic Press, 1999.

[32] K.R. Holland and P.A. Nelson. Sound source characterisation: The focussed beamformer vs. the inverse method. In *Proceedings of the Tenth International Congress on Sound and Vibration, Jul 7-10 2003*, pages 3499–3506, Stockholm, Sweden, 2003. Institute of Acoustics.

[33] C.R. Lowis and P. Joseph. Determining the strength of rotating broadband sources in ducts by inverse methods. *Journal of Sound and Vibration*, 295(3-5):614–632, 2006.

[34] J.M. Mendoza, T.F. Brooks, and W.M. Humphreys Jr. An aeroacoustic study of a leading edge slat configuration. *International Journal of Aeroacoustics*, 1(3):241–274, 2002.

[35] F.V Hutcheson and T.F. Brooks. Measurement of trailing edge noise using directional array and coherent output power methods. *International Journal of Aeroacoustics*, 1(4):329–353, 2002.

[36] S. Oerlemans and P. Sijtsma. Acoustic array measurements of a 1:10.6 scaled airbus A340 model. In *10th AIAA/CEAS Aeroacoustics Conference*, Manchester, United Kingdom, 2004.

[37] Robert P. Dougherty. *Aeroacoustic Measurements*, chapter Beamforming in Acoustic Testing. Springer, 2002. Editor: Mueller, Thomas J.

[38] P. Sijtsma, S. Oerlemans, and H. Holthusen. Location of rotating sources by phased array measurements. In *7th AIAA/CEAS Aeroacoustics Conference*, Maastricht, Netherlands, 2001.

[39] S. Oerlemans, P. Sijtsma, and B.M. Lopez. Location and quantification of noise sources on a wind turbine. *Journal of Sound and Vibration*, 299(4-5):869 – 83, 2007.

[40] P. Sijtsma. Using phased array beamforming to locate broadband noise sources inside a turbofan engine. Technical report, National Aerospace Laboratory (Netherlands), 2006. Based on a presentation held at the AARC Engine Noise Phased Array Workshop, Cambridge, MA, USA. 11-12 May 2006.

[41] C.R. Lowis and P. Joseph. A focused beamformer technique for separating rotor and stator-based broadband sources. In *12th AIAA/CEAS Aeroacoustics Conference (27th AIAA Aeroacoustics Conference)*, Cambridge, Massachusetts, 8-10 May 2006 2006. AIAA-2006-2520.

[42] Philip M. Morse and K. Uno Ingard. *Theoretical Acoustics.* Princeton University Press, first edition, 1986.

[43] Kinsler, Frey, Coppens, and Sanders. *Fundamentals of acoustics.* Wiley, New York, 3rd ed edition, 1982.

[44] William S. Burdic. *Underwater Acoustic Signal Analysis.* Prentice-Hall, 1984.

[45] Don. H. Johnson and Dan. E. Dudgeon. *Array Signal Processing: Concepts and Techniques.* Prentice Hall, 1993.

[46] R. O. Nielsen. *Sonar Signal Processing.* Artech House, 1991.

[47] Walter Eversman. *Aeroacoustics of Flight Vehicles: Theory and Practice*, volume 2: Noise Control, chapter Theoretical Models for Duct Acoustic Propagation and Radiation. NASA, 1991. Editor: Hubbard, H.

[48] M. Goldstein. *Aeroacoustics.* McGraw-Hill, New York, 1976.

[49] C.L. Morfey. Sound transmission and generation in ducts with flow. *Journal of Sound and Vibration*, 14(1):37–55, 1971.

[50] Golub and van Loan. *Matrix computations.* North Oxford Academic, Oxford, 1983.

[51] W.K. Blake. *Mechanics of Flow Induced Sound and Vibration*, volume II. Academic Press, INC., 1986.

[52] S.A.L. Glegg. Airfoil self-noise generated in a cascade. *AIAA Journal*, 36(9):1575 – 82, 1998.

[53] P.A. Nelson. *Advanced Applications in Acoustics, Noise and Vibration*, chapter Source Identification and Location. Spon Press, 2004. Edited by Frank Fahy and John Walker.

[54] A.P. Dowling and J.E. Ffowcs Williams. *Sound and the sources of sound.* Ellis Horwood Limited, 1983.

[55] Barry D. Van Veen and Kevin M. Buckley. Beamforming: A versatile approach to spatial filtering. *IEEE ASSP Magazine (Acoustics, Speech, and Signal Processing)*, 5(2):4–24, 1988.

[56] E.J. Rice and M.F. Heidmann. Modal propagation angles in a cylindrical duct with flow and their relation to sound radiation. In *17th Aerospace Sciences Meeting*, New Orleans, January 15-17 1979.

[57] C.J. Chapman. Sound radiation from a cylindrical duct. part 2. source modelling, nil-shielding directions, and the open-to-ducted transfer function. *Journal of Fluid Mechanics*, 313:367–80, 1996.

[58] P. Joseph, C.L. Morfey, and C.R. Lowis. Multi-mode sound transmission in ducts with flow. *Journal of Sound and Vibration*, 264(3):523–544, 2003.

[59] Phillip Joseph and Christopher L. Morfey. Multimode radiation from an unflanged, semi-infinite circular duct. *Journal of the Acoustical Society of America*, 105(5):2590, 1999.

[60] E.J. Rice. Modal density function and number of propagating modes in ducts. Technical Memorandum TM X-73539, NASA, 1976. Presented at the 92nd Meeting of the Acoustical Society of America, San Diego, California, Nov. 16-19, 1976.

[61] E.J. Rice. Broadband noise radiation models for aircraft engines. In *5th AIAA/CEAS Aeroacoustics Conference and Exhibit,*, volume AIAA-1999-1953, Bellevue, WA, May 10-12 1999.

[62] Free Field Technologies, Louvain-la-Neuve, Belgium. *ACTRAN 2004 users' manual*, 2004.

[63] G. Gabard and R. J. Astley. Theoretical model for sound radiation from annular jet pipes: far- and near-field solutions. *Journal of Fluid Mechanics*, 549:315–341, 2006.

[64] R.M. Munt. Acoustic radiation from a circular cylinder in a subsonic stream. *Journal of the Institute of Mathematics and its Applications*, 16:1–10, 1975.

[65] R. Sugimoto, R.J. Astley, L. De Mercato, K.R. Holland, and V. Jurdic. Prediction methods for propagation in bypass ducts and comparison with measured data. In *11th AIAA/CEAS Aeroacoustics Conference (26th AIAA Aeroacoustics Conference)*, Monterey, California, 23-25 May 2006 2005. AIAA-2005-3059.

[66] Robert J. Urick. *Principles of Underwater Sound*. McGraw-Hill, 3rd edition, 1983.

[67] Y.H. Sng and Youming Li. Fast algorithm for gain and phase error calibration of linear equi-spaced (les) array. In *Proceedings of ICSP2000*, 2000.

[68] A. Paulraj and T. Kailath. Direction of arrival estimation by eigenstructure methods with unknown sensor gain and phase. *ICASSP 85. Proceedings of the IEEE International Conference on Acoustics, Speech, and Signal Processing (Cat. No. 85CH2118-8)*, pages 640 – 3, 1985.

[69] A.G. Piersol. Time delay estimation using phase data. *IEEE Transactions on Acoustics, Speech and Signal Processing*, 29(3):471 – 7, 1981.

[70] T. F. Brooks and W.M. Humphreys. A deconvolution approach for the mapping of acoustic sources (damas) determined from phased microphone arrays. *Journal of Sound and Vibration*, 294(4-5):856–879, July 2006.

[71] K. Ehrenfried and L. Koop. Comparison of iterative deconvolution algorithms for the mapping of acoustic sources. *AIAA Journal*, 45(7):1584–1595, July 2007.

[72] S.W. Rienstra and A. Hirschberg. An introduction to acoustics. Technical Report IWDE 92-06, Eindhoven Institute of Technology, 2006. 19th July 2006 edition obtained from http://www.win.tue.nl/ sjoerdr/.

[73] M. Abramowitz and I.A. Stegun. *Handbook of Mathematical Functions*. Dover Publications, INC., ninth edition, 1970.